# Passive mode-locking of 2-μm solid-state lasers: towards sub-10 optical cycle pulse generation


im Fachbereich Physik
der Freien Universität Berlin
eingereichte Dissertation

**Yicheng Wang**
2017

This work was carried out at the Max Born Institute for Nonlinear Optics and Ultrafast Spectroscopy, Berlin, under the mentorship of Dr. V Petrov.

**Erstgutachter: Prof. Dr. Marcus Vrakking (Betreuer)**

**Zweitgutachter: Prof. Dr. Ivan Buchvarov**

Date of the defense: 6. November 2017

# Abstract

This thesis is devoted to the development of novel passively mode-locked lasers around 2 micron based on the Tm and Ho trivalent ion stimulated emission in this spectral range. The main objective of the experimental work was to investigate the limits of ultrashort pulse generation with this kind of solid-state lasers. To this aim, novel active media and novel saturable absorbers were studied and the performance of the mode-locked lasers was characterized.

A fundamental prerequisite for the generation of femtosecond pulses from a mode-locked laser is the available gain bandwidth. For the given two ions which have no alternative in this spectral range this can be optimized in terms of flat and broad spectral gain cross-sections only by selection of suitable host materials. The materials which were exclusively available for this research included ceramic samples of the isotropic garnets $Y_3Al_5O_{12}$ (YAG) and $Lu_3Al_5O_{12}$ (LuAG), one uniaxial disordered crystal, $CaGdAlO_4$ (CALGO), and one biaxial crystal with pronounced distortion of the crystal field, $MgWO_4$. The samples used were designed on the basis of careful spectroscopic characterization of the relevant properties and in particular the anisotropy which offers more options for selection of the proper orientation.

The saturable absorbers employed in the 2 micron spectral range included novel GaSb-based semiconductor saturable absorber mirrors (SESAMs) with faster relaxation times, as well as low-loss carbon nanostructures (graphene and single-walled carbon nanotubes, SWCNTs) deposited on transparent substrates, which typically exhibit broadband nonlinear response. All of them can be considered as being slow in their recovery compared to the pulse durations achieved.

Stable and self-starting SESAM mode-locking was achieved with three garnet ceramics (Tm:YAG, Ho:YAG, and Tm:LuAG) generating picosecond pulses. Sub-picosecond durations were obtained with the SESAM mode-locked Tm:CALGO laser. Finally, all the saturable absorbers were compared with the $Tm:MgWO_4$ crystal and for a specific orientation, this laser generated for the first time sub-100 fs pulses which were characterized by frequency-resolved optical gating (FROG) measurements.

**Keywords:** Tm- and Ho-doped laser materials, mode-locked solid-state lasers, femtosecond pulses, eye-safe 2-micron ultrafast lasers, saturable absorbers

# Kurzzusammenfassung

Diese Arbeit widmet sich der Entwicklung von neuartigen, passiv modengekoppelten Lasern im 2-µm Wellenlängenbereich auf der Basis von Tm- und Ho-dotierten aktiven Materialien. Das Hauptziel der experimentellen Arbeit war es, die Grenzen der Ultrakurzpulserzeugung mit dieser Art von Festkörperlasern zu erforschen. Zu diesem Zweck wurden neuartige aktive Medien und neuartige sättigbare Absorber untersucht und deren Potential in modengekoppelten Laser charakterisiert.

Eine Grundvoraussetzung für die Erzeugung von Femtosekunden-Impulsen mit einem modengekoppelten Laser ist die verfügbare spektrale Verstärkungsbandbreite. Diese sollte ein breites und flaches Verstärkungsprofil aufweisen, was nur durch die Auswahl geeigneter Wirtsmaterialen optimiert werden kann. Für $Tm^{3+}$- und $Ho^{3+}$-Ionen, welche im 2-µm Spektralbereich alternativlos sind, standen folgende Wirtsmaterialien exklusiv zur Verfügung: keramische Proben der isotropen Granate $Y_3Al_5O_{12}$ (YAG) und $Lu_3Al_5O_{12}$ (LuAG), ein uniaxialer ungeordneter Kristall, $CaGdAlO_4$ (CALGO) und ein biaxialer Kristall mit ausgeprägter Verzerrung des Kristallfeldes, $MgWO_4$. Die verwendeten Laserkristalle wurden auf der Grundlage einer sorgfältigen spektroskopischen Charakterisierung der relevanten Eigenschaften konzipiert. Der Anisotropie wurde besonderes Augenmerk gewidmet, da sie Auswahlmöglichkeiten für geeignete Kristallorientierungen bietet.

Die eingesetzten sättigbaren Absorber für den 2-µm Spektralbereich umfassten neuartige, auf GaSb basierende, sättigbare Absorberspiegel (SESAMs) mit kurzen Relaxationszeiten sowie verlustarme Kohlenstoff-Nanostrukturen (Graphen und einwandige Kohlenstoff-Nanoröhrchen, SWCNTs). Letztere wurden auf transparenten Substraten abgeschieden und weisen typischerweise eine breitbandige nichtlineare Response auf. Die Relaxationszeiten aller eingesetzten sättigbaren Absorber sind lang im Vergleich zu den erreichten Laserimpulsdauern.

Stabile und selbststartende Modenkopplung unter Verwendung von SESAMs wurde mit drei Granatkeramiken erreicht (Tm:YAG, Ho:YAG und Tm:LuAG). Die emittierten Pulsdauern lagen bei wenigen Pikosekunden. Kürzere Pulse, im sub-Pikosekundenbereich, wurden mit dem gleichen Prinzip mit einen Tm:CALGO Laser erzielt. Der Vergleich aller eingesetzter sättigbarer Absorber wurde mit dem, hinsichtlich der spektroskopischen Eigenschaften, vielversprechendsten aktiven Material, $Tm:MgWO_4$, durchgeführt. Unter Verwendung eines Graphen-basierten sättigbaren Absorbers und einer spezifischen Kristallorientierung wurden erstmals Impulse mit sub-100 fs Dauer für Festkörperlaser im 2-µm Spektralbereich erzeugt. Die Charakterisierung dieser Pulse mittels frequenzaufgelöstem optischem Gating (FROG) lieferte eine nahezu Fourier-limitierte Pulsqualität.

# Contents

# Glossary of abbreviations

| | |
|---|---|
| AC | autocorrelation |
| A-FPSA | antiresonant Fabry–Pérot saturable absorber |
| AR | antireflection |
| ASE | amplified spontaneous emission |
| CALGO | $CaGdAlO_4$ |
| CALYO | $CaYAlO_4$ |
| CEP | carrier-envelope phase |
| CM | chirped mirror |
| CNT | carbon nanotube |
| CPA | chirped-pulse amplification |
| CPOPA | chirped-pulse optical parametric amplification |
| CR | cross-relaxation |
| CW | continuous-wave |
| CWML | continuous-wave mode-locking |
| Cz | Czochralski |
| ESA | excited-state absorption |
| ET | energy-transfer |
| FH | fourth harmonic |
| FROG | frequency resolved optical gating |
| FWHM | full width at half maximum |
| FWOT | full wave optical thickness |
| GD | group delay |
| GDD | group delay dispersion |
| GSA | ground-state absorption |
| GVD | group velocity dispersion |
| GVM | group velocity mismatch |
| HHG | high harmonic generation |
| HITRAN | high resolution transmission database developed at the Harvard-Smithsonian Center for Astrophysics |
| IR | infrared |
| KLM | Kerr lens mode-locking |
| KREW | $KRE(WO_4)_2$, RE = Gd, Y, Lu |
| LD | laser diode |
| LIDAR | light detection and ranging |
| Ln | lanthanide |
| LuAG | $Lu_3Al_5O_{12}$ |

| | |
|---|---|
| M | migration |
| MBE | molecular beam epitaxy |
| MgW | $MgWO_4$ |
| OC | output coupler |
| OPA | optical parametric amplification |
| OPSL | optically pumped semiconductor laser |
| PMMA | polymethyl-methacrylate |
| PP | prism pair |
| QD | quantum defect |
| QSML | Q-switched mode-locking |
| QW | quantum well |
| RE | rare earth |
| RF | radio frequency |
| RoC | radius of curvature |
| SA | saturable absorber |
| SCF | single crystal fiber |
| SESAM | semiconductor saturable absorber mirror |
| SF | self-focusing |
| SH | second harmonic |
| SHG | second harmonic generation |
| SPM | self-phase modulation |
| SPOPO | synchronously pumped optical parametric oscillator |
| SSL | solid-state laser |
| SWCNT | single-walled carbon nanotube |
| TBP | time-bandwidth product |
| TM | transition metal |
| TOD | third order dispersion |
| TPA | two-photon absorption |
| TSSG | top-seeded solution growth |
| UC | up-conversion |
| UCF | up-conversion fluorescence |
| YAG | $Y_3Al_5O_{12}$ |
| YSGG | $Y_3Sc_2Ga_3O_{12}$ |

# Chapter 1
# Introduction

Mode-locked ultrafast solid-state lasers generating picosecond and femtosecond light pulses in the near-IR up to ~ 3 μm have become nowadays an indispensable research tool in physics, chemistry, biology, medicine as well as in machining and engineering [1].

Developments of such coherent sources around 2 μm, i.e. lasers based on Tm- and/or Ho-doped materials, is drawing increasing attention in the last decade due to their unique advantages for certain applications. Because of the strong water absorption in this spectral range, such sources fall into the category of the "eye-safe" lasers. The "eye-safe" range starts in fact from around 1.4 μm but Er-lasers lasers operating near 1.6 μm are much more limited in terms of achievable efficient pumping, output power or pulse energies. In general, 2 μm lasers are considered advantageous for free-space applications such as eye-safe LIDAR (LIght Detection And Ranging) and gas sensing or for direct atmospheric optical communications [2, 3]. The favorable absorption in water makes them very useful for medical treatments and highly localized surgery in particular (i.e. precise cutting of biological tissue combined with a coagulation) [3]. Transparent plastic processing (e.g. welding of polymers) benefits from the fact that such materials directly absorb ~ 2 μm laser light in contrast to the standard ~ 1 μm laser sources which require artificial absorbers. All these important technological, security, military, environmental and medical applications greatly stimulated the development of 2 μm solid-state lasers defining a new segment in the laser market. However, apart from few exceptions (e.g., very specific material processing or medical issues), the coherent sources required for them emit continuous-wave (CW) radiation or pulses of nanosecond (i.e. short but not ultrashort) durations.

Tm and Ho solid-state lasers can be divided into fiber and bulk (glass, ceramic or crystalline) lasers, both types having their advantages and limitations. Lasers in general and solid-state lasers in particular are often applied also to pump other lasers, basically to create new coherent sources at different (mostly longer) wavelengths where such do not exist. This is generally true also for ~ 2 μm lasers but it makes no sense to employ ultrafast lasers for pumping other solid-state lasers because the relevant relaxation processes in such solids proceed on a much slower time scale. Thus, the so-called synchronous pumping (i.e. an ultrafast laser pumps another ultrafast laser with matched cavity length), widely employed in the past for dye lasers [4], is not relevant to all-solid-state laser systems. It is possible, however, to synchronously pump a nonlinear material (non-centrosymmetric crystal exhibiting $2^{nd}$ order optical nonlinearity) in a cavity whose round-trip time corresponds exactly to the repetition rate of the solid-state laser because this process is not related to electronic transitions and is instantaneous in its nature. Such devices called synchronously pumped optical parametric oscillators (SPOPOs) represent nowadays the main direct "application" of ultrafast 2 μm lasers in laser physics because through their wide spectral

tunability they enable the coverage of an extremely broad part of the mid-IR part of the spectrum (e.g., from 3 to 15 μm) [5]. The essential advantage of the pump wavelength region around 2 μm in this case is that one can avoid another higher order but detrimental nonlinear effect known as two-photon absorption. While this effect is present in any nonlinear crystal, the non-oxide crystals employed in the mid-IR are narrow band-gap semiconductors and as such cannot be pumped by the more mature ultrafast solid-state lasers emitting at ~ 800 nm or ~ 1 μm in the near-IR.

SPOPOs operating in the mid-IR possess their own great application potential related to the so-called molecular fingerprint region (the spectral region in which the characteristic vibrations of many molecules occur). Depending on the spectral resolution required in such spectroscopic measurements, picosecond pulses might be more adequate than femtosecond pulses because the temporal and spectral extents of an ultrashort pulse are linked by a relation similar to the Heisenberg uncertainty principle. It is important to note that because the nonlinear process is instantaneous, SPOPOs reproduce the pulse duration of the pump laser and thus picosecond or femtosecond 2 μm lasers might be required as such pump sources. A relatively new field based on femtosecond SPOPOs is related to frequency comb generation in the mid-IR. In the case of femtosecond pulse durations, such frequency combs can be viewed as a collection of ~ $10^5$ phase-locked narrow-bandwidth CW sources, which can be applied to massively parallel high resolution spectroscopy [6]. Direct generation of mid-IR frequency combs is challenging due to the lack of suitable femtosecond laser sources but SPOPOs are a very promising alternative and the best results have been demonstrated by pumping them with femtosecond 2 μm lasers [5]. Frequency combs in the mid-IR can be also generated from a femtosecond 2 μm laser without the SPOPO (i.e. without the complexity required to match two cavities): Propagation in highly nonlinear fibers can be used to produce a Stokes shifted replica of the pump by supercontinuum or Raman generation which is then parametrically amplified by the major part of the available pulse energy near 2 μm. Also in this case the advantage of the pump wavelength is that more efficient nonlinear crystals can be applied in such so-called difference-frequency generation [5].

Mode-locked ultrafast oscillators emit an infinite train of ultrashort pulses typically at a repetition rate of the order of 100 MHz: Thus, the output pulses are much shorter than the corresponding period of ~ 10 ns. The repetition rate of some more sophisticated mode-locked lasers may be as low as few MHz in order to achieve higher single pulse energy or as high as few GHz, e.g. for frequency combs with increased spacing (equal to the longitudinal mode spacing) that can be resolved by compact dispersive elements [1]. In any case the ideal regime of operation under CW pumping is stationary or steady-state which ensures stability and reproducibility of the pulse parameters. Such lasers are limited in their average power to about few Watts (although the shortest pulses are demonstrated normally at average powers of the order of 100 mW or even less) which is mainly related to the thermal load as a result of the heat released in the laser material. This automatically sets a limit on the single pulse energy which is normally on the nJ level or even less. There is one exception and this is the thin-disk laser concept which enables efficient heat removal and has resulted in average powers

reaching the kW level and pulse energies of tens of microjoules directly from a diode-pumped mode-locked laser, albeit at the expense of the pulse duration [7]. It shall be emphasized here that such mode-locked lasers exist only in the 1 μm spectral range: Extension to the 2 μm range is expected in the near future, however, there are a number of new challenges for the thin-disk concept in this spectral range related to the lack of laser diodes for direct pumping, adequate mode-locking elements, and suitable laser gain media.

The well-known approach to increase the pulse energy of an ultrashort pulse emitted from a mode-locked laser in order to enable new applications is its amplification at lower repetition rates (by picking pulses out of the ~ 100 MHz pulse train from the oscillator) [8]. This is possible because the maximum average power reflects fundamental limitations while the pulse energy can reach even the joule level at low repetition rates down to single pulses. Ultrafast laser amplifiers are normally based on the same or similar active medium as the seed oscillator, however, they operate at lower repetition rates (typically from about 10 Hz up to hundreds of kHz). The repetition rate is practically determined by the pump source of the amplifier which again has to be pulsed, typically with nanosecond duration (ultrashort pulses will produce higher order nonlinear effects such as self-focusing leading to optical damage), because only by depositing a high energy into the laser amplifier medium within the fluorescence lifetime (energy storage time) can one achieve high inversion and sufficient gain. An exception here are fiber based ultrafast amplifiers which can be pumped by CW laser diodes and amplify the output of a mode-locked laser (fiber or bulk type) maintaining the original ~ 100 MHz repetition rate, however, the single pulse energy achieved in this case will be obviously limited. In general, the so-called chirped-pulse amplification (CPA) concept is employed to avoid higher order nonlinear effects due to the amplified pulse leading to optical damage in the laser gain medium: The input pulse is stretched in time by dispersive elements and recompressed after laser amplification by similar elements with opposite sign of their group velocity dispersion. All the above applies fully to Tm- and Ho-based ultrafast amplifiers, however, a seed oscillator (i.e. a mode-locked solid-state laser) is always needed. Depending on the application envisaged for the ultrafast amplifier it can also operate in the picosecond or femtosecond regime and the pulse duration is largely, though not fully determined by the seed source. While amplified femtosecond pulses find direct applications, amplified picosecond pulses around 2 μm are needed for pumping of optical parametric amplifiers as discussed in the following.

The present work is devoted to the development and characterization of mode-locked Tm and Ho lasers needed for integration in high average power and high energy laser systems under development for applications in high field physics. This is closely related to the focus of the research programme of the Attosecond Physics Division of the Max Born Institute. The final goal in this case is to achieve high energy few cycle (the optical cycle is equal to ~ 7 fs at 2 μm) pulses at relatively high repetition rates which is only possible by optical parametric amplification (OPA), the same fundamental three-wave nonlinear optical process employed in SPOPOs, however without a cavity thanks to the high pump intensity achievable at lower repetition rates. OPA provides gain bandwidths much broader than any laser amplifier in

which the gain bandwidth is determined by the fluorescence spectrum, however, high amplification factors are achievable only in some special cases (for specific combinations of pump, signal and idler wavelengths) when relatively long nonlinear crystals can be applied [5]. Since pump and seed (at the signal wavelength) laser sources are available only at specific wavelengths, the universal approach for efficient parametric amplification is related again to stretching (i.e. chirping) of the input seed pulses and their instantaneous (in contrast to laser amplifiers which can store the pump energy) amplification in the field of the longer pump pulse followed by recompression to the initial pulse duration. This technique is called chirped-pulse optical parametric amplification (CPOPA) and nowadays plays an important role for high harmonic generation (HHG) of attosecond pulses [9]. Although state-of-the-art HHG sources are mainly based on Ti:sapphire laser amplifiers operating near 800 nm as driving sources, there are many efforts taking place towards longer wavelength driving lasers since the cut-off energy of high harmonics is proportional to $\lambda^2$ [9]. Therefore, the development of ~ 2 μm femtosecond and ultimately few-cycle seed mode-locked lasers is of great importance as they could be further parametrically amplified for HHG. The CPOPA is normally pumped by nanosecond pulses and efficient amplification requires stretching of the seed to a comparable duration. However, when it comes to few-cycle pulses, maintaining such pulse durations is only possible at lower stretching factors, which requires pump sources with duration of the order of few picoseconds. This makes picosecond 2 μm lasers interesting as pump sources for mid-IR CPOPA (e.g., up to 8 μm for the idler) because they can ensure access to yet higher high harmonic photon energies. Such picosecond Tm or Ho lasers can be amplified in CPA laser systems as discussed above [10].

It should be outlined here that femtosecond lasers are nowadays no longer the only source of a seed for high-power CPOPA systems and this holds also for the 2-μm spectral range. As already mentioned such CPOPA chains are pumped by amplified picosecond laser systems (most often based on the CPA architecture). The mature quality of oxide second-order nonlinear crystals which cover the entire near-IR makes it possible to derive a seed wavelength near 2-μm from CPA pump systems operating near 800 nm (Ti:sapphire lasers) or near 1 μm (Yb-lasers). To this aim, apart from difference-frequency generation such schemes employ also supercontinuum generation in bulk materials. The advantage of such methods based on nonlinear optics is the intrinsic synchronization and the passive carrier-envelope phase (CEP) stabilization essential for HHG with few cycle pulses [11].

The seed lasers used in the CPA pump systems normally provide much shorter pulses, serving as a “front end” because CPA is associated with some spectral narrowing and temporal broadening in the process of laser amplification. Therefore, it is in fact advantageous to employ the seed laser for the generation of femtosecond pulses near 2 μm. In this case, however, the energy obtained is very low and it may be problematic to suppress a competing nonlinear process in the CPOPA chain called amplified parametric super-fluorescence [12]. When it comes to Ti:sapphire laser front-ends combined with Nd- or Yb-laser amplifiers in the pump arm, separate amplification in different laser amplifiers for the seed generation will be required which greatly increased the complexity of the entire system [13].

A seed pulse for CPOPA near 2 μm can be directly derived also from the CPA pump system: The supercontinuum generation necessary to shift the wavelength and achieve finally few-cycle pulse durations is, however, much more difficult with picosecond systems and this works with Yb-laser (but not with Nd-laser) based systems operating in the 1 μm spectral range [14]. Availability of femtosecond mode-locked lasers near 2-μm as direct seed sources for CPOPA systems could offer major advantages due to the higher seed level. However, the perfect solution for subsequent HHG will require durations down to the few optical cycles and CEP stabilization. Second-harmonic generation from such femtosecond lasers could provide simultaneously convenient seed for 1-μm based CPA amplifiers based on Nd- or Yb-lasers to be employed as a pump for the CPOPA. The major advantage of a CPOPA system at 2 μm, pumped near 1 μm, is that operation near degeneracy results in substantially broader parametric gain and allows one to use longer nonlinear crystals [5].

The present work is devoted to passively mode-locked bulk solid-state lasers operating in the 2 μm spectral range. This research field advances in steady competition with fiber based systems which have certain advantages but exhibit also some limitations. In fiber lasers, because of the very long active material length and small mode area, there will be strong nonlinear effects leading to structured spectra, the phase noise is much more pronounced and there may be uncontrolled birefringence leading to unpredictable polarization.

The ideal laser material for generating ultrashort pulses will exhibit high absorption and emission cross-sections as well as broad and flat gain spectral shape. However, due to fundamental relationships between these spectroscopic characteristics (the mechanisms for line broadening), a trade-off is inevitable. Other aspects of the laser material such as thermo-mechanical properties or anisotropy are also crucial for the mode-locked laser stability and power scaling. The objective of this thesis is to demonstrate a kind of a roadmap towards ultrashort pulse generation in the 2 μm spectral range by mode-locked Tm and Ho lasers that could be useful for the above discussed applications. Besides the laser material, another cavity element of crucial importance to shorten the pulse duration and realize this objective is the saturable absorber which initiates and sustains mode-locked operation ensuring long-term stability against noise and fluctuations. There is, however, a second important reason to include separate introductory chapters devoted to the laser materials and saturable absorbers employed in the present work: All of them were provided by different collaboration partners (from China, Spain and Germany for the laser crystals and ceramics, and from Finland and South Korea for the semiconductor and carbon nanostructures). On one hand, the exclusive access to these materials and structures was instrumental in achieving results beyond the state-of-the-art. On the other hand, all of them exhibit some novel features in relation to the spectral range of application and are still in a development stage, with ongoing characterization and optimization by the research groups manufacturing them, for which a feedback from laser experiments is of major importance. Therefore, all the resulting publications are joint works with the researchers who supplied these components: Without them the present PhD work would be impossible to realize.

The thesis begins with Chapter 2 which gives an overview of the active dopant ions and the host materials for the 2 μm spectral range, including energy level schemes of the $Tm^{3+}$ and $Ho^{3+}$ ions, the processes of excitation, emission and different interactions between the ions. Then three families of hosts and in particular specific representatives of them are presented and compared in terms of polarized absorption, emission and gain cross sections as well as upper state lifetime. These spectroscopic results are directly related to the main experimental part of the dissertation which is devoted to the mode-locking of 2 μm solid-state lasers because exactly the same materials, including isotropic ceramics, uniaxial and biaxial crystals with Tm and Ho doping, are employed there as active elements in the laser setup.

Chapter 3 explains the principle of operation of relevant saturable absorbers which represent the key cavity element to transform a CW solid-state laser into an ultrafast laser by locking the phase of the longitudinal modes through a "passive" method, i.e. by the evolving pulse itself. Special emphasis is given to the saturation and relaxation behavior of those saturable absorbers that are employed in the mode-locking experiments, which include semiconductors and carbon nanostructures, i.e. single-walled carbon nanotubes (SWCNTs) and graphene. All known parameters and characteristics of the saturable absorbers used later on are summarized in this chapter.

The specific saturation behavior of the laser materials and the saturable absorbers applied in the 2-μm spectral range is essential for understanding the mode-locking regime which is realized in such solid-state lasers. That is why these chapters precede the presentation of the different mode-locking techniques in Chapter 4. Chapter 4 first provides a brief theoretical background of passive mode-locking explaining the differences and the advantages with respect to active mode-locking (and also the possibility of Q-switching), including all the pulse shaping mechanisms and their role in the formation of the steady-state. Special emphasis is given here to the effects of group velocity dispersion and its compensation as well as the self-phase modulation. These two effects show some peculiarities in the 2 μm spectral range (e.g., compared to shorter wavelengths, the dispersion may be anomalous and the self-phase modulation is expected to be much weaker far from the material band-gap), however, the differences are basically quantitative.

Then a model of steady-state passive mode-locking is presented in Chapter 4 based on the assumption of slight changes of the pulse parameters in each of the cavity elements, leading to an equation widely known in the literature as Haus master equation. This equation can be used for analytical and numerical modeling of many types of passively mode-locked laser systems and while steady-state modeling of the obtained results goes beyond the scope of the present work, it is essential to show that there is a theoretical background for the pulse shapes normally assumed when measuring the pulse durations of ultrashort pulses by the autocorrelation technique. Three most important passive mode-locking concepts are subsequently discussed which are related to the spectroscopic properties of the laser medium and the saturable absorber. The mode-locked lasers considered in the present work belong to one of them. A brief insight into soliton-like pulses and their properties is presented, both in the narrow sense including self-phase modulation and anomalous dispersion, and also in the

more general case with all pulse shaping effects present in the laser model. Finally, the stability of the steady-state mode-locking regime as well as methods that can ensure such stability are discussed. This concerns Q-switching instabilities and pulse break-up, both of which were encountered in the experimental part. Special emphasis is given here to a fundamental soliton bound-state (two pulses at a separation comparable to their duration) because this really exotic effect has been experimentally observed, too.

Chapter 5 can be considered as the main body of this dissertation because it summarizes the essential experimental results achieved in the present work with passively mode-locked bulk Tm and Ho lasers emitting near 2 μm. The common laser cavity is described first together with all the relevant elements, pump sources and diagnostic tools. Then all the experimental results with the different materials are presented and discussed in terms of pulse duration, spectral width, average output power, stability, etc. These include picosecond, sub-picosecond and femtosecond operation culminating in the generation of the shortest pulses so far from a 2 μm bulk solid-state laser which were below 100 fs. Wherever possible, soliton-like pulse-shaping is analyzed as well as the existence of multi-pulses and bound states. Chapter 5 ends with a table where the obtained results are compared with literature data on mode-locked solid-state lasers with respect to all the essential output characteristics.

The final Chapter 6 provides a summary of the achievements and gives an outlook on their possible extensions and direct applications in the near future.

As already mentioned, the major contributions of the present work are found in Chapter 5 where the author had the leading role in all experiments. However, some additional contributions are included also in Chapter 2: They concern spectroscopic properties, anisotropy, identification of orientation, and in general characterization of some of the laser materials as explained in the corresponding places. In the end of the Dissertation, after the list of references, a list of publications is included which were used as a basis when writing the present text and where more detailed information can be found on the different subjects. An additional list contains all publications that appeared in the period of the PhD work but which finally remained outside the scope of the thesis.

# Chapter 2
# $Tm^{3+}$ and $Ho^{3+}$ doped laser active materials

Laser active materials must exhibit sharp fluorescent lines, strong absorption bands and high quantum efficiency for the fluorescent transition of interest: Solids with such properties are crystals, ceramics or glasses that incorporate in small amounts elements in which optical transitions can occur between different states. In the near-IR spectral range from 0.7 to 3 μm, coherent sources based on laser emission from solids (solid-state lasers or SSLs) rely on emission from two kinds of ions: transition metals (TM), such as chromium ($Cr^{3+}$, $Cr^{4+}$, $Cr^{2+}$) and titanium ($Ti^{3+}$), and trivalent lanthanide ($Ln^{3+}$) ions including ytterbium ($Yb^{3+}$), neodymium ($Nd^{3+}$), erbium ($Er^{3+}$), thulium ($Tm^{3+}$) and holmium ($Ho^{3+}$), as shown in Fig. 2.1.

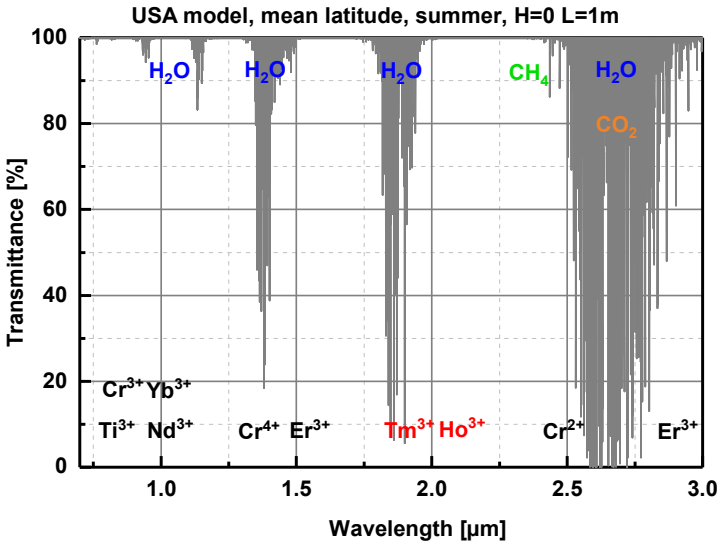


Fig. 2.1 Laser emission of different ions in the near-IR (0.7-3 μm). The gray line shows the air transmission at normal conditions, calculated from the HITRAN database for a path length of 1 m.

TM lasers are characterized by strong interaction of electronic transitions with phonons – vibrational-electronic (vibronic) interaction – which leads to large laser gain bandwidth. More phonons can be emitted or phonon absorption can be involved in optical transitions. Vibronic lasers are widely tunable lasers, called in the past also phonon-terminated SSLs. Most Ln lasers are NOT vibronic lasers. Nevertheless, phonons play other important roles in Ln lasers: They lead to fast thermalization within Stark level manifolds and fast non-radiative transitions between close manifolds. In many cases, such fast non-radiative transitions are essential for pumping and/or for depopulating the lower laser level.

The ground state electronic configuration of the Ln atom consists of a core that is identical to xenon, plus additional electrons in higher orbits. In Xe, the shells n=1,2,3 are completely filled, the shell n=4 has its s, p, and d subshells filled, whereas the 4f subshell

capable of accommodating 14 electrons is empty. However, the n=5 shell has acquired its first 8 electrons which fill the 5s and 5p orbits: $1s^2 2s^2 2p^6 3s^2 3p^6 3d^{10} 4s^2 4p^6 4d^{10} 5s^2 5p^6$.

Table 2.1 Electronic configurations of the Ln atoms (57-71) and some $Ln^{3+}$-ions. Not all Ln-ions have optical transitions to be considered as laser-active. Some Ln-ions such as Gd and Lu are "passive" and thus more suited for host compounds to be substituted by an active dopant ion, preferably a neighbor in the periodic table.

| No. | Chemical element | Number of electrons in shells n=1,2,3,4,5,6 | $Ln^{3+}$-ion configuration |
|---|---|---|---|
| 54 | Xenon | 2, 8, 18, 18, 8 | |
| 55 | Caesium | 2, 8, 18, 18, 8, 1 | |
| 56 | Barium | 2, 8, 18, 18, 8, 2 | |
| 57 | Lanthanum | 2, 8, 18, 18, 9, 2 | |
| 58 | Cerium | 2, 8, 18, 19, 9, 2 | |
| 59 | Praseodymuim | 2, 8, 18, 21, 8, 2 | |
| 60 | Neodymium | 2, 8, 18, 22, 8, 2 | $Nd^{3+}$: $[Xe]4f^3$ |
| ... | ... | ... | ... |
| 67 | Holmium | 2, 8, 18, 29, 8, 2 | $Ho^{3+}$: $[Xe]4f^{10}$ |
| 68 | Erbium | 2, 8, 18, 30, 8, 2 | $Er^{3+}$: $[Xe]4f^{11}$ |
| 69 | Thulium | 2, 8, 18, 31, 8, 2 | $Tm^{3+}$: $[Xe]4f^{12}$ |
| 70 | Ytterbium | 2, 8, 18, 32, 8, 2 | $Yb^{3+}$: $[Xe]4f^{13}$ |
| 71 | Lutetium | 2, 8, 18, 32, 9, 2 | |

The number of 4f electrons in Ln atoms increases from 1 (Ce) to 14 (Yb, Lu). The sharp fluorescence lines in $Ln^{3+}$ ions result from the fact that the 4f electrons involved in optical transitions are shielded by the outer shells (5s, 5p) from the surrounding crystal lattice. The corresponding transitions are similar to those in the free ions.

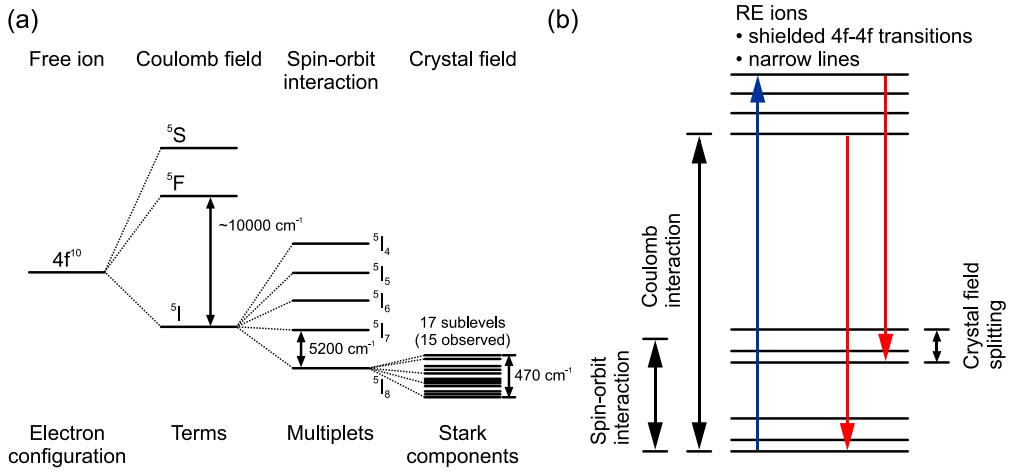


Fig. 2.2 Energy level scheme of $Ho^{3+}$ in YSGG ($Y_3Sc_2Ga_3O_{12}$, a garnet crystal) (a) and magnitude of the different splitting mechanisms in $Ln^{3+}$ ions (b). Note that pump and laser transitions in Ho and Tm lasers are intra-configurational (i.e. within $4f^{10}$ and $4f^{12}$, respectively).

In Ln ions, the Coulomb and spin-orbit interactions are similar in magnitude and the crystal field splitting acts as a small perturbation, see Fig. 2.2. In TM ions, the crystal-field splitting dominates the spin-orbit splitting: The optical transitions are 3d-3d in the outer shell and the vibronic character is much stronger (e.g. $Ti^{3+}$:sapphire), however, there exist also narrow lines (R-lines in $Cr^{3+}$:$Al_2O_3$ or ruby) or combination of narrow-band and vibronic transitions ($Cr^{3+}$:$BeAl_2O_4$ or alexandrite), with all these examples in the same spectral range.

Which of the Ln ions are more vibronic and why? A complete theoretical treatment is not available [15] but at least the spectroscopy confirms that the vibronic character tends to increase for active ions towards the end of the $Ln^{3+}$ series: $Yb^{3+}$, $Tm^{3+}$, etc. The question is also not very precisely formulated because more than one electronic transitions exist in many Ln ions and the situation for them might be different. However, the answer to this question remains important because ultrashort pulse (ps and fs) SSLs can be built only with broadly tunable active media, i.e. partly vibronic materials. In cases when the laser transitions are narrow-band, e.g. $Nd^{3+}$ or $Er^{3+}$, fs pulses can only be produced with glass hosting these ions.

Air absorption and in particular water absorption as indicated in Fig. 2.1 define important applications of SSLs. The latter can be based on material absorption but also on the absence of such absorption, e.g. the $Er^{3+}$ transition at 1.6 μm for telecommunications. $Er^{3+}$ lasers emitting near 3 μm are widely used e.g. in medical applications but the penetration depth is too low for minimally invasive surgical treatment. Near 2 μm, even the small difference in the wavelength between Tm-lasers (emitting in general below 2 μm) and Ho-lasers (slightly above 2 μm) can play a significant role [3].

In this work the main interest is exactly in this same wavelength range near 2 μm but the motivation comes from a different kind of applications which require ultrashort (ps and fs) pulses, as explained in the Introduction. $Tm^{3+}$ and $Ho^{3+}$ ions and in particular their transitions to the ground state (i.e. the ~ 2 μm transitions) offer nowadays the most attractive properties for laser operation in this spectral range. Indeed, continuous-wave (CW) and pulsed, i.e. in the Q-switched (QS) or mode-locked (ML) regimes which will be explained in Chapter 4, operation of such lasers, in particular under laser-diode pumping, has been drawing increasing attention over the last two decades [16, 17].

Table 2.2 Ln-ion transitions for which mode-locked lasers have been demonstrated in the ps or fs regimes. The right column shows typical optical sources employed for pumping (LD: laser diode, SH: second harmonic, FH: fourth harmonic, OPSL: optically pumped semiconductor laser).

| Laser ion | Laser wavelengths | Emission range | Pump source |
|---|---|---|---|
| $Nd^{3+}$ | 0.9 μm, 1.06 μm, 1.3 μm | near-IR Ln lasers | AlGaAs LD |
| $Yb^{3+}$ | 1.0−1.1 μm | | InGaAs LD |
| $Tm^{3+}$ | 2 μm | | AlGaAs LD or Tm |
| $Ho^{3+}$ | 2 μm | | AlGaIn-AsSb LD or Tm |
| $Er^{3+}$ | 1.6 μm, 3 μm | | Yb-Er or InGaAsP LD |
| $Pr^{3+}$ | 0.52 μm, 0.60 μm | Visible Ln lasers | (InGa)N LD or SH OPSL |
| | 0.64 μm, 0.72 μm | | |
| *$Ce^{3+}$ | 0.3 μm | UV Ln lasers | GaN LD or FH Nd |

*Inter-configurational, electric-dipole allowed transition, with characteristics similar to laser dyes.

It shall be mentioned that in the past also so-called color-center SSLs were employed for the generation of ultrashort pulses near 2 µm [18] but they have lost their importance because of the cryogenic temperatures required. Nowadays, in addition to SSLs, also parametric frequency down-conversion in nonlinear crystals from the 1-µm spectral range (Nd- and Yb-lasers) or the 800-nm range (Ti:sapphire laser) can be used to obtain ultrashort pulses near 2 µm, however, at the cost of greatly increased complexity of such systems. Table 2.2 summarizes the Ln ion transitions on which mode-locking has been demonstrated to generate ultrashort pulses and indicates the pump sources employed in each case.

When $Tm^{3+}$ and $Ho^{3+}$ ions are introduced into the laser host, the electric crystal field produces a Stark-splitting. The relevant laser transitions ($^3F_4 \rightarrow {}^3H_6$ for $Tm^{3+}$ and $^5I_7 \rightarrow {}^5I_8$ for $Ho^{3+}$) of these two ions for the 2-µm emission both end in the upper Stark levels of the ground state manifold. Thus, lasing is described using a so-called quasi-3-level model.

In this chapter, the energy level schemes of $Tm^{3+}$ and $Ho^{3+}$ are discussed first, including the processes of excitation, emission and different interactions between the ions. Then representatives of three different families of hosts, which are employed in the laser experimental part, are presented in more detail, with emphasis on their spectroscopic properties such as polarized absorption, emission and gain cross sections as well as the upper state lifetime.

## 2.1 Energy level schemes of $Tm^{3+}$ and $Ho^{3+}$ ions

Population inversion between the upper and lower levels of a laser transition is essential for laser amplification and more than two energy levels are needed to achieve this. Most lasers usually operate in one of the three fundamental schemes: 4-level scheme, 3-level scheme and quasi-3-level scheme, as shown as Fig. 2.3. The ruby laser ($Cr^{3+}$:$Al_2O_3$) is an example of a 3-level scheme [19].The threshold pump power is high in this case since population inversion can be achieved only when more than half of the ions are excited into the upper laser level. In the 4-level scheme, typical for Nd-lasers operating on the 1.06 µm transition, the threshold can be much lower since the lower laser level is not populated; in the lasing state, fast non-radiative decay from this level to the ground state will keep the population inversion.

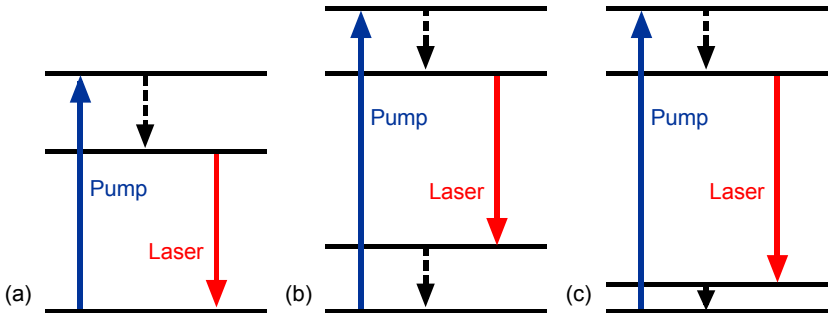


Fig. 2.3 Energy level diagrams for different laser schemes: (a): 3-level scheme, (b): 4-level scheme, (c): quasi-3-level scheme. Dashed arrows indicate fast non-radiative decay processes.

As most of the Ln ion transitions included in Table 2.2, the relevant 2-μm transitions in $Tm^{3+}$ and $Ho^{3+}$ ions can be described as quasi-3-level schemes, which is a kind of intermediate case. The lower laser level is an upper Stark component of the ground state manifold with appreciable population at the operating temperature. Typically, 2% of the ions can be in the lower laser level at room temperature. This leads to several features which are specific for quasi-3-level lasers:

- Weakly pumped regions of the gain medium still cause some reabsorption loss at the laser wavelength and higher pump intensities are needed, achievable only with high brightness pump sources.
- The spectral shape of the optical gain depends on the excitation level because of the reabsorption. As a consequence, the laser wavelength depends on the cavity losses as well as the doping concentration. High cavity losses or low doping concentration require a higher inversion: The maximum gain shifts then to shorter wavelengths.

The above consideration follows the most widespread classification in the existing literature but is only qualitative. Pronounced 3-level behavior is inevitable for gain media with a very small quantum defect (QD = $1-\lambda_P/\lambda_L$, where the subscripts P and L stand for the pump and laser wavelengths; QD determines the maximum possible laser efficiency), because this enforces a small energy spacing between the lower laser level and the ground state, so that thermal population of the lower laser level is significant. The transition between 4- and 3-level systems can be smooth and the extent of being a 3-level-system depends on the exact laser wavelength and operating temperature. The systematics of such schemes can be in fact quantified with precise definitions of quasi-2-, quasi-3-, and quasi-4-level schemes [20].

The relevant energy level scheme for the $Tm^{3+}$ ion is shown in Fig 2.4a. Excitation of Tm lasers is usually at $\lambda_P \sim 800$ nm ($^3H_6 \rightarrow {}^3H_4$ transition), which matches very well the emission of AlGaAs laser diodes. Laser operation is achieved typically at $\lambda_L \sim 1.95$ μm due to the $^3F_4 \rightarrow {}^3H_6$ transition. This results in a low Stokes efficiency, $\eta_{St} = \lambda_P/\lambda_L \sim 0.41$. However, a special feature of the $Tm^{3+}$ system is the very strong cross-relaxation (CR) mechanism for two adjacent ions, $^3H_4 + {}^3H_6 \rightarrow {}^3F_4 + {}^3F_4$ [21]. This non-radiative process ideally generates two photons at ~ 1.95 μm from only one pump photon at ~ 0.8 μm, resulting in a much higher $\eta_{St}$ of $2\lambda_P/\lambda_L \sim 0.82$. Laser operation with strong CR is very desirable for increase of the efficiency and reduction of the heat load. The latter can be estimated as $\eta_h = 1 - 2\lambda_p/\lambda_L \sim 0.18$ which is lower than for $Nd^{3+}$ ions ($\eta_h \sim 0.24$) pumped at the same wavelength. The efficiency of the CR process strongly depends on the doping concentration ($\sim N^2$) since the involved dipole-dipole interaction probability depends on the ion spacing [22]. For many $Tm^{3+}$-doped materials, a very high CR efficiency for reasonable $Tm^{3+}$ doping concentrations (3-5 at. %) has been demonstrated and, consequently, a high laser efficiency has been achieved. It is also possible to pump the $^3F_4$ energy level directly between 1.7 and 1.8 μm (in-band pumping), but no well-developed pump sources suitable for this exist.

CR is only one of the few non-radiative energy-transfer (ET) processes in which no emission / absorption of a photon is involved. In the opposite direction, up-conversion (UC)

processes occur. Starting from the upper laser level, UC processes are phonon assisted. One such process is the reverse of the mentioned CR process, i.e. $^3F_4 + {}^3F_4 \rightarrow {}^3H_4 + {}^3H_6$ which leads to UC fluorescence (UCF) from $^3H_4$ but it introduces negligible losses. The other UC process from this level is $^3F_4 + {}^3F_4 \rightarrow {}^3H_5 + {}^3H_6$ and in this case the excitation of one ion is lost. The $^3H_5$ state has a very short lifetime and is depopulated by a non-radiative process $^3H_5 \rightarrow {}^3F_4$ which generates heat in the crystal.

Excited-state absorption (ESA) is another important process limiting the performance of Ln SSLs. ESA results in a depopulation of the pump level or emitting state with the excitation of the Ln ions to higher-lying multiplets and leads to UCF processes. Non-radiative or radiative transitions from these multiplets result in an additional heat load and decrease the laser efficiency. ESA of laser photons may occur also from $^3F_4$ to $^3H_4$ or from $^3H_4$ to $^1G_4$. When pumping $Tm^{3+}$ ions at ~ 800 nm, $^3H_5 \rightarrow {}^1G_4$ ESA may be observed. As a result of the population of the $^1G_4$ higher-lying multiplet (~ 21500 $cm^{-1}$), several visible up-conversion emissions occur at ~ 480 nm (to the $^3H_6$ ground-state, observed in the blue), at ~ 650 nm (to the $^3F_4$ state, in the red) and at ~ 800 nm (to the $^3H_5$ state, in the near-IR). As the energy gap between the $^3F_{2,3}$ states and the lower-lying $^3H_4$ pump state is small (~ 2000 $cm^{-1}$), a fast non-radiative relaxation suppresses any additional parasitic emissions. UCF in singly $Tm^{3+}$-doped materials is relatively weak.

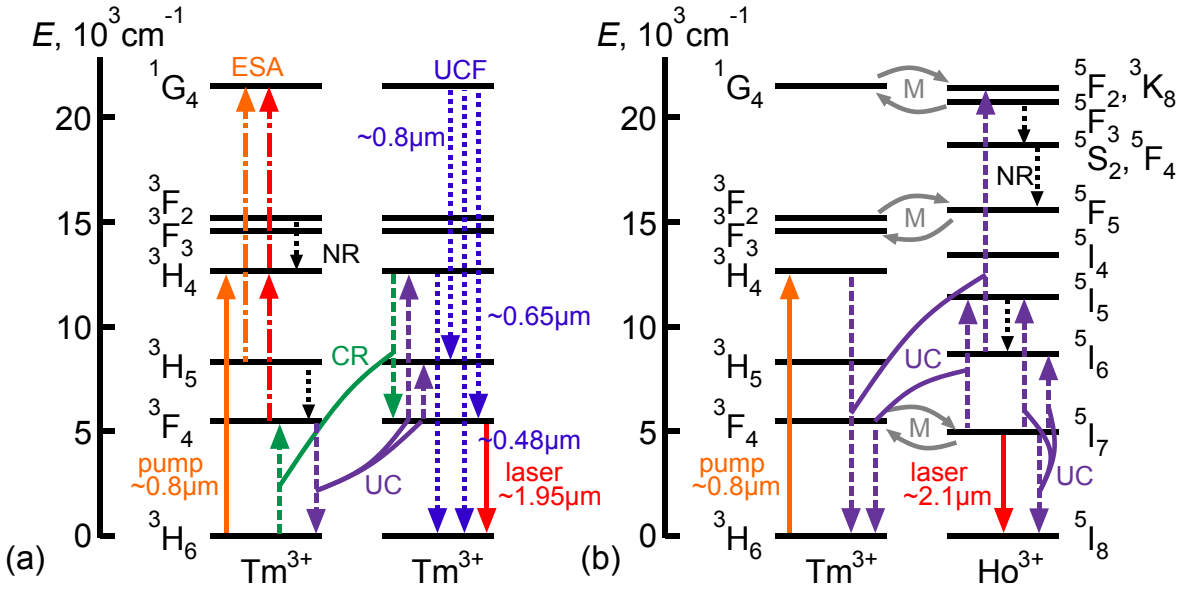


Fig. 2.4 Detailed energy level diagrams of the $Tm^{3+}$ ion (a) and of $Tm^{3+}$ and $Ho^{3+}$ ions (b) indicating the resonant excited levels: UC – up-conversion, UCF – UC fluorescence, ESA – excited-state absorption, CR – cross-relaxation, M – migration, NR – non-radiative relaxation. In (a), all processes exist in both ions but for clarity they are arbitrarily distributed between the two.

Considering a fast and efficient CR mechanism for highly $Tm^{3+}$-doped laser materials, one can neglect the population of all multiplets with the exception of the $^3H_6$ ground state ($N_1$) and the $^3F_4$ upper laser level ($N_2$), so that $N_1 + N_2 \approx N_{Tm}$ where $N_{Tm}$ is the $Tm^{3+}$ concentration.

The $Ho^{3+}$ ion exhibits no absorption bands in the emission range of standard laser diodes and Ho-lasers were mainly lamp-pumped in the past. At present, most attractive is in-band pumping into the upper laser level using high-power Tm-fiber lasers or AlGaIn-AsSb diodes at wavelengths slightly below 2 μm (Table 2.2). Co-doping with $Tm^{3+}$ is another method of pumping through an efficient migration (M), another ET process, between $Tm^{3+}$ ($^3F_4$) and $Ho^{3+}$ ($^5I_7$) ions: $^3F_4 + {}^5I_8 \rightarrow {}^3H_6 + {}^5I_7$, see Fig. 2.4b. Typically, at optimum co-doping and room temperature, about 50% of the excitation energy can be transferred to the $Ho^{3+}$ ions, the rest of the energy is stored in excited $Tm^{3+}$ ions.

The Ho-laser emission around 2 μm is a result of the $^5I_7 \rightarrow {}^5I_8$ transition. UC processes exist in $Ho^{3+}$, too. In Fig. 2.4b two such phonon-assisted UC processes are indicated: $^5I_7 + {}^5I_7 \rightarrow {}^5I_6 + {}^5I_8$ and $^5I_7 + {}^5I_7 \rightarrow {}^5I_5 + {}^5I_8$. They become important at high inversion levels. In co-doped crystals, CR processes occur also between $Tm^{3+}$ and $Ho^{3+}$ ions and there are M processes also between other higher-lying excited states, cf. Fig. 2.4b.

$Ho^{3+}$ ions show somewhat narrower optical bands, more structured compared to $Tm^{3+}$ because of the lower number of 4*f* electrons. However, Ho-lasers are still very attractive for ultrashort pulse generation because the pump scheme offers more options for power scaling.

## 2.2 Host materials

Host materials can be classified as crystals, glasses and ceramics. Crystals belong to one of the 32 symmetry classes (point groups) which are grouped in 7 crystal systems. From the point of view of linear optics, crystals are isotropic (cubic), uniaxial (trigonal, tetragonal and hexagonal), and biaxial (orthorhombic, monoclinic and triclinic). For electric dipole transitions in birefringent crystals the interaction of the dopant ion with light depends only on the polarization but not on the propagation direction.

The absorption and emission probabilities are described in terms of interaction cross-sections. The meaning of the absorption cross-section for instance can be easily understood from the Lambert-Beer law (transmission $T = I/I_0 = e^{-\alpha}$), where the dimensionless absorption coefficient is given by $\alpha = \sigma_a(\lambda)NL$ ($L$: sample length). The factor $\sigma_a(\lambda)$ has a dimension of area ($cm^2$). It can be interpreted as the probability of a photon to hit an ion which may be viewed as a 'target' with such area. The larger the cross section, the higher the probability that the 'target' will be hit.

In uniaxial crystals, the spectroscopic notations are σ for light polarization perpendicular to the optic axis *c* and π for polarization parallel to the optic axis *c*. The interaction cross-sections depend on the wavelength: For one and the same electronic transition they can be higher for one of these polarizations at a certain wavelength but the situation may be reversed at a different wavelength. Obviously, maximum cross-sections may occur also at some intermediate polarization. Nevertheless, to avoid polarization rotation effects leading to cavity losses, one usually selects the laser polarization to be one of the two principal polarizations, σ or π. Normally it is the one that ensures higher gain but in a mode-locked laser it can be also the one providing larger bandwidth. If π polarization is selected, the active element has the so-

called *a*-cut (propagation along one of the two *a*-axes). If σ polarization is selected, the cut can be either *a*-cut or *c*-cut and the exact choice may depend on other anisotropic properties such as thermal conductivity which determines the cooling efficiency.

Also the pump polarization might have to be taken into account because although in many cases it coincides with the laser polarization (when the active element is uncoated and inclined under Brewster's angle to prevent Fresnel reflection losses), laser diodes used for pumping are often unpolarized when coupled into fibers and antireflection (AR) coated elements used at normal incidence are preferable. The polarization dependence of the crystal absorption is different from the one of the emission and in this case one can select the configuration that ensures higher overall pump absorption.

From Maxwell's equations one can derive that in a crystal there can be zero, one or two optic axes in the sense that for propagation along these special directions the index of refraction is independent of the polarization direction [23]. The two optic axes in biaxial crystals are important for some effects (e.g. in polarization rotators) but do not play an essential role in laser physics or nonlinear optics. Instead, the so-called dielectric frame is considered here, also known as the frame of the optical ellipsoid or optical indicatrix [23]: It is the orthogonal eigenframe of the tensor of the linear electric susceptibility which will be defined in Chapter 4. The corresponding 3 axes are designated as principal axes; they span 3 principal planes, and the 3 refractive indices are called principal refractive indices. In the principal planes, biaxial crystals are considered in a similar way as uniaxial crystals but the nomenclature is different for laser and nonlinear crystals although this can be exactly the same crystal. For laser crystals, the old notation $N_p$, $N_m$, and $N_g$ is still most popular to designate the 3 orthogonal axes of the optical ellipsoid where per definition $n_p<n_m<n_g$ holds for the three principal refractive indices. Spectroscopic properties are reported for the three principal polarizations along these axes. As in uniaxial crystals, the laser polarization is chosen along one of these principal optical axes while propagation is along one of the remaining two axes and the latter choice does not affect the interaction cross-sections. In orthorhombic crystals the dielectric frame $N_pN_mN_g$ coincides with the orthogonal crystallographic frame *abc* and only the correspondence of the axes has to be determined. In monoclinic crystals, however, in which *abc* is not an orthogonal frame, only one of the dielectric axis coincides with the monoclinic axis which is normally designated as *b* (the axis which is perpendicular to the plane spanned by the other two: Depending on the symmetry, this is a two-fold crystallographic axis for point group 2, an axis perpendicular to the mirror plane in point group *m* or both in point group 2/*m*). The remaining two dielectric axes are rotated at some angles from the *a*- and *c*-axes which cross at the monoclinic angle β (per convention $\beta \geq 0$ and $c_0 < a_0$ holds for the lattice constants). These angles depend on wavelength and temperature but normally the position of the dielectric frame relative to the crystallographic frame can be assumed to be fixed [24]. Illustrating examples follow in this chapter when describing the laser crystals employed in the present work.

Crystalline laser hosts are also divided into ordered and disordered [25]. In ordered crystals the passive ion (most often a trivalent rare-earth, RE, i.e. $Sc^{3+}$, $Y^{3+}$ or $Ln^{3+}$ including

$La^{3+}$) to be substituted by the $Ln^{3+}$ dopant occupies only a single lattice site. In disordered crystals one lattice site can be occupied by different host cations, e.g. with 50% $Na^{+}$ and 50% $Gd^{3+}$ in $NaGd(WO_4)_2$, but in a random distribution for the first cationic sphere of neighbors or there can be two different crystallographic sites that can accommodate both the monovalent and the trivalent cations but in general with different occupancy factors. Disordered crystals can be obtained also by mixing two ordered crystals containing different passive RE ions such as $Gd^{3+}$ and $Lu^{3+}$, e.g. $KGd_xLu_{1-x}(WO_4)_2$. In all cases the active Ln dopant ion which substitutes the passive RE host ion experiences a locally variable crystal field which is manifested in the large bandwidths of the spectral lines of the electronic transitions, the so-called inhomogeneous line broadening in laser physics. With regard to their spectroscopic but also opto-mechanical properties, such disordered crystals occupy an intermediate position between ordered laser hosts and glasses which are characterized by only short-range order (no local disorder and no long-range order). Disordered crystals are important for mode-locked lasers because they provide larger gain bandwidths supporting shorter pulses, however, their thermal conductivity is lower. Glasses ensure the broadest absorption and gain bandwidths but they exhibit also lowest thermal conductivity and for this reason have lost their importance in the 2-µm spectral range. This is true, however, only for bulk glasses. In $Tm^{3+}$ or $Ho^{3+}$ optical fibers, where the thermal load problem is solved by heat distribution across a very large fiber length and surface, they are real alternatives to bulk lasers.

Polycrystalline ceramics consist of fine, randomly oriented microcrystals with sizes ranging from submicron to several tens of micrometers. The development of Ln ion doped crystals is slowed down by the expensive, complex and time consuming growth in comparison with the simpler and relatively fast ceramic approach. Since growth of large crystals is technologically limited, laser power or energy scaling are also limited. Furthermore, a composite laser medium is essential to improve laser performance. Large aperture, minimal losses, high optical homogeneity, good thermo-mechanical properties in combination with adequate spectroscopic properties, and cost effectiveness, are requirements that are impossible to satisfy simultaneously with the existing crystals applied in SSL systems. While glasses, which are scalable in size, with their roughly an order of magnitude lower thermal conductivity are restricted to low repetition rate and average power applications, laser ceramics seem to offer a combined solution to all these challenges. The main features of the ceramic laser technology can be summarized as: (i) Scalability, i.e. increasing the size of the active elements in a cost-effective manner while preserving the optical uniformity, (ii) Multifunctionality, because fabrication of multifunctional elements is possible by the bonding technique which is easy to adapt to this technology to produce composite elements or functionally graded materials by adjusting the doping concentration (which can be in general higher than in crystals) and chemical composition, and (iii) Mass production, similar to that of glass. Transparent laser ceramics exhibit optical and thermal properties similar to those of single crystals but their fracture toughness and damage resistivity are superior. In general, most ceramics are opaque. The reason is simple: Translucent ceramics contain many scattering sources, such as grain boundary phases, residual pores and secondary phases, which

cause significant scattering losses. The real technological breakthrough came in the 1990s, with the use of submicron- to nano-sized raw materials [26]. It should be outlined that it makes sense to use only isotropic (cubic) materials for fabrication of laser ceramics due to the random grain orientation. The spectroscopic properties of doped laser ceramics are considered to be similar to those of the corresponding crystals although accurate characterization is available only in rare cases.

Transitions occurring between levels inside the 4f subshell are in fact electric-dipole forbidden by the Laporte selection rule which says that states with even parity can be connected only with states of odd parity, and odd states only with even states. Although magnetic dipole and electric quadrupole radiative transitions are allowed, with few exceptions the $Ln^{3+}$-transitions are still of electric-dipole type because the crystalline fields in solids distort the electronic motion so that the selection rules for free ions no longer apply. This effect is produced, however, only by non-centrosymmetric crystal fields, which emphasizes the importance of the local site symmetry [27]. The local symmetry determines the number of sublevels that can be expected as a result of the Stark splitting while the local field strength determines the magnitude of the splitting.

The ground-state absorption (GSA) cross-sections of $Tm^{3+}$ and $Ho^{3+}$-doped materials are measured simply by transmission spectroscopy (spectrophotometer) using a broadband halogen lamp as the source and samples oriented for the corresponding polarization. The intensities are low and no depletion of the ground state occurs, thus the absorption cross-section $\sigma_a$ is derived from the Lambert–Beer law. A powerful theoretical tool exists, the Judd-Ofelt method, which allows one to calculate the radiative transition probabilities and the branching ratios as well as lifetimes for spontaneous emission for different inter-manifold (i.e. manifold to manifold) transitions from accurate measurements of the entire GSA spectrum [27]. It is based on static, free-ion and single configuration approximations with some additional assumptions. In the static model, the central ion is affected by the surrounding host ions via a static electric field, referred to as ligand or crystal field. In the free-ion model, the host environment produces the static electric field, and is treated as a perturbation to the free-ion Hamiltonian. In the single configuration model, the interaction of electrons between configurations is neglected. The results can be validated by comparing the branching ratios with fluorescence and lifetime measurements. The latter can be complicated by the presence of ET, non-radiative relaxation and reabsorption. Thus, directly measured lifetimes might be inaccurate even at lower temperature.

The emission cross-section $\sigma_e$ can be determined from polarized fluorescence measurements by the Füchtbauer–Ladenburg equation [17],

$$\sigma_e^i(\lambda) = \frac{\lambda^5 P_f^i(\lambda)}{8\pi n^2 c \tau_r \int P_f^i(\lambda)\, \lambda d\lambda},$$

where $P_f^i(\lambda)$ is the recorded fluorescence signal (power) in dependence on the wavelength for the *i*-th polarization, *n* is an average refractive index of the laser host, *c* is the speed of light,

and $\tau_r$ is the spontaneous (or radiative) lifetime of the level or manifold investigated. Apart from the fact that the value of $\tau_r$ is required, the main problem in the Füchtbauer–Ladenburg method is the reabsorption which affects the measured signal. Therefore, in quasi-3-level systems it is mainly applied in the long-wave wing of the emission, exactly where another method called the reciprocity method might be problematic. The reciprocity method requires GSA measurements for the laser transition for all polarizations. This method is based on the theory developed by McCumber [28] who considered quasi-3-level systems applying the Einstein relations for the rates of spontaneous and stimulated emission and absorption, with the levels in each manifold being in thermal equilibrium (i.e. Boltzmann distribution). The result reads [17]:

$$\sigma_{\mathrm{e}}^{i}(\lambda) = \sigma_{\mathrm{a}}^{i}(\lambda) \exp\left(-\frac{hc}{k_B T}\left(\frac{1}{\lambda} - \frac{1}{\lambda_\mu}\right)\right),$$

where the absorption cross-section $\sigma_{\mathrm{a}}^{i}(\lambda)$ was introduced before and the chemical potential wavelength is defined by: $\lambda_\mu = \frac{hc}{k_B T}(\ln\frac{Z_l}{Z_u})^{-1}$. Here $k_{\mathrm{B}}$ is the Boltzmann constant, $T$ is the temperature, $h$ is the Planck constant, and $Z_l$ and $Z_u$ are the partition functions of the lower and upper manifolds defined as $Z_m = \sum_k g_k^m \exp(-E_k^m/k_B T)$, $m = l, u$. $g_k^m$ is the degeneracy of the sublevel having the number $k$ and the energy $E_k^m$ measured from the bottom of the corresponding multiplet. Thus, the reciprocity method requires precise knowledge of all the individual Stark sublevels of the two manifolds. This problem has been circumvented in the modified reciprocity method [29] leading to the expression:

$$\sigma_{\mathrm{e}}^{i}(\lambda) = \frac{\exp\left(-\frac{hc}{k_B T\lambda}\right)}{8\pi n^2 \tau_r c \left\langle \int \lambda^{-4}\sigma_a(\lambda) \exp\left(-\frac{hc}{k_B T\lambda}\right) d\lambda \right\rangle} \sigma_{\mathrm{a}}^{i}(\lambda),$$

for the $i$-th polarization where $\langle\ \ \rangle$ denotes averaging over polarizations (the 3 principal polarizations in biaxial crystals or the π-polarization and 2 times the σ-polarization in uniaxial crystals). Note that, a combination of the Füchtbauer–Ladenburg and reciprocity methods, i.e. with $\sigma_e^i(\lambda)$ derived by the latter, provides an expression for the radiative lifetime $\tau_{\mathrm{r}}$ [17]:

$$\tau_r^{-1} = 8\pi n^2 c \left\langle \int \lambda^{-4}\sigma_{\mathrm{e}}(\lambda)\, d\lambda \right\rangle,$$

Similarly, a combination of the reciprocity and the modified reciprocity methods can also be used to determine the radiative lifetime $\tau_{\mathrm{r}}$ [29]:

$$\tau_r^{-1} = 8\pi n^2 c \left\langle \int \lambda^{-4}\sigma_{\mathrm{a}}(\lambda) \exp\left(-\frac{hc}{k_B T}\left(\frac{1}{\lambda} - \frac{1}{\lambda_\mu}\right)\right) d\lambda \right\rangle,$$

Vibronic interactions may compromise the accuracy of the reciprocity method [30].

As already mentioned, in quasi-3-level systems the maximum laser gain is determined not only by the emission but also by the reabsorption. This leads to the concept of the gain cross-section $\sigma_g = \beta\sigma_e - (1-\beta)\sigma_a$, where the inversion rate $\beta = N_1/(N_1+N_2) \approx N_1/N$ is approximately equal to the ion density in the upper laser level divided by the total ion density $N$ ( = $N_{Tm}$ or $N_{Ho}$). This parameter is simply plotted for different values of the inversion rate and serves to predict the laser wavelength in the CW regime because different cavity losses require different magnitude of the gain coefficient $\sigma_g NL$ where $L$ is the active medium length. Which polarization will dominate in anisotropic materials depends on the wavelength dependent gain cross-section. The latter is obviously sensitive to temperature. At lower temperatures quasi-3-level systems tend to behave as 4-level systems because reabsorption losses decrease but simultaneously the spectral linewidths get narrower which is disadvantageous for the generation of ultrashort pulses. At higher temperatures, there will be a reduction of the peak absorption cross-section, and linewidth broadening [31]. Spectroscopic cross-section data are available as a rule only at room temperature. In a quasi-3-level system laser, by changing the cavity losses one can control not only the wavelength of maximum gain (as already mentioned - decreasing with the losses) but also the gain bandwidth.

The experimentally measured lifetime is usually not the radiative lifetime $\tau_r$ but the harmonic mean value with the lifetime accounting for non-radiative processes $\tau_{nr}$:

$$\tau_f^{-1} = \tau_r^{-1} + \tau_{nr}^{-1} ,$$

Since this is the characteristic time with which the fluorescence signal decays, the time constant $\tau_f$ is called in laser physics the fluorescence lifetime. It depends on the concentration because at higher doping ion-ion interactions tend to reduce it (fluorescence quenching). For this reason the measurements are preferably performed with low-doped samples, which also eliminate ET effects. The results in the literature often vary a lot because the reabsorption effect, called also radiation trapping, is not properly taken care of and few techniques have been suggested to solve the problem. Two methods are mainly used to suppress this effect and the total internal reflection (i.e. fluorescence from inside the crystal which propagates at such large angles that it remains trapped in the crystal after reflection at the surface) both of which lengthen the intrinsic decay constant of an isolated ion: using powdered samples [32] or a pinhole on the bulk sample surface [33]. In the pinhole method the sample with the pinhole is inclined at 45° with respect to the excitation beam and detection takes place at 90° from the excitation beam. The overlap of the crystal region that is excited and the region that emits photons that can be detected scales up with the pinhole size. To eliminate the probability of re-emission the pinhole size is continuously decreased and the fluorescence lifetime is derived asymptotically from the measurements for zero pinhole size. To determine the intrinsic $\tau_f$ properly is essential on the first place for spectroscopic characterization of a new material and as explained above – for derivation of the emission and gain cross-sections. This is so because in Ln doped materials non-radiative relaxation can be normally neglected for the laser

transition. Then $\tau_r$ is approximated by the measured $\tau_f$. Experimentally measured values of $\tau_f$ can be compared with values of $\tau_r$ derived from the reciprocity method as explained above, which provides an estimate for the overall accuracy of the emission cross-section values [34]. Both results can be used also for validating the Judd-Ofelt method reliability. In a real laser, the effects of fluorescence quenching, reabsorption and stimulated emission all affect the actual fluorescence or energy storage lifetime which can be measured under operating conditions or estimated from the performance in the regime of active Q-switching (cf. Chapter 4) under CW pumping. It is then this time that enters different theoretical models.

### 2.2.1 YAG and LuAG

YAG ($Y_3Al_5O_{12}$) and LuAG ($Lu_3Al_5O_{12}$) (space group $Ia\bar{3}d$ or $O_h^{10}$, point group $m\bar{3}m$) are representatives of the big family of isostructural synthetic garnet crystals belonging to the cubic system, with general formula $A_3B_2(CO_4)_3$, where A = Ca, Y, or RE, B = Al, Sc, Ga, or Fe, C = Al, Ga, Ge, or Fe, the A-ion is located in 8-fold $O^{2-}$-coordinated sites with orthorhombic 222 local symmetry, B in octahedral sites, and C in tetrahedral sites. Garnets are one of the most popular and successful laser host materials for many of the $Ln^{3+}$ active dopants [25]. They are optically isotropic ordered crystals, known for their superior thermo-mechanical properties. The incorporation of Ln active ions is facilitated by the presence of RE passive ions in the lattice, Sc, Y, Gd or Lu. Since $Tm_3Al_5O_{12}$ and $Ho_3Al_5O_{12}$ belong to the same space group, the substitution can be up to 100% (complete solid solutions). However, in contrast to other dopants such as $Yb^{3+}$, unwanted interaction processes between excited ions as shown in Fig. 2.4, limit the doping level to much lower values and stoichiometric TmAG and HoAG lasers do not exist in contrast to YbAG. Thanks to their cubic structure, doped YAG and LuAG are both suitable for transparent laser ceramics [26]. Most of the best laser results in terms of CW or average power in the pulsed regime that can be found in the literature were obtained with Tm- and Ho-doped YAG crystals [3, 17].

Figures 2.5 and 2.6 show the absorption cross-sections for the pump transition measured in Tm:YAG ceramics, and the absorption, emission and gain cross-sections obtained for the laser transition [35]. The maximum absorption cross section for the $^3H_6 \rightarrow {}^3H_4$ transition is $\sigma_a$ = $7.7\times10^{-21}$ cm$^2$ at 786 nm. This value is very close to the one reported for single crystals, $7.5\times10^{-21}$ cm$^2$ at 785 nm [3]. The emission cross-section of Tm:YAG ceramics was calculated by the Füchtbauer–Ladenburg method approximating $\tau_r$ by $\tau_f$ (see below), giving a maximum $\sigma_e$ = $3.0\times10^{-21}$ cm$^2$ at 2.015 μm with a linewidth (FWHM) of 29.6 nm. This is higher compared to single crystals ($1.8\times10^{-21}$ cm$^2$ at 2.013 μm with a linewidth of ~ 28 nm [3]). Having in mind that more measurements on single crystals exist, which confirm the latter values, it can be concluded that further spectroscopic efforts are needed in order to obtain more reliable values for the emission cross-section. The fluorescence lifetime of a 4% Tm:YAG ceramic sample was measured by the pinhole method giving $\tau_f$ = 10 ms at room temperature [35], which agrees rather well with values known for single crystals (10-10.5 ms)

[3, 34]. In general, such characteristics indicate that the quality of the developed ceramics is comparable to that achievable with single crystals.

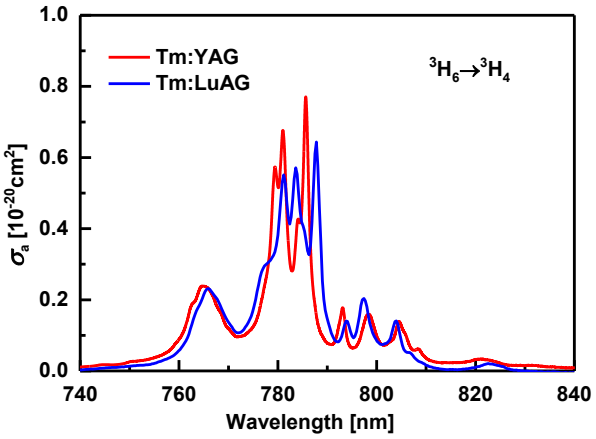


Fig. 2.5 Ground-state absorption (GSA) cross-section of Tm:YAG (red curve) and Tm:LuAG (blue curve) ceramics (reproduced from [20]).

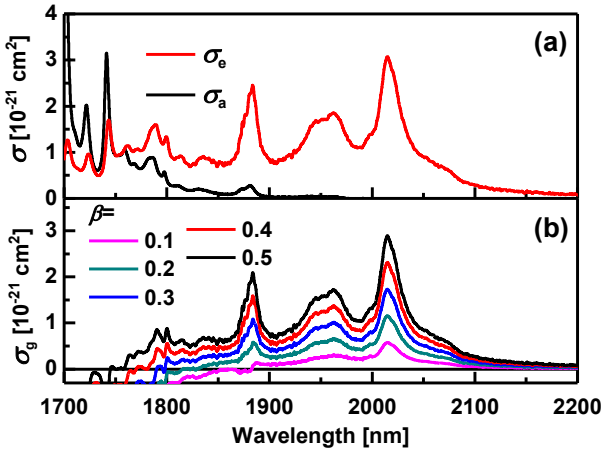


Fig. 2.6 Absorption, $\sigma_a$, and emission, $\sigma_e$, cross-sections (a), and calculated gain cross-section, $\sigma_g$, for different inversion rates $\beta$ (b) of Tm:YAG ceramics (remeasured data but very close to [20]).

LuAG is a similar host material but studied to a much lesser extent as a crystal. In the case of Tm-doping, one of its advantages is the weaker population of the lower laser level as a result of the stronger crystal field and Stark splitting [36]. As a consequence, the free running emission wavelength of Tm:LuAG is 2.023 μm, i.e. shifted by ~ 10 nm to longer wavelengths compared to Tm:YAG [3, 37], which matches much better to one of the atmospheric optical transmission windows. The Tm ionic radius in 8-fold coordination (0.994 Å) is closer to that of Lu (0.977 Å) compared to that of Y (1.019 Å) [38]. Thus one of the advantages of this host compared to YAG (as in other crystal families containing these two passive ions) is the possibility for higher doping (important to activate the CR process) without distortion of the crystal lattice and with weaker effect on the thermal conductivity. It is unclear, however, if this advantage is essential in ceramics as well.

In the literature, spectroscopic data are only available for Tm:LuAG single crystals [36, 37]. Here, the laser-relevant spectroscopic characterization of Tm:LuAG ceramics will be presented. The highest absorption cross-sections for the $^3H_6 \rightarrow {}^3H_4$ $Tm^{3+}$ pump transition amount to $6.43\times10^{-21}$ $cm^2$ at 783 nm and $5.71\times10^{-21}$ $cm^2$ at 787 nm. In single crystals the maximum $\sigma_a$ amounts to $5.7\times10^{-21}$ $cm^2$ at 788 nm [3, 37]. The emission cross-section $\sigma_e$ for the $^3F_4 \rightarrow {}^3H_6$ $Tm^{3+}$ laser transition was derived from the absorption cross-section $\sigma_a$ by the reciprocity method. Both cross-sections for the $^3F_4 \leftrightarrow {}^3H_6$ transition are shown in Fig. 2.7a. The maximum emission cross-section of the ceramics for the laser transition from the $^3F_4$ level to the ground state is $1.51\times10^{-21}$ $cm^2$ at 2.023 µm with a linewidth of 30 nm. It is only slightly lower compared to Tm:LuAG single crystals: $\sigma_e = 1.66\times10^{-21}$ $cm^2$ with a linewidth of 23 nm [37]. The calculated gain cross-section $\sigma_g$ for several values of the inversion rate $\beta$ is presented in Fig. 2.7b. For the $^3F_4 \leftrightarrow {}^3H_6$ $Tm^{3+}$ transition, the Tm:LuAG ceramics cross-sections are very similar to those of its single crystal counterpart [37]. The $^3F_4$ fluorescence lifetime of 10 ms measured for 4 at.% bulk Tm:LuAG ceramics at room temperature is also in good agreement with values reported for single crystals (10.9 ms) [37].

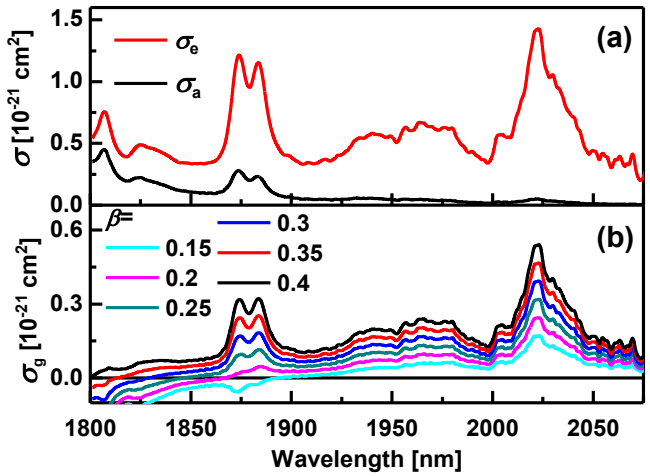


Fig. 2.7 Absorption, $\sigma_a$, and emission, $\sigma_e$, cross-sections (a) and gain cross-section, $\sigma_g$, for different inversion rates $\beta$ (b) of Tm:LuAG ceramics.

With regard to $Ho^{3+}$-doping, only YAG laser ceramics were available and considered in the present work. The maximum $\sigma_a$ for in-band pumping amounts to $9.8\times10^{-21}$ $cm^2$ at 1.9065 µm with a linewidth of 5.6 nm. In crystals, this value is $1.18\times10^{-20}$ $cm^2$ at 1.90765 µm with a linewidth of 5 nm [39]. In order to estimate the potential spectral extent of the gain in Ho:YAG ceramics, the gain cross-section was calculated for several values of the inversion rate $\beta$, as shown in Fig. 2.8b. The radiative lifetime $\tau_r$ of the upper laser level $^5I_7$ was estimated from the Judd-Ofelt modeling to be 7.7 ms [40]. The emission cross-section $\sigma_e$ was deduced from the absorption cross-section $\sigma_a$ (both shown in Fig. 2.8a) by the reciprocity method using the reported Stark splitting for Ho:YAG single crystals [41]. All spectroscopic results were very close to published data for single crystals [39]. The maximum $\sigma_e$ of the Ho:YAG ceramics for the $^5I_7 \rightarrow {}^5I_8$ $Ho^{3+}$ laser transition at 2.09 µm is $1.45\times10^{-20}$ $cm^2$. This

value is slightly higher compared to Ho:YAG single crystals at the same wavelength: $\sigma_e$ = $1.29\times10^{-20}$ $cm^2$ [39]. Comparing the gain cross-sections, the wavelength dependence is somewhat smoother in ceramics which is potentially advantageous for ultrashort pulses. For inversion rates $\beta$ < 0.2, emission of the free running Ho:YAG ceramic laser is expected at ~ 2.1215 µm, whereas for higher $\beta$ the maximum gain is at 2.09 µm (Fig. 2.8b).

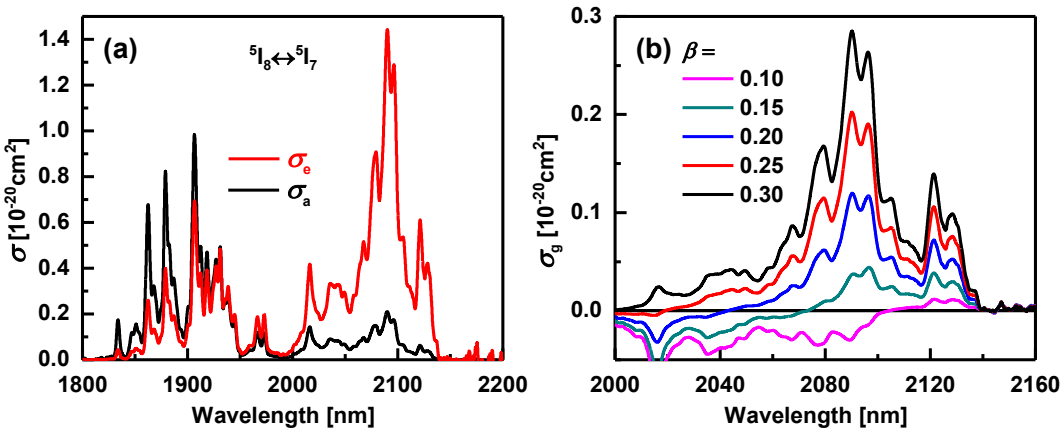


Fig. 2.8 Absorption, $\sigma_a$, and emission, $\sigma_e$, cross-sections (a) and gain cross-section, $\sigma_g$, for different inversion rates $\beta$ (b) of Ho:YAG ceramics.

The $^5I_7$ fluorescence lifetime of 8 ms measured for 1 at. % bulk Ho:YAG ceramics at room temperature is very close to the radiative lifetime $\tau_r$ and also in good agreement with values reported for single crystals (7.8 ms [3, 34]).

### 2.2.2 CALGO and CALYO

CALGO ($CaGdAlO_4$) as well as its isomorph CALYO ($CaYAlO_4$) (space group $I4/mmm$ or $D_{4h}^{17}$, point group $4/mmm$) are representatives of an isostructural family of crystals belonging to the tetragonal crystal system, with the general formula $ABCO_4$, where A is either Ca or Sr, B is Y or Ln, and C is Al or Ga; A and B statistically occupy the same 9-fold $O^{2-}$-coordinated site with tetragonal $4mm$ local symmetry whereas C is in octahedral sites. They are optically uniaxial disordered crystals. In CALGO, the $Tm^{3+}$ ions (ionic radius: 1.052 Å) replace the $Gd^{3+}$ ones which have a closer radius (1.107 Å) compared to the $Ca^{2+}$ ions (1.180 Å) [38]. The local disorder affecting the crystal field for $Tm^{3+}$ originates from the second coordination sphere of the $Ca^{2+}/Gd^{3+}$ ions due to the charge difference of these two ions and the different cation-cation distances [42]. CALGO and CALYO crystals were one of the most successful hosts with $Yb^{3+}$-doping in terms of shortest pulse durations (~ 30 fs) achieved by mode-locked lasers around 1 µm [43, 44]. This is due to the relatively broad and flat gain spectra related to the structural disorder. Nevertheless, CALGO exhibits relatively good thermo-mechanical properties, and the thermal conductivity of 4.5-5.3 W/mK (depending on the orientation), is roughly two times lower compared to the garnets [45]. Another advantage is the low melting temperature: CALGO melts congruently at ~ 1840°C (i.e., no phase transition

to a different crystallographic structure occurs below this temperature) and large crystals were obtained by the Czochralski (Cz) method [46].

The Tm:CALGO crystals grown by the Cz method at FEE GmbH (Idar-Oberstein, Germany) were with 3 at. % Tm-doping in the charge [47]. The actual concentration was unknown but one can assume a segregation coefficient (i.e. ratio of the actual doping in the crystal to that in the melt) of ~ 0.6 from the literature [29]. This leads to 1.8 at. % doping in the crystal which, with a density of 5.947 g·cm$^{-3}$ [45], gives $N_{Tm}$ = 2.22×10$^{20}$ cm$^{-3}$, in good agreement with absorption measurements. The as-grown crystals were yellow colored as shown in Fig. 2.9a. According to [45] the coloration is due to interstitial oxygen. The color centers were removed by annealing under $H_2$ at 950°C for 24 h. The annealed crystals became completely colorless, cf. Fig. 2.9b. With an *a*-cut cubic (3×3×3 mm$^3$) sample, it was possible to access both π- and σ-polarizations for spectroscopy and laser experiments. Here, the spectroscopic features of Tm:CALGO are presented.

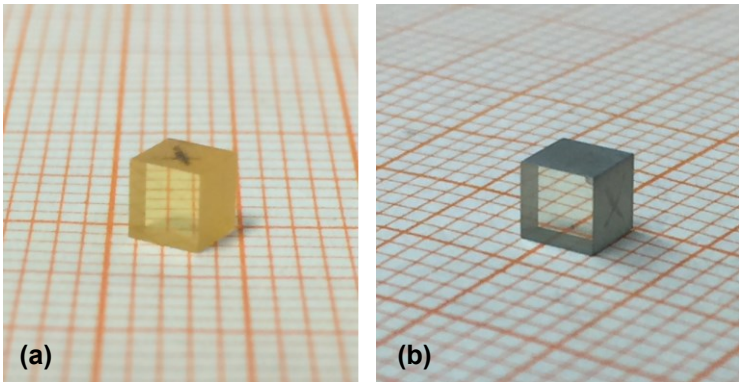


Fig. 2.9 As grown (yellow) (a) and annealed (colorless) (b) Tm:CALGO crystals.

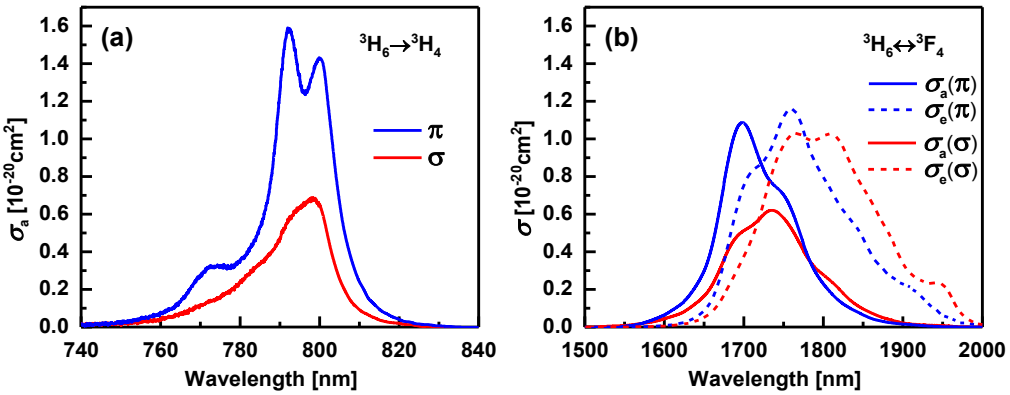


Fig. 2.10 Polarized absorption cross-sections for the $^3H_6 \rightarrow {}^3H_4$ (a) and absorption/stimulated emission (solid/dashed line) cross-sections for the $^3H_6 \leftrightarrow {}^3F_4$ (b) transitions of Tm:CALGO.

Figures 2.10 show the absorption cross-sections for the pump transition measured in Tm:CALGO, and the absorption, emission and gain cross-sections obtained for the laser transition at room temperature, respectively [47]. For the $^3H_6 \rightarrow {}^3H_4$ transition suitable for

pumping near 800 nm, the maximum $\sigma_a$ is $15.9\times10^{-21}$ $cm^2$ at 792.0 nm (π-polarization), with a linewidth of 16.5 nm, see Fig. 2.10a. For σ-polarization, $\sigma_a$ is lower, $6.9\times10^{-21}$ $cm^2$ at 798.4 nm, with a linewidth of 18.1 nm. For the $^3H_6 \rightarrow {}^3F_4$ transition, cf. Fig. 2.10b, $\sigma_a(\pi) = 10.9\times10^{-21}$ $cm^2$ at 1.698 µm and $\sigma_a(\sigma) = 6.2\times10^{-21}$ $cm^2$ at 1.7352 µm.

The radiative lifetime $\tau_r$ of the $^3F_4$ excited state is ~ 2 ms as calculated from Judd-Ofelt theory [47]. Using this lifetime in the modified reciprocity method, the stimulated-emission cross-sections for the $^3F_4 \rightarrow {}^3H_6$ transition were calculated, see dashed line in Fig. 2.10b. The maximum $\sigma_e$ corresponds to π-polarization: $11.6\times10^{-21}$ $cm^2$ at 1.7592 µm, with a linewidth of 143.6 nm. For σ-polarization, there exist two identical maxima of $10.3\times10^{-21}$ $cm^2$ at 1.766 and 1.808 µm, see dashed line in Fig. 2.10b.

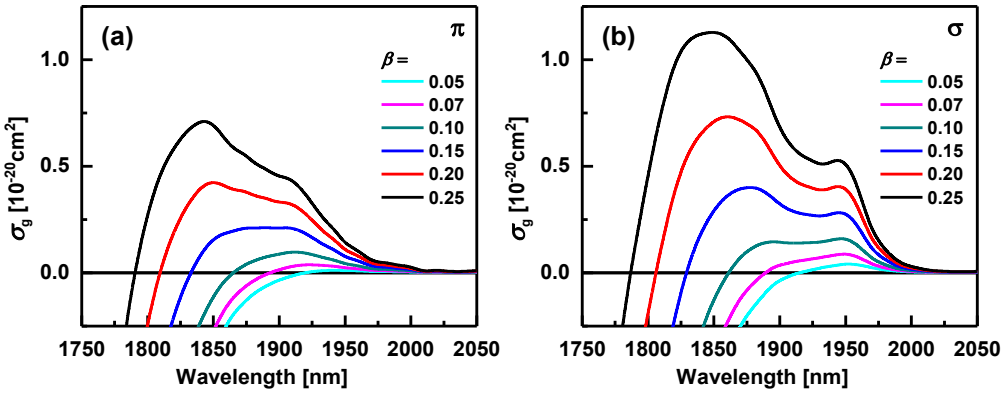


Fig. 2.11 Gain cross-sections $\sigma_g$ for π- (a) and σ- (b) polarizations corresponding to the $^3F_4 \rightarrow {}^3H_6$ transition of Tm:CALGO for various inversion rates $\beta$.

However, at longer wavelengths, where laser operation in the quasi-3-level $Tm^{3+}$ laser system is expected, the σ-polarization exhibits higher emission cross-section: The value of $\sigma_e$ in the local maximum at 1.944 µm is $2.38\times10^{-21}$ $cm^2$. The calculated gain cross-sections shown in Fig. 2.11 indicate generally higher gain for σ-polarization which will be naturally selected in a laser cavity without polarization n selective elements. At low inversion rates ($\beta <$ 0.10), typical for mode-locked lasers, the gain for σ-polarization is also broader and smoother, which may facilitate the generation of shorter pulses. The wavelength dependence of the gain cross-sections of Tm:CALGO is smoother and relatively flat compared to the garnet hosts discussed before. The $^3F_4$ fluorescence lifetime of 6.04 ms measured in [29] for 3.66 at. % bulk Tm:CALGO at room temperature is longer than the calculated radiative lifetime $\tau_r$ which is attributed to re-absorption.

Only Tm:CALGO was available for the present work. As can be expected from the closer ionic radii (1.075 Å for $Y^{3+}$), the isomorph CALYO shows higher segregation coefficient for Tm-doping [48]. The spectroscopic information on Tm:CALYO that can be found in the literature is rather limited, especially the polarization dependence, but at least the absorption spectra for the pump transition are very similar to Tm:CALGO [48].

### 2.2.3 KLuW and MgW

Ordered monoclinic double tungstates and disordered tetragonal double tungstates and molybdates represent other important classes of laser host crystals [25]. In particular, monoclinic potassium double tungstates with general formula $KRE(WO_4)_2$ (KREW, RE = Gd, Y, Lu) with which some of the most efficient lasers with different Ln-dopings have been realized, are famous for their strong anisotropy, highest cross-sections, and minimal fluorescence quenching due to relatively large dopant ion-ion separation. Tm:KREW crystals, and Tm:KLuW in particular which so far provided the best results in terms of shortest pulses, are characterized by broad and smooth spectral emission near 2 μm [49] which makes them attractive for mode-locked lasers. In this ordered crystal, $Tm^{3+}$ ions substitute $Lu^{3+}$ ions in an 8-fold coordinated site with monoclinic 2 local symmetry. For reasons similar to those discussed when comparing LuAG to YAG, KLuW is the preferable host of this class for Tm dopant ions. The tungstate crystal investigated for the first time in the present work as Tm host, $MgWO_4$ (MgW) belongs to a group of monoclinic divalent metal mono-tungstates with general formula $MWO_4$ (M = Mg, Mn, Ni, Cd, Zn) [50, 51], which do not contain a passive RE ion and for which Ln-doping has been attempted only very recently. The spectroscopic features of the novel Tm:MgW crystal developed at Fujian Institute of Research on the Structure of Matter, CAS (Fuzhou, China), show emission properties similar to those of the monoclinic double tungstates [52]. In the ordered MgW host, $Tm^{3+}$ ions substitute $Mg^{2+}$ ions in a single 6-fold coordinated site with monoclinic 2 local symmetry while charge compensation is ensured by $Na^+$ ions from the flux. The distortion of the crystal field for the $Tm^{3+}$ ion is facilitated by the significant difference of its ionic radius (0.88 Å) from that of the substituted $Mg^{2+}$ ion (0.72 Å) [38]. As a consequence, Tm:MgW exhibits very broad absorption and emission bands [52]. With 10 at. % Tm in the charge, the concentration of $Tm^{3+}$ ions in the as-grown crystal was determined to be 0.89 at. % ($N_{Tm} = 1.409\times10^{20}cm^{-3}$), leading to an expectedly low segregation coefficient of 0.089 [52]. The room temperature thermal conductivity of the monoclinic MgW host crystal measured for an arbitrary orientation is ~ 8.7 W/mK [53], i.e. more than 2 times higher compared to KLuW (2.55-4.4 W/mK, depending on direction) [49].

Both KLuW (space group $C2/c$ or $C_{2h}^6$, point group $2/m$) and MgW (space group $P2/c$ or $C_{2h}^4$, point group $2/m$) belong to the monoclinic system and are optically biaxial. Figure 2.12 shows the correspondence between crystallographic and dielectric frames in KLuW and MgW crystals. In KLuW, the monoclinic angle is β = 130.7°, the principal optical axis $N_p$ is parallel to the *b* crystallographic axis, $N_g$ is located at 18.5° with respect to the *c* crystallographic axis and $N_m$ at 59.2° with respect to the *a* crystallographic axis, cf. Fig. 12a [49].

Since the principal refractive indices of MgW are still unknown and only an average value can be found in the literature, it was not possible to define the $N_p$, $N_m$, and $N_g$ axes. Conoscopic interference patterns (characteristic pictures observed on a screen for divergent light propagating along special directions in a biaxial crystal) still enable one to identify the location of the three orthogonal principal axes *X*, *Y* and *Z*, choosing arbitrarily the *Y*-axis to be parallel to the crystallographic *b*-axis, cf. Fig. 2.12b. The other two axes of the optical

indicatrix are located in the *a*-*c* plane: *X* at 36.4° from *a* and *Z* at 37.1° from *c*. The monoclinic angle is β = 90.7°. Note that for MgW the non-standard convention $a_0 < c_0$ for the lattice constants is used and the specified angles refer in fact to Yb-doped MgW [54].

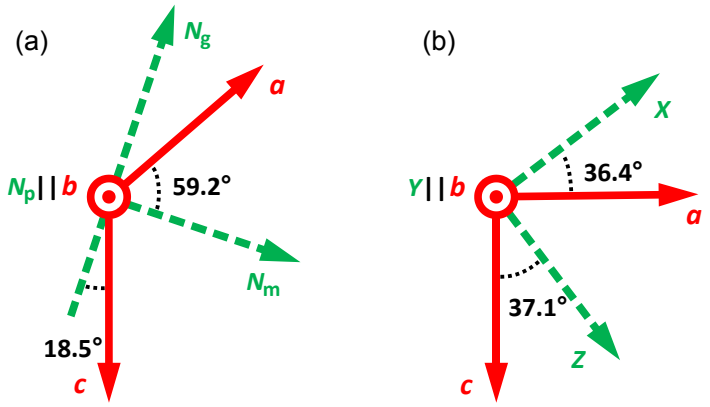


Fig. 2.12 Correspondence between crystallographic (red) and dielectric (green) frames in KLuW (a) and MgW (b).

Similar to KLuW, MgW exhibits non-congruent melting character (i.e. a phase transition to a different crystallographic structure below the melting point) and cannot be grown by the Cz method [55]. The growth temperature can be reduced by adding a solvent (flux methods) and in this case the top-seeded solution-growth method (TSSG) is applied. Fig. 2.13 shows a bulk Tm:MgW crystal with dimensions of ~ 16×8×6 $mm^3$ [52]. The light yellowish coloration of the as-grown crystal comes from color centers (defects), most probably related to the flux used. The defect related optical absorption in the 320–420 nm spectral range is present also in undoped MgW [55].

Fig. 2.13 As-grown MgW crystal with 0.89 at. % Tm-doping.

The spectroscopic features of Tm:KLuW have been discussed in detail in [49]. For comparison and completeness, only the wavelength dependence of the cross-sections is

reproduced in Figs. 2.14-15. Note that due to the low cross-sections, the $N_g$ polarization is not used for pumping and / or lasing. The radiative lifetime $\tau_r$ of the $^3F_4$ excited state of 1.483 ms calculated by Judd-Ofelt theory agrees, within the accuracy, with the measured by the pinhole method fluorescence lifetime $\tau_f$ of 1.34 ms for 3.7 at. % Tm-doping [49].

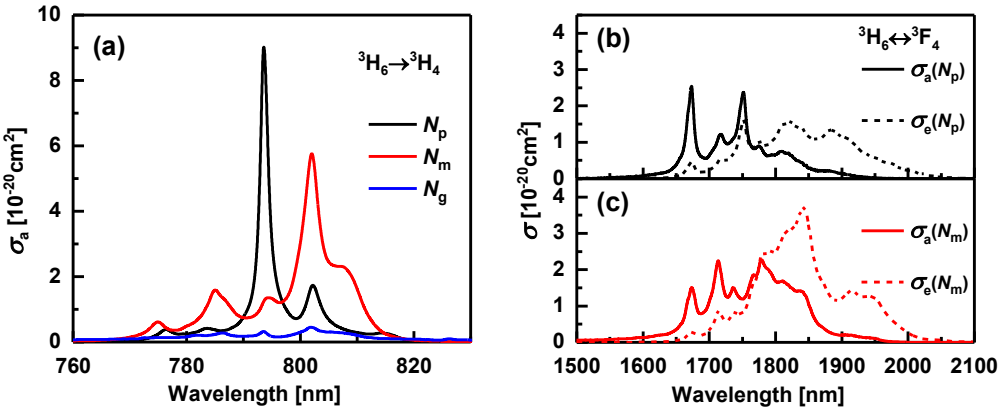


Fig. 2.14 Polarized absorption cross-sections for the $^3H_6 \rightarrow {}^3H_4$ transition of Tm:KLuW (a), and absorption and stimulated-emission cross-sections for the $^3H_6 \leftrightarrow {}^3F_4$ transition: $N_p$- (b) and $N_m$- (c) polarizations (reproduced from [34]).

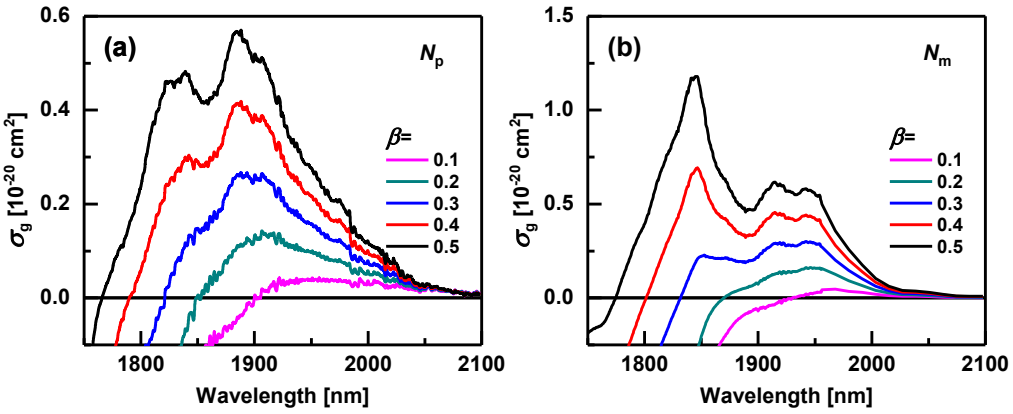


Fig. 2.15 Gain cross-sections of Tm:KLuW for $N_p$- (a) and $N_m$- (b) polarizations and different inversion rates $\beta$ (reproduced from [34]).

Figures 2.16 and 2.17 summarize the spectroscopic properties of Tm:MgW in the dielectric frame defined in Fig. 12b [52]. The polarized absorption cross-sections $\sigma_a$ for the $^3H_6 \rightarrow {}^3H_4$ Tm transition are shown in Fig. 2.16a. The maximum $\sigma_a$ is $2.07\times10^{-20}$ cm$^2$ at 803.0 nm ($X$-polarization) with a linewidth of ~ 14 nm. For $Y$-polarization, the maximum $\sigma_a$ is somewhat lower and amounts to $1.44\times10^{-20}$ cm$^2$ at 796.4 nm, with a flat top and a linewidth of 31 nm, and for $Z$-polarization the maximum $\sigma_a$ is only $0.35\times10^{-20}$ cm$^2$ at 802.0 nm with a linewidth of 25 nm. Strong anisotropy is seen also in the absorption cross-section for the $^3H_6 \rightarrow {}^3F_4$ transition, cf. Fig. 2.16b. Thus, similar to KLuW, one of the polarizations ($Z$) in the case of the MgW host turns out not to be useful for pumping/lasing.

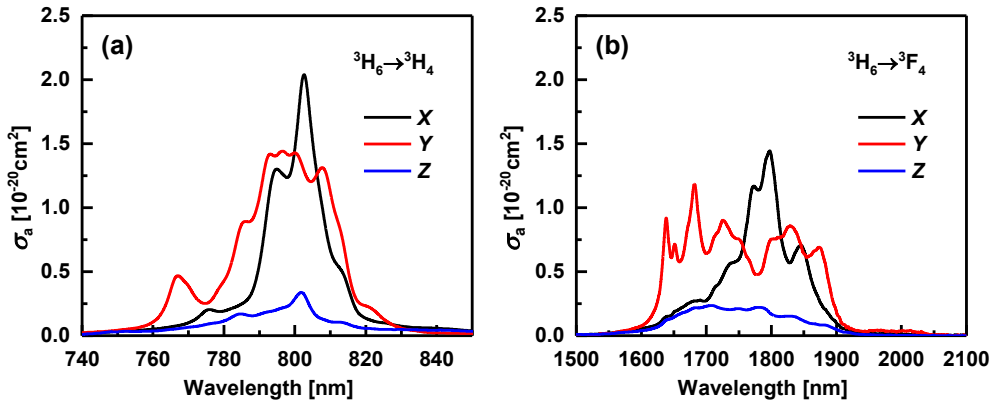


Fig. 2.16 Polarized absorption cross-sections for the $^3H_6 \rightarrow ^3H_4$ (a) and $^3H_6 \rightarrow ^3F_4$ (b) transitions of Tm:MgW.

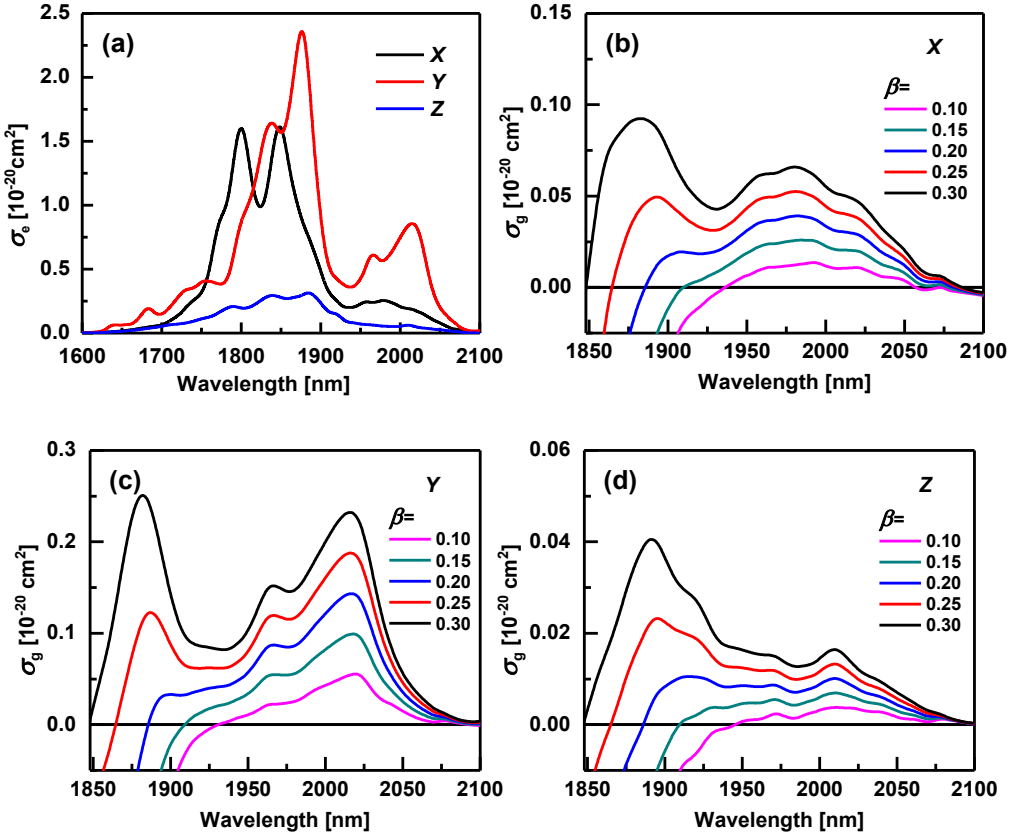


Fig. 2.17 Polarized stimulated-emission cross-sections for the $^3F_4 \rightarrow ^3H_6$ transition of Tm:MgW (a), and gain cross-sections for different inversion rates $\beta$ for *X*- (b), *Y*- (c) and *Z*- (d) polarizations.

The radiative lifetime $\tau_r$ of the $^3F_4$ excited state amounts to 1.95 ms, as calculated from Judd-Ofelt theory [52]. The polarized stimulated-emission cross-sections for the $^3F_4 \rightarrow ^3H_6$ transition were calculated from the absorption cross-sections by the modified reciprocity method using this lifetime and are shown in Fig. 2.17a. The maximum $\sigma_e$ corresponds to *Y*-polarization and amounts to $2.36 \times 10^{-20}$ cm$^2$ at 1.877 μm with a linewidth of 76.7 nm. For *X*-

polarization, there exist two local peaks at 1.7995 and 1.8485 μm with a cross-section of ~ $1.61\times10^{-20}$ cm$^2$. For *Z*-polarization, the maximum $\sigma_e$ is only $0.31\times10^{-20}$ cm$^2$ at 1.884 μm.

With the same argumentation as for Tm:CALGO, due to the quasi-3-level scheme, the actual free running laser polarization is expected to be parallel to the *Y*-axis. The local maximum for $\sigma_e^Y$ amounts to $0.86\times10^{-20}$ cm$^2$ at 2.0145 μm, with a linewidth of 83 nm. More accurate predictions including the situation in lasers with selected polarization are provided by the calculated gain cross-sections shown in Figs. 2.17b-d. For inversion rates $\beta$ up to 0.25, the maximum gain cross-section for *Y*-polarization is at ~ 2.014 μm (cf. Fig. 2.11 for Tm:CALGO where switching to shorter wavelengths occurs at much lower inversion). Comparing with the gain curves for Tm:KLuW shown in Fig. 2.15, it can be seen that Tm:MgW naturally supports operation above 2 μm which is essential to avoid air absorption/dispersion effects. The tungstates in general, similar to Tm:CALGO exhibit smoother gain cross-sections compared to Tm- or Ho-doped garnets.

The $^3F_4$ fluorescence lifetime of 1.93 ms measured in [36] by the powder method for 0.89 at. % Tm:MgW at room temperature almost coincides with the calculated radiative lifetime $\tau_r$

## 2.3 Comparison of the Tm- and Ho-doped laser materials

The main spectroscopic features of the presented laser active materials and the thermal conductivity $\kappa$ (taken from the literature) are summarized in Table 2.3. For the monoclinic tungstates, only the two useful polarizations are included: $N_m$ and $N_p$ for Tm:KLuW, and *X* and *Y* for Tm:MgW. For the garnets, the spectroscopic parameters refer to single crystals, for better comparison and also because for the moment these data are more reliable.

Table 2.3 Relevant properties of the considered 2 μm laser materials: $\lambda_P$ indicates the pump wavelength for which $\sigma_a$ is specified together with the linewidth (FWHM) and similarly $\lambda_L$ indicates the expected laser wavelength with the corresponding $\sigma_e$ and linewidth (FWHM).

| Material | Tm:YAG | Tm:LuAG | Tm:CALGO | | Tm:KLuW | | Tm:MgW | | Ho:YAG |
|---|---|---|---|---|---|---|---|---|---|
| Symmetry | cubic | cubic | tetragonal | | monoclinic | | monoclinic | | Cubic |
| Polarization | – | – | σ | π | $N_m$ | $N_p$ | *X* | *Y* | – |
| $\lambda_P$ [nm] | 785 | 788 | 798.4 | 792 | 802 | 793.5 | 803 | 797 | 1908 |
| $\sigma_a$ [$10^{-21}$ cm$^2$] | 7.5 | 5.7 | 6.9 | 15.9 | 59.5 | 99.6 | 20.7 | 14.4 | 11.8 |
| FWHM [nm] | 1.3 | 1.7 | 18.1 | 16.5 | 4 | 1 | 14 | 31 | 5 |
| $\lambda_L$ [μm] | 2.013 | 2.023 | 1.95 | 1.95 | 1.95 | 1.95 | 1.979 | 2.0145 | 2.09 |
| $\sigma_e$ [$10^{-21}$ cm$^2$] | 1.8 | 1.66 | 2.38 | 0.84 | 12 | 5.7 | 2.55 | 8.6 | 12.9 |
| FWHM [nm] | 28 | 23 | – | – | – | – | – | 83 | 15.5 |
| $\tau_f$ [ms] | 10-10.5 | 10.9 | 6.04 [46] | | 1.34 [49] | | 1.93 [52] | | 7.8 |
| $\kappa$ [W/mK] | 8.8-13 [56] (undoped) | 8.3-9.6 [56] (undoped) | 5.3//*a*, 4.5//*c* [45] (undoped) | | 2.55-4.4 [49] (undoped) | | 8.69 (avg.) [53] ($Cr^{3+}$-doped) | | 8.8-13 [56] (undoped) |
| Growth method | Cz / Ceramics | Cz / Ceramics | Cz / Ceramics | | TSSG | | TSSG | | Cz / Ceramics |

Apart from KLuW which was included for completeness and also for comparison of the experimental results in Chapter 4, the other materials in Table 2.3 are those used in the laser experiments. Availability of spectroscopic data is a prerequisite for the design of successful

lasing experiments and the interpretation of the results. However, even for the most widely used crystals, this information is never complete and steadily updated and improved. This is a consequence of the difficulties already mentioned in this chapter, e.g. not precisely known actual doping, limited dynamic range of spectrophotometers used to measure the absorption, systematic errors in the measured fluorescence lifetime, etc. The absorption cross-sections (position of peaks and their magnitude in dependence on polarization) were used to design the active elements for the laser experiments in terms of doping level, length and orientation for use with the available pump sources. The characteristic absorption linewidths in Table 2.3 are important to evaluate the required wavelength stability and emission linewidth of the pump source and conclude whether diode-pumping is feasible. Calculated low-signal absorption values were used to evaluate possible saturation effects under lasing conditions.

The emission wavelengths in Table 2.3 are used to compare with the experimentally observed laser wavelength in the free-running mode and also in relation with the dependence on the cavity losses. As already discussed, the laser wavelength will in fact be determined by the gain cross-sections and from the observed wavelength one can judge about the actual cavity losses. While linewidths could be partially defined for the emission spectra, this was impossible for the gain spectra. This is related to all the line broadening mechanisms such as electron-phonon coupling, crystal disorder, distortion of the crystal field, etc. That such data could not be included in the table makes the comparison of different materials more qualitative but on the other hand, as already mentioned, broader and smoother gain spectra are the first prerequisite for obtaining ulrashort pulses. If the broader gain occurs for a given polarization in combination with a higher gain cross section the choice of the crystal orientation is rather simple (secondary effects such as thermo-mechanical properties still might have to be considered). Otherwise one normally has to compare the laser results for more than one orientation simply because the gain cross sections depend on the inversion level and hence on cavity losses, etc. This is a consequence of the quasi-3-level system according to which the 2 μm lasers operate.

From the spectroscopic information presented in this chapter one can more or less compare the potential of the different materials in Table 2.13. This has been largely discussed when presenting them individually. The fluorescence lifetime is more related to the expected difficulties in achieving and stabilizing ultrashort pulse operation of the laser. As it will be explained in Chapter 4, although there is no direct relation of this parameter to the stability criterion, from the Füchtbauer-Ladenburg equation shorter lifetime is associated with higher emission cross-sections which favor the mode-locking stability.

Other parameters related to the thermo-optic properties are also important but similar to the spectroscopic properties they are only partially known (in particular their anisotropy, temperature and wavelength dependence). The thermal conductivity in Table 2.3 is only one such example. Power scaling of such lasers might require taking account also the tensor character of the thermal expansion or the thermo-optic coefficients (dependence of refractive index on temperature). For the power levels applied in the present work, simple water cooling of the active element holder proved to be sufficient to avoid thermal effects.

Further aspects when comparing different crystals which are difficult to assess quantitatively include crystal homogeneity, stress, optical damage threshold, difficulty of the growth, etc. These aspects were not relevant for the present work because relatively small samples were employed. Nevertheless, it shall be outlined here that almost all samples available were exclusive, often from first growth attempts of novel materials, made available only for the present laser experiments.

# Chapter 3
# Saturable absorbers

After the gain medium, the saturable absorber is the second most essential cavity element which plays a crucial role in generating femtosecond pulses from a SSL. Passive mode-locking of SSLs is realized by an intensity or fluence dependent loss mechanism in the laser cavity which favors the peak of the circulating pulse and suppresses its wings, in particular the leading edge, providing a pulse shortening effect which, as will be explained in the next chapter, is counterbalanced in the steady-state regime by dispersion. Most often this role is played by saturable absorbers (SAs) representing a key element in ultrafast SSLs. Much shorter laser pulses can be obtained from passively mode-locked SSLs because driven by the pulse itself, this key element can modulate the cavity losses much faster than any electronic (typically acousto- or electro-optic) modulator used in actively mode-locked lasers (cf. Chapter 4). From the first application of saturable dyes for mode-locking [57] until now, various types of SAs have been developed to satisfy the different laser requirements because depending on the parameters of the SA and the gain medium, saturable absorption may also lead to passive Q-switching or Q-switched mode-locking (cf. Chapter 4). While organic dye SAs played a crucial role in the first steady-state femtosecond lasers which were based on laser dyes [4], in ultrafast SSLs this role was taken over by semiconductor SAs [58, 59]. In the last decade, however, novel low-dimensional carbon nanostructures with parameters similar to those of the semiconductor SAs proved to be useful for Q-switching and mode-locking of SSLs. In the first place these were carbon nanotubes (CNTs) and graphene which operate in a wide spectral range covering almost the entire near-IR [60-62]. Despite the different absorption mechanism, there are several general material independent SA parameters which control the pulse generation process: non-saturable losses, saturable losses, saturation fluence or intensity and recovery time.

In this chapter the principle of operation of relevant SAs will be reviewed based on the existing literature, including their saturation and relaxation behavior, and the parameters of semiconductor, single-walled CNT (SWCNT) and graphene SAs will be compared at ~ 2 μm.

## 3.1 Characteristics of SAs used in mode-locked SSLs

As already mentioned an element with saturable loss is needed for passive mode-locking. In the so-called Kerr lens mode-locked SSLs this is indeed an intensity dependent saturable loss which can be achieved as a result of self-focusing (SF) in combination with a soft or hard aperture [59]. The physical effect behind this, as it will be explained in Chapter 4, is the electronic Kerr effect which can be considered as being instantaneous or much faster compared to the steady-state pulse duration. In contrast, in the considered types of SAs that are employed in the present work absorption rather than loss is saturated and they show non-

instantaneous response (slow SAs) to laser radiation. Therefore, the saturation effect is mostly fluence and not intensity dependent, with the saturation fluence as a characteristic parameter. However, the same SA can be considered as being fast in a mode-locked SSL generating relatively long picosecond pulses and then the saturation intensity will be the relevant parameter.

Although this is not desirable, only part of the cavity losses introduced by the SA are saturable. This part of the losses is often called modulation depth of the SA (in analogy with this parameter in active mode-locking devices) although the actual effect on the circulating pulse depends on the saturation level and can be lower than the specified modulation depth. The non-saturable part of the absorption losses, due e.g. to defect centers, is unwanted and may eventually prevent mode-locking. After some recovery time, the SA returns to its initial state and different relaxation mechanisms may be responsible for more than one characteristic time constant of this recovery process.

In principle all considered types of SAs can operate in reflection when combined with a dielectric or metallic mirror or in transmission when manufactured on a transparent substrate. In the following, a reflection type SA will be considered: Its reflectivity $R$ is a function of the incident pulse fluence $F_p$ and thus a function of time during the interaction with the circulating pulse. Typically SEmiconductor SAs are Mirrors (SESAMs) while SWCNTs and graphene are used as transmission type SAs. In the latter case, instead of the reflectivity $R$ one considers the fluence/intensity dependent transmission $T$ of the SA.

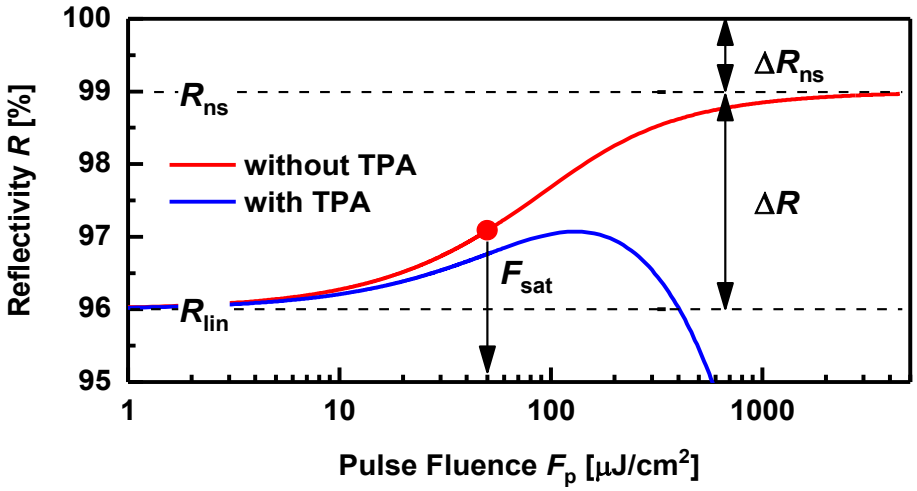


Fig. 3.1 Typical reflectivity curve of a reflection type SA: nonlinear reflectivity $R$ as a function of incident pulse fluence $F_p$. $R_{ns}$ and $R_{lin}$ define the reflectivity with the absorption saturated and the linear (i.e. low signal) reflectivity, respectively.

The nonlinear reflectivity $R$ versus incident pulse fluence $F_p$ is shown in Fig. 3.1. Such a dependence can be experimentally measured outside the cavity [63]. This is easier for transmission type SAs where translation along a focused beam ($z$-scan) at constant power can be applied [64]. A deviation from the model function may occur at higher fluences with the reflectivity decreasing due to two-photon absorption (TPA) [63], an effect more typical for

transmission-type SAs, due e.g. to the substrate material. At relatively low fluences, the nonlinear reflectivity $R$ can be described by a 2-level system band structure approximation, neglecting intraband relaxations as well as trapping or recombination. Then one can solve the coupled nonlinear differential equations for the absorption and the transmitted intensity [63]. After integration over time one obtains:

$$R(F_\mathrm{p}) = R_\mathrm{ns}\frac{\ln\left(1 + R_\mathrm{lin}/R_\mathrm{ns}(\mathrm{e}^{F_\mathrm{p}/F_\mathrm{sat}} - 1)\right)}{F_\mathrm{p}/F_\mathrm{sat}},$$

As expected for a 2-level system with a slow relaxation, the saturation effect is fluence dependent [4]. At higher fluences this formula can be corrected by the factor $\exp(-F_p/F_2)$ [63], where $F_2 \approx \tau_p/\beta_{TPA}L_{eff}$, $\tau_\mathrm{p}$ is the pulse duration, $\beta_\mathrm{TPA}$ is the TPA coefficient, $L_\mathrm{eff}$ is the effective absorber thickness which accounts for the standing wave pattern, the penetration depth of the optical field into the mirror, and the different TPA coefficients for different materials. TPA involves a transition from the ground state of a system to a higher-lying state by the simultaneous absorption of two incident photons and is an instantaneous, i.e. intensity-dependent process [65] as can be seen by substitution of the $F_2$ expression into the saturation term which leads to $\exp(-\beta_{TPA}I_pL_{eff})$ dependence with the pulse intensity $I_\mathrm{p} = F_\mathrm{p}/\tau_\mathrm{p}$. The differential equation describing this effect reads $dI_p/dz = -\alpha I_P - \beta_{TPA}I_p^2$ where $\alpha$ is the linear absorption coefficient (as derived from the Lambert–Beer law). The blue curve in Fig. 3.1 shows the modified nonlinear reflectivity in the presence of TPA assuming $F_2 = 150$ μJ/cm$^2$. Apart from the introduced losses, TPA obviously counteracts the pulse shortening mechanism due to saturation because it is an instantaneous intensity dependent effect that suppresses the pulse peak.

Typically, i.e. in the absence of TPA, only three parameters completely describe the characteristic curve of the SA shown in Fig. 3.1: the linear reflectivity $R_\mathrm{lin}$, the reflectivity $R_\mathrm{ns}$ with the absorption totally bleached and the saturation fluence $F_\mathrm{sat}$. The modulation depth $\Delta R$ and the non-saturable losses $\Delta R_\mathrm{ns}$ are expressed then as $\Delta R = R_\mathrm{ns} - R_\mathrm{lin}$ and $\Delta R_\mathrm{ns} = 1 - R_\mathrm{ns}$, respectively. The saturation fluence $F_\mathrm{sat}$ corresponds to the value of the incident fluence at which the reflectivity $R$ increases by $\Delta R$/e (i.e. by ~ 37% of $\Delta R$) from $R_\mathrm{lin}$, where the saturation process starts. Note that all the above definitions imply plane waves, i.e. the spatial distribution of the beam on the SA is neglected assuming some average values.

The recovery time of the SA can be measured with standard pump-probe techniques. Despite the complexity of the dynamics, typical temporal decay of the reflectivity (or transmission) of SAs from a certain saturated level back to the initial, i.e. the linear level can be modeled with a bi-exponential function

$$R(t) = Ae^{-\mathrm{t}/\tau_1} + (1 - \mathrm{A})e^{-t/\tau_2},$$

where $A$ is the amplitude of the fast component, $\tau_1$ is the fast decay constant and $\tau_2$ is the slow decay constant.

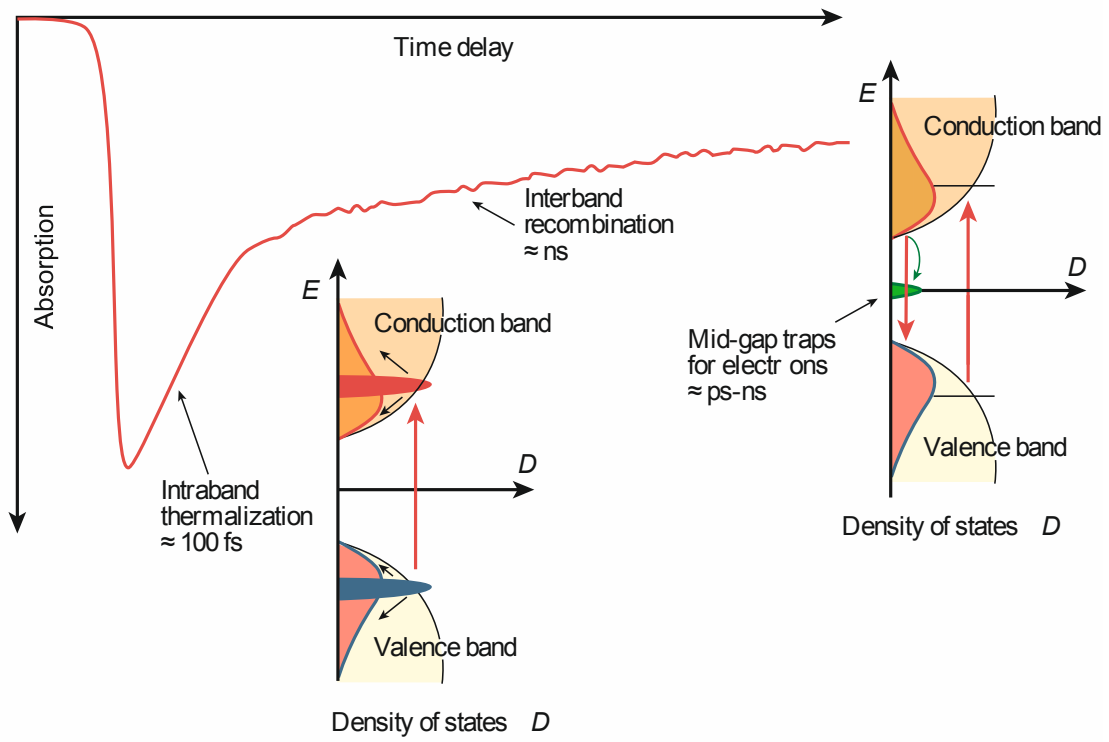


Fig. 3.2 Typical relaxation dynamics of a SESAM: bi-exponential response with a fast component $\tau_1$ in the 100 fs range corresponding to intraband thermalization and a slow component $\tau_2$ in the picosecond-nanosecond range corresponding to interband recombination (figure reproduced from [1]).

The two decay constants correspond to different recombination processes as shown in Fig. 3.2 [1] for a SESAM. A semiconductor can absorb light if the photon energy is sufficient to excite carriers from the valence to the conduction band (graphene is an exception since it is a zero band-gap semiconductor). Then, after a decoherence process, the relaxation is dominated solely by the dynamics of the electron/hole population. The scattering that occurs between charge carriers is known as intraband thermalization. Usually this process takes place within ~ 100 fs. Once the thermalization is completed, interband recombination of electron – hole pairs will dominate the relaxation process until the semiconductor returns to thermodynamic equilibrium. For high quality semiconductors (i.e. with a low level of defect states), such recombination processes take place on time scales of hundreds of ps and longer [1]. At high optical intensities, electrons can accumulate in the conduction band, so that initial states for the absorbing transition are depleted while final states are occupied. Band-filling occurs because two electrons cannot fill the same state in agreement with the Pauli blocking principle. This is the physical mechanism behind the saturation (bleaching) of the absorption.

The terms fast and slow refer to the pulse duration. If the steady-state pulse duration of a CW pumped laser is longer than the relaxation time of the SA, the saturable absorption will be fast, i.e. intensity dependent with a characteristic saturation intensity parameter $I_{sat} \sim F_{sat}/\tau_2$.

Saturation of the SA by intensity may lead to its damage and in mode-locked SSLs such a regime is more typical for artificial SAs (in which losses and not absorption are saturated) such as Kerr lensing in combination with an aperture. On the other hand, the use of a slow SA does not mean that the resulting steady-state pulse duration of the mode-locked SSL cannot be shorter than the characteristic decay constants: In fact the slow component might be instrumental for achieving reliable self-starting. The same types of SAs can be used not only for mode-locking where the pulse duration is much shorter than the cavity round trip time but also for Q-switching of SSLs where the pulse duration is much longer than the cavity round trip time (cf. Chapter 4), however, the requirements are different. In mode-locked SSLs, $\Delta R_{ns}$ is typically quite low (e.g. < 1%) and $F_{sat}$ shall be several times lower than the pulse fluence which can be adjusted by the beam size on the SA. Depending on the mode-locking mechanism employed, the recovery time may or may not be important for the generation of ultrashort pulses. Low $\Delta R_{ns}$ helps to achieve higher average power and shorter pulse durations. Optical damage is a more serious issue in SAs used for Q-switching because of the higher fluences. Thus, it is essential to avoid Q-switching instabilities in mode-locked SSLs, e.g. by enhancing the bleaching through tighter focusing on the SA. This and other issues related to the dependence of the mode-locking regime on the SA parameters will be discussed in Chapter 4.

## 3.2 SESAMs

SEmiconductor SA Mirrors (SESAMs) are the most widely used SAs developed for passively mode-locked SSLs. Until their invention such passive mode-locking was possible only in a pulsed (non-steady-state) regime employing fast dye SAs and a steady-state regime under CW pumping was considered to be impossible to realize because of instabilities [4]. The general design of a SESAM is characterized by two main components: the semiconductor quantum wells (QWs) and the Bragg mirror. III-V semiconductor materials offer a wide flexibility in the absorption range to match the emission wavelength of a particular SSL. Despite the band structure and the presence of mid-gap impurities, the long wavelength limit of the saturable absorption is only determined by the band-gap. Thus, the absorption of different III-V semiconductor materials ranges from ~ 400 nm in the UV (GaN-based structures) to ~ 2.5 μm in the near-IR (InGaAsSb-based structures). However, a broad spectral range for a selected material composition may only be obtained at the expense of higher defect concentration because this is achievable at an increased lattice mismatch to a given substrate material. Also, TPA may be non-negligible in SESAMs [66].

Different from the typical GaAs-based design for operation around 1 μm, SESAMs for lasers emitting around 2 μm are based on InGaAs or InGaAsSb QWs. In the latter case, GaSb substrates and AlAsSb/GaSb distributed Bragg reflectors can be applied to avoid large lattice mismatch, improve the SESAM quality and reduce the non-saturable losses. Fig. 3.3 shows such a typical GaSb-based design.

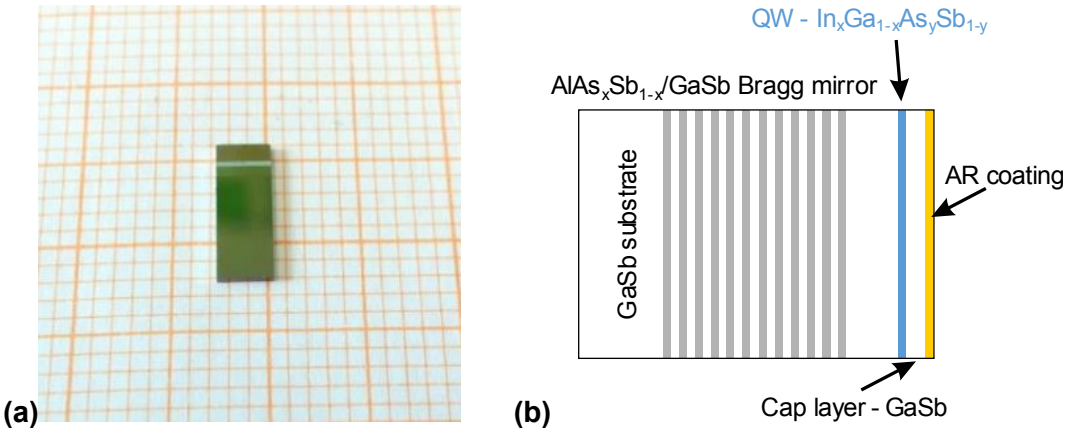


Fig. 3.3 AR-coated near-surface quantum-well (QW) design GaSb-based SESAM (a) and its schematic structure (b).

Interband recombination processes taking place on a time scale of hundreds of picoseconds or even nanoseconds will restrict the performance of such a SESAM with respect to the achievable pulse duration. Few methods have been developed to accelerate the recombination processes, such as low temperature growth [67] and ion implantation [68]. However, most of these techniques increase the defect density and thus the non-saturable losses imposing a trade-off between faster recovery time and lower $\Delta R_{ns}$ of the SESAM design. A near-surface QW design is another method to accelerate the recovery of the saturable absorption by placing the QWs only a few nm from the surface (separated by a cap layer, as shown in Fig. 3.3), see Table 3.1 and Fig. 3.4. This is due to fast surface recombination effects. In fact, the recovery time of such high quality heterostructures did not change for a relatively large variation of the growth conditions [69] which is attributed to the fact that in narrow band-gap materials, such as GaSb, the Auger recombination (recombination of electron-hole pair giving up their energy to an electron in the conduction band, increasing its energy) is significantly stronger than in GaAs and InP heterostructures, which also contributes to the reduced carrier lifetime. The band gap of GaSb is 0.726 eV and though not observed for the intensities applied so far, TPA can be expected with ultrashort pulses in the 2 μm spectral range.

Because the initially developed semiconductor SAs introduced large cavity losses, they were first used in weakly coupled secondary cavities (e.g., such coupled through a low-transmission output coupler of the main cavity) [70]. This simultaneously resolved the problem of the too low saturation intensity and the low damage threshold. The antiresonant Fabry–Pérot SA (A-FPSA) design combines these properties in an integrated structure that can be employed directly in the cavity, most often as an end reflector [71]. In earlier A-FPSA designs, the SA was placed between two Bragg mirrors. Adjusting the thickness of the SA and spacer layers, the Fabry-Perot is operated at antiresonance at the laser wavelength so that the intensity inside is always lower than the incident intensity, which increases the effective saturation intensity and the damage threshold of the device. The dielectric top reflector can be designed to control the intensity in the SA. The A-FPSA exhibits negligible bandwidth

limitations at antiresonance because the free spectral range is very broad and the semiconductor bottom Bragg reflector or the dielectric top reflector may be the limiting factor. Modern SESAMs are based on a complex design, which may incorporate also special dispersive properties. Concerning the Fabry-Perot effect it ranges from the high-finesse A-FPSA (high reflectivity of the top reflector) version to AR-coated SESAMs where the top reflectivity is missing. In the latter case thinner SA layers have to be used to suppress the effect of non-saturable losses while the saturation performance can be controlled by the beam waist on the SESAM surface [72]. In addition, the AR-coating can increase the modulation depth of the SESAM and act as a passivation layer for the semiconductor surface that can improve the long-term reliability of the entire device [58].

The GaSb-based SESAMs employed in the present work were AR-coated (Table 3.1 and Fig. 3.4). Precise simulations performed by the manufacturers in the case of the near-surface design indicate that the electric field strength in the position of the QWs is twice lower with AR-coating compared to the case without, cf. Fig. 3.5. Measurements indicated, however, that the AR-coating reduces the slow decay constant $\tau_2$ by as much as 68% [73] which is a desirable effect (although no data are available about the effect on the actual modulation depth).

Table 3.1 AR-coated GaSb-SESAMs with different designs tested in the present work (from [73]).

| SESAM | No. of QWs | Cap [nm] | $\tau_1$ [ps] | $\tau_2$ [ps] |
|---|---|---|---|---|
| No.1 | 3 | 300 | 0.292 | 9.7 |
| No.2 | 2 | 5 | 0.266 | 4.1 |
| No.3 | 1 | 10 | 0.300 | 1.7 |
| No.4 | 1 | 5 | 0.471 | 1.6 |
| No.5 | 2 | 50 | 0.239 | 20 |

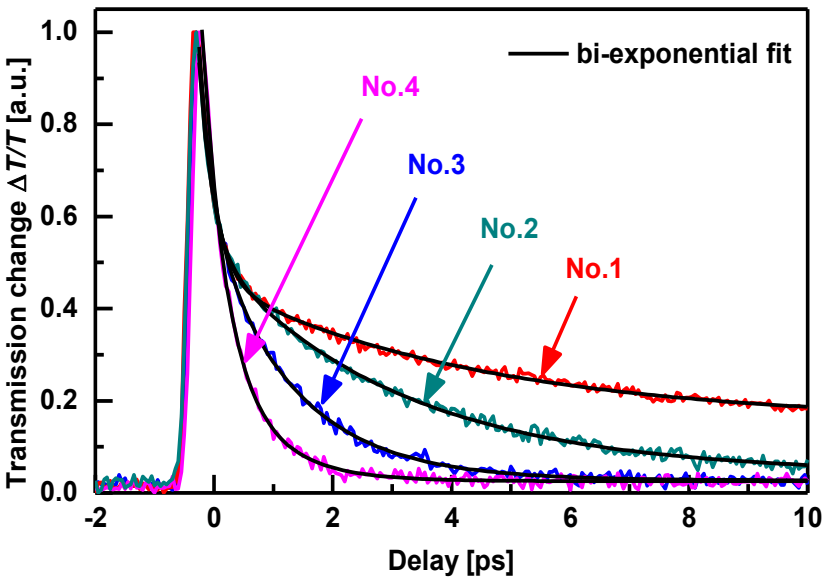


Fig. 3.4 Relaxation dynamics of different GaSb-based SESAMs from Table 3.1 (from [73]).

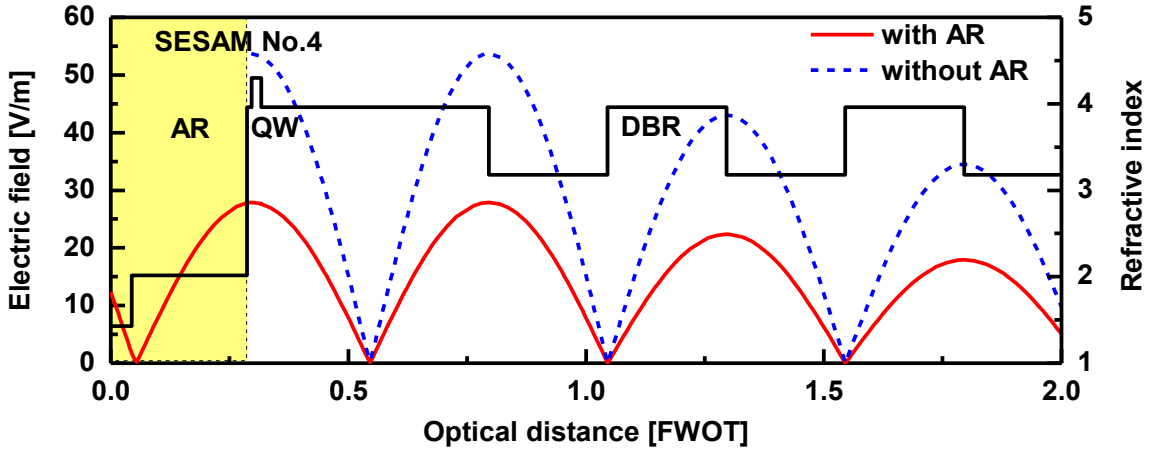


Fig. 3.5 Simulation of the electric field in SESAM No.4 with and without AR-coating: With a near-surface QW design the field drops almost 2 times in the presence of AR-coating. The FWOT (full wave optical thickness) units correspond to the design wavelength (2 µm). The size of the QW is exaggerated for better visibility. DBR: distributed Bragg reflector.

For low optical intensities, the degree of electronic excitation is small, and the absorption remains unsaturated. At high optical intensities, however, electrons can accumulate in the conduction band, so that initial states for the absorbing transition are depleted while final states are occupied (Pauli blocking).

SESAMs require complex and expensive fabrication processes such as metal organic chemical vapor deposition (MOCVD), metal organic phase vapor epitaxy (MOPVE), or molecular beam epitaxy (MBE), From the above description it is also clear that the complex stack of layers including AR-coating, cap layer, QWs, distributed Bragg reflector and substrate required for a specific SESAM may lead to a dramatic number of parameters to be optimized in different growth runs. This increases not only the fabrication complexity but also the costs.

## 3.3 SAs based on carbon nanostructures

As already mentioned, SWCNTs and graphene also show saturable absorption properties which are suitable for mode-locking [60, 74]. Compared to SESAMs, the fabrication of SWCNT- and graphene-SAs is much simpler: Commercially available SWCNTs or graphene can be easily transferred (i.e. by spin coating) onto a dielectric mirror or a transparent substrate.

SWCNTs and graphene represent 1D and 2D carbon nanostructures, respectively. As illustrated in Fig. 3.6, monolayer graphene may be regarded as a source material from which different dimensions of carbon nanostructures can be constructed [75]. Although the growth of SWCNTs does not require graphene as a key precursor [76], for visualization, SWCNTs may be understood as a rolled up sheet of graphene with diameter on the nanometer scale and length on the micrometer scale.

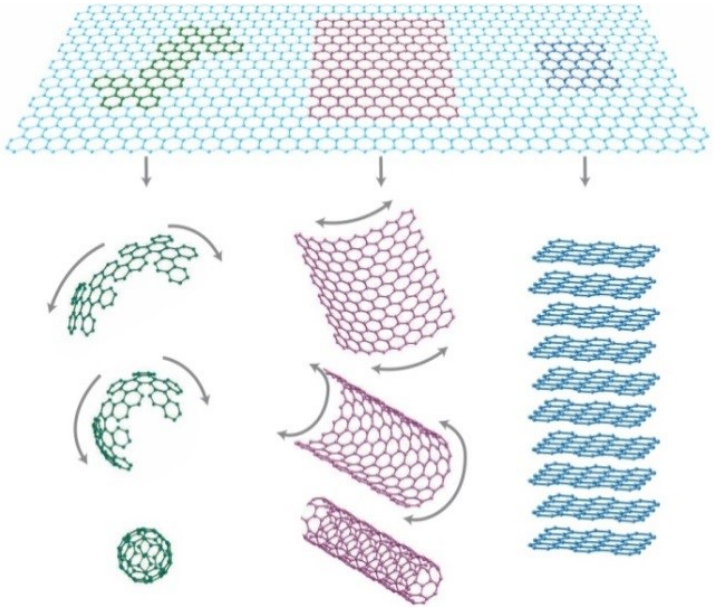

Fig. 3.6 Construction of fullerenes, SWCNTs, and graphite (from left to right) from graphene, which may be understood as a basis structure for the three carbon nanostructures (from [75]).

### 3.3.1 SWCNT-SAs

Depending on their chirality (roll-up direction), SWCNTs exhibit pronounced metal or semiconductor characteristics. In particular, the latter possess a pronounced optical nonlinearity together with chemical stability and high optical damage threshold [77]. Figure 3.7 shows the qualitative pattern of sharp van Hove peaks, which arise from quasi–onedimensionality, predicted for electronic state densities of semiconducting SWNTs [78].

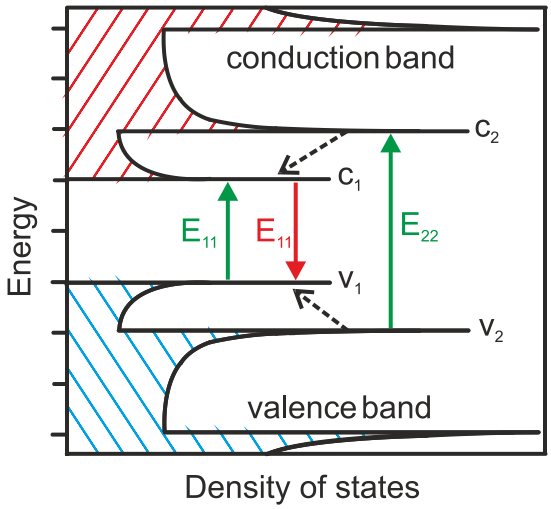


Fig. 3.7 Schematic density of electronic states for an individual free-standing SWCNT showing the first two interband transitions. Solid arrows depict optical absorption and emission transitions; dashed arrows denote non-radiative relaxation of the electron (in the conduction band) and hole (in the valence band) before emission (after [78]).

As the absorption resonance of the electronic interband transition spectrally shifts with diameter and chirality [79], natural mixtures of SWCNTs automatically provide smooth and broad absorption in the near-IR range. A typical transmission spectrum of a SWCNT-SA as the one shown in Fig. 3.8a [80] exhibits two broad absorption bands spanning from 0.85 to 1.15 μm and from 1.60 to 2.10 μm. The latter is attributed to an overlap of the first interband transition (E11) in semiconducting SWCNTs (Fig. 3.7) of different diameters and chiralities with intertube interaction causing further broadening. Raman spectroscopy provides information on the diameter and chirality of the distributed SWCNTs. The former band is related to the E22 interband transition in semiconducting SWCNTs (Fig. 3.7). The two absorption bands represent averaging and their position depends on the synthesis method for the SWCNTs which affects their distribution [81]. Using different types of SWCNTs and based on these two transitions such SAs can be employed for mode-locking of various TM and Ln lasers emitting in the near-IR [81] and in particular of Tm/Ho lasers, operating in the 2 μm spectral range. A particular advantage of SWCNTs is that a dispersion of different types can be used to manufacture a single device applicable in all near-IR SSLs [60, 81].

Under excitation, charge carriers in SWCNTs are excited from the valence to the conduction band by absorbing a photon. With increasing fluence the number of occupied states increases, preventing absorption of subsequent incident photons. This leads to a characteristic decrease of the absorption with the incident intensity, similar to semiconductors.

Regardless of the fabrication procedure used, non-saturable losses are always present in SWCNTs, in the first place related to scattering. Depending on the preparation of the SWCNT dispersion and the coating process, more or less pronounced bundling and curling may occur, causing nanotubes to interweave, eventually forming macroscopic ball-like objects with much less favorable scattering properties. However, bundling may also enhance tube-to-tube interactions to some extent, accelerating the absorber relaxation [60]. In any case, control of the statistical distribution of the SWCNTs is the key to balancing non-saturable losses and accelerated relaxation. Separating low values of saturable and non-saturable losses is experimentally difficult and such data are not available in the entire near-IR spectral range.

The SWCNT SAs studied in this work were fabricated by the procedure described in [78]. Purified SWCNTs synthesized by the arc-discharge method from a commercial supplier were used as a precursor. They were dried under vacuum at 100°C and dispersed in dichlorobenzene (DCB) via ultrasonic agitation. Subsequently, poly(m-phenylenevinylene-co-2,5-dioctoxy-p-phenylenevinylene) (PmPV) was added in the ultrasonic process to enhance their solubility. The SWCNT dispersion and a polymethyl-methacrylate (PMMA) solution were then mixed and stirred. Transmission type SAs were produced by spin coating the SWCNT film onto a quartz substrate (substrate thickness 1 mm, film thickness ~ 300 nm) [77]. Assuming a modulation depth < 0.5% as deduced at 1.3 μm [80], the non-saturable losses of such SWCNT-SAs near 2 μm are estimated to be in the 0.7 - 1.2% range.

Figure 3.8b shows the measured relaxation dynamics of such a SWCNT-SA pumped and probed at 1.92 μm [80]. With the bi-exponential decay model described before, the response is well fitted by one nearly instantaneous component with a time constant of ~ 0.25 ps and a

second slower component with a characteristic time of 1.16 ps, which is comparable to the fastest response reported for GaSb-based SESAMs.

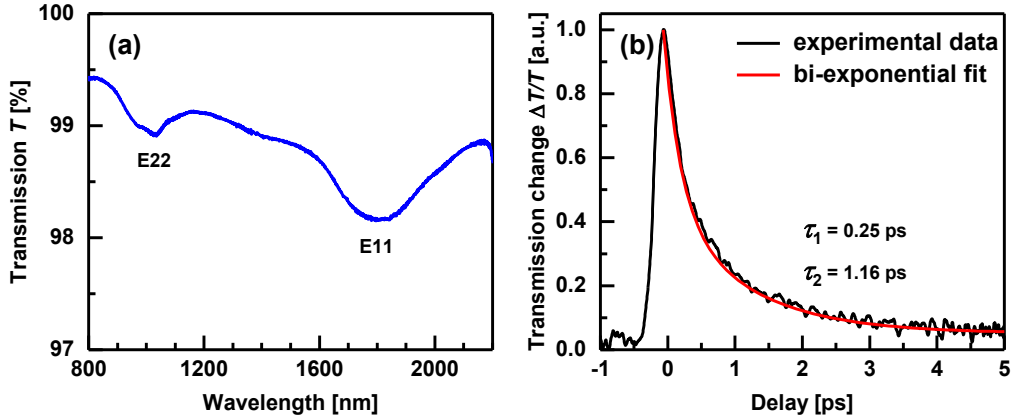


Fig. 3.8 (a) Low signal transmission spectrum of a transmission-type SWCNT-SA (corrected for Fresnel losses) and (b) relaxation dynamics of such a SWCNT-SA at 1.92 µm (from [80]).

TPA has been observed in SWCNTs at shorter wavelengths near 800 nm for peak intensity values on the GW/cm$^2$ level [82]. However, no such observations have been reported at longer wavelengths for similar intensity levels [60].

### 3.3.2 Graphene-SAs

While the saturable absorption of SWCNTs decreases significantly beyond 2 µm, vanishing towards 2.1 µm [80], graphene is characterized by a broad absorption extending into the mid-IR [74]. Furthermore, the modulation depth of graphene-SAs can be increased by adding graphene layers [74]. A single-layer graphene is characterized by "universal" small-signal absorption, almost constant from the visible (~ 0.6 µm) up to at least ~ 3 µm, equal to $\pi\alpha$ = 2.3% where $\alpha = e^2/4\pi\varepsilon_0\hbar c \sim 1/137$ is the fine structure constant [83]. For multilayer (n) graphene, the small-signal absorption scales with n almost linearly, ~ nπα. The mechanism of saturable absorption is illustrated in Fig. 3.9. Graphene has a unique band structure. Both its valence and conduction bands have hollow cone shapes touching each other which results in almost zero band-gap. The absorption of a photon with an energy $hv$ leads to the appearance of a hole in the valence and an electron in the conduction band. For high excitation intensities, the concentration of photon-generated carriers increases significantly, so that the states near the edges of the bands (within an energy interval of $hv/2$ for each band) are filled [74, 84]. Thus, further absorption is blocked implying transparency of graphene.

The linear absorption of graphene is almost constant but the saturable part shows pronounced wavelength dependence [85]. In particular, $I_{sat}$ decreases with wavelength and it is easier to achieve saturation of graphene at longer wavelengths. Figure 3.9 illustrates this dependence: The number of electronic states is linearly proportional to the energy and lower energy photons require the excitation of a lower number of electrons in order to exhaust the corresponding part of the valence band and bleach the absorption. Indeed, measurements indicate that $I_{sat}$ decreases in the ~ 0.5-2 µm spectral

range inversely proportional to the wavelength, approaching zero at long wavelengths, which is the characteristic of the Dirac point in the graphene band structure. Thus, the use of graphene as a SA for mode-locking ~ 2 µm Tm/Ho lasers is more attractive compared to lasers emitting e.g. at ~ 1 µm.

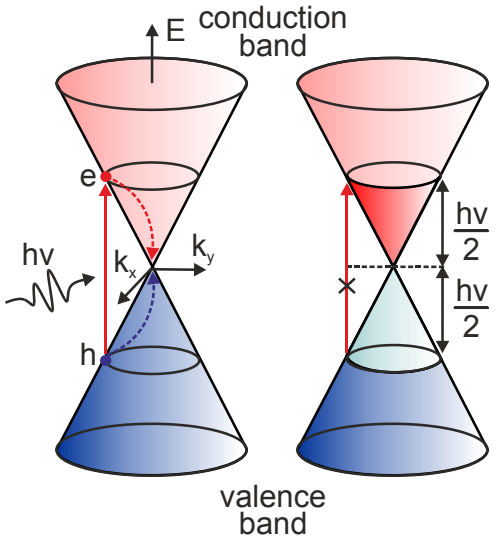


Fig. 3.9 The saturable absorption effect in graphene.

The graphene-SAs employed in the present work were fabricated following the procedure described in [86]. Monolayer graphene was synthesized by chemical vapor deposition (CVD) of the mixture of methane and hydrogen gases on Cu foils at 1000°C. After spin-coating the well-grown graphene monolayer with 5 wt % PMMA in chlorobenzene, the underlying Cu foil was etched and the graphene layer supported by PMMA was transferred onto quartz or $CaF_2$ substrates without any intense mechanical and chemical treatments and dried on a hot plate at 80°C. Finally, acetone was used to remove the PMMA layer. Multilayer SAs were fabricated by layer-by-layer stacking of monolayer graphene.

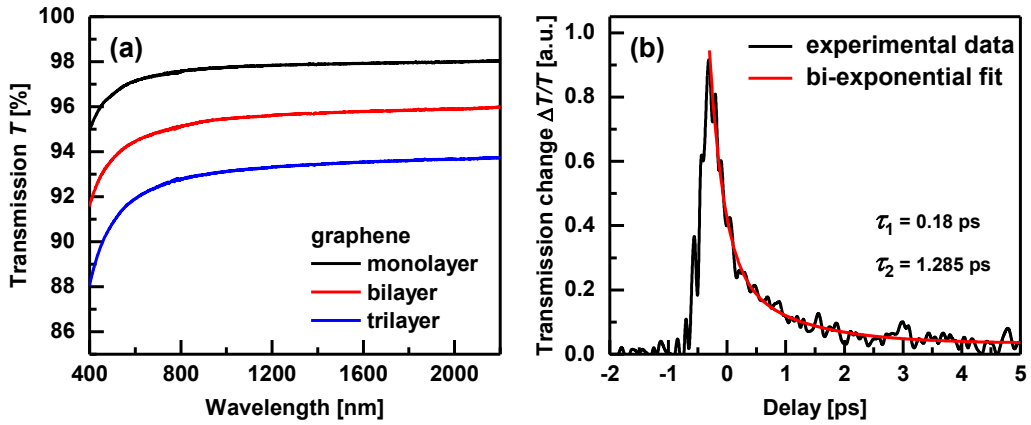


Fig. 3.10 (a) Transmission spectra of monolayer, bilayer and trilayer graphene-SAs (corrected for Fresnel losses) (from [86]) and (b) relaxation dynamics of a graphene-SA at 1.56 µm (from [62]).

The transmission spectra of such monolayer, bilayer and trilayer graphene-SAs are shown in Fig. 3.10a [86]. The increase in absorption indeed occurs in steps of 2.3%. Assuming a modulation depth similar to the values measured at 1.25 µm (0.54% and 1.3% for monolayer and bilayer graphene, respectively [86]), the non-saturable losses near 2 µm were calculated as 1.86% for monolayer and 3.4% for bilayer graphene, slightly higher compared to the SWCNT-SAs but lower compared to the SESAMs.

Figure 3.10b shows the measured relaxation dynamics of a graphene-SA at 1.56 µm [62]. Applying the bi-exponential decay model, the response is well described by a fast component with a time constant of 0.18 ps and a slower component with a decay time of ~ 1.29 ps.

Due to resonant enhancement, the TPA coefficient $\beta_{\mathrm{TPA}}$ of graphene shows also strong wavelength dependence and can be few orders of magnitude higher compared to normal semiconductors [87]. However, the relevant thickness $L_{\mathrm{eff}}$ amounts to only few nm (one atomic layer), which is $>10^6$ times thinner compared with a typical SESAM design, and no detrimental TPA effects are expected in graphene-SAs.

## 3.4 Comparison of different SAs employed for mode-locking at 2 µm

The relevant characteristics of the SAs employed for mode-locking of Tm/Ho lasers near 2 µm are summarized in Table 3.2. In general, both carbon nanostructures are characterized by a fast carrier relaxation process, low saturation fluence, low cost as well as easy fabrication.

Table 3.2 Relevant properties of different SAs for the 2 µm spectral range.

| | GaSb-based SESAMs | SWCNTs | Mono/bilayer Graphene |
|---|---|---|---|
| Operating wavelength [µm] | 1.9-3 [73] | 0.8-2.1 [80] | 0.8-2.5 [74] |
| Modulation depth $\Delta R$ [%] | ≈ 3-6 [88]* | < 0.50% [80] | 0.54 / 1.30 [86] |
| Non-saturable losses $\Delta R_{\mathrm{ns}}$ [%] | | ≈ 0.7-1.2 [80] | 1.86 / 3.4 [86] |
| Saturation fluence $F_{\mathrm{sat}}$ [µJ/cm$^2$] | NA | < 10 [80] | 14.5 / 22.5 [86] |
| Fast relaxation time $\tau_1$ [ps] | 0.3-0.5 [73] | 0.25 [80] | ≈ 0.18 [62] |
| Slow relaxation time $\tau_2$ [ps] | ≈ 2-10 [73] | 1.16 [80] | 1.29 [62] |
| TPA | not observed | absent | absent |
| Fabrication | complex/expensive | simple | simple |

*in the case of the SESAMs only the total losses are known and included in the table.

As can be concluded from the Table 3.2, the characteristics of the SAs described are often difficult to be measured extracavity (e.g. in pump and probe arrangements) and not all of them are precisely known. This is related mainly to the low values of the modulation depth. However, in most of the cases the signal-to-noise ratio is sufficient to evaluate the relaxation times. As will be seen in Chapter 5, the short relaxation times play a crucial role in achieving pulse shortening in mode-locked 2-µm lasers.

# Chapter 4
# Fundamentals of passive mode-locking

The gain media and SAs employed in the present work were reviewed in the previous two chapters. Inserting such a SA into the cavity of a CW laser containing the gain medium might result in two different regimes of operation: passive Q-switching and mode-locking. It is important to distinguish them here because although the thesis is devoted solely to mode-locking, the Q-switching process might simultaneously occur, leading to the so-called regime of Q-switched mode-locking (QSML). This regime is essentially different from the steady-state mode-locking which can be called CW mode-locking (CWML).

In a passively Q-switched laser, the absorption of the SA will prevent the build-up of oscillation, continuously increasing the population inversion of the gain medium over some period in which the cavity quality Q-factor is low (high losses). At a certain point, the SA losses suddenly start to decrease due to the rapidly growing amplified spontaneous emission (ASE). The cavity begins to resonate the radiation and its Q-factor grows rapidly (low loss cavity) while the laser produces finally a so-called "giant pulse" at its output. After the giant pulse has been generated, the cavity Q-factor again switches to low because the gain has been depleted and the SA has recovered. Under CW pumping the process can be periodic and typically the pulse durations are much longer (in the 1-100 ns range) than the cavity round trip time. Highest energies (at the mJ level) can be generated if lasing is suppressed for a period equal to the gain medium lifetime, i.e. at repetition rates corresponding to the inverse lifetime.

Mode-locking is a totally different process: A Fabry-Perot cavity is resonant for an infinite number of longitudinal modes with frequency separation of $c/2L_c$ where $L_c$ is the optical cavity length and a CW laser normally oscillates on many longitudinal modes (optical frequencies) which fall within the gain bandwidth. The electric field of the different longitudinal modes inside the cavity can be expressed as [4]:

$$E_m(t) = E_0 \cos\left(\omega_0 t + m\frac{\pi c}{L}t + \varphi_m\right),$$

where $\omega_0$ is the center frequency and $\varphi_m$ is the phase of the m-th longitudinal mode. If the phase $\varphi_m$ of the different modes are locked with a constant $\theta_0$, $\varphi_m = \varphi_0 + \mathrm{m}\theta_0$ , the sum of such 2n+1 modes can be expressed as,

$$\begin{aligned} E(\mathrm{t}) = \sum_{m=-n}^{n} E_m(t) &= E_0 \sum_{m=-n}^{n} \cos(\omega_0 t + m\frac{\pi c}{L}t + \varphi_0 + m\theta_0) \\ &= E_0 \frac{\sin\frac{2n+1}{2}(\frac{\pi c}{L}t + \theta_0)}{\sin\frac{1}{2}(\frac{\pi c}{L}t + \theta_0)} \cos(\omega_0 t + \varphi_0). \end{aligned}$$

The last expression can be regarded as a plane wave with a carrier frequency $\omega_0$ and an amplitude modulated by the factor $\sin\frac{2n+1}{2}\left(\frac{\pi c}{L}t+\theta_0\right)/\sin\frac{1}{2}(\frac{\pi c}{L}t+\theta_0)$. The formation of a pulse by the superposition of longitudinal modes is illustrated in Fig. 4.1 which shows the temporal intensity and the spectral intensity of the pulse (known in physics also as a wave package).

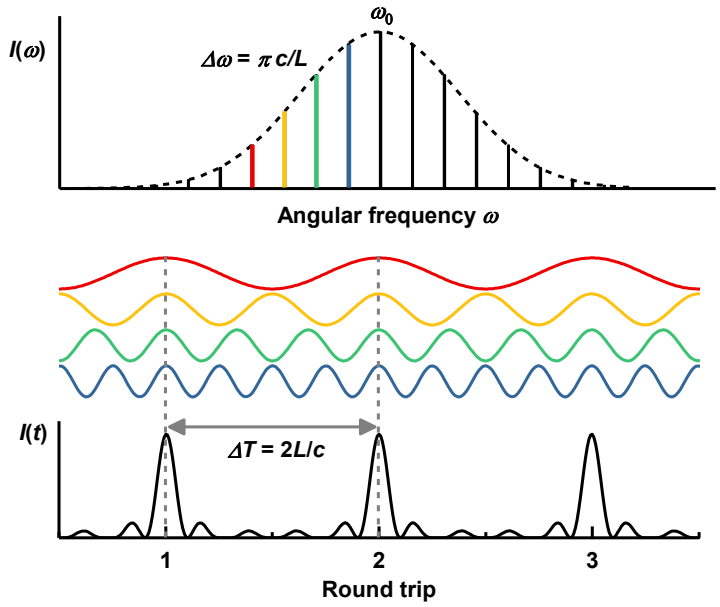


Fig. 4.1 Superposition of longitudinal modes, an effect known as mode-beating in the case of few modes, gives birth to well-defined pulses at a separation of $2L/c$ in the case of a large number of longitudinal modes ($n$ = 1 assumed for the refractive index).

If a fixed phase relationship can be established between these different longitudinal modes, ultrashort pulses are formed through the superposition of these frequencies whose pulse duration (in the picosecond and femtosecond ranges) is much shorter than the cavity round trip time. As in Q-switching, this can be realized externally (active modulation) or by the pulse itself (passively). In the steady-state which can be established under CW pumping, mode-locking could be understood as a single pulse, oscillating inside the cavity and "bleaching" (saturating) the SA each time when passing through it, while random fluctuations are suppressed by the SA. This eventually produces a pulse train at the output, with a repetition frequency $f_{rep} = c/2L_c$. Obviously a SA with a relaxation time much longer than the cavity roundtrip will only lead to Q-switching. It is essential to realize that the spectrum of a mode-locked laser consists of the discrete modes which, however, are normally not resolved by the spectrometer which records the envelope.

While active mode-locking which relies on an optical modulator typically produces longer (~ 100 ps) pulses and needs electronic synchronization between the cavity length and the modulation frequency, passive mode-locking of bulk SSLs is capable of producing pulses as short as few femtoseconds. Nowadays, numerous cavity elements and techniques have

been demonstrated but the operation principle of all of them can be reduced to a saturable loss effect and in particular to saturable absorption (cf. Chapter 3). The already mentioned Kerr lens mode-locking (KLM) is the most prominent example of a situation without absorption and the main advantage of this technique is that there is no heat load leading to damage. The other most exploited technique relies on a SA used in reflection or transmission. Both effects can be present simultaneously: the SA serving as a starting and stabilizing mechanism and the Kerr effect shortening the pulse duration.

In this chapter, the basic concepts and theories of passive mode-locking are briefly reviewed. The role of the dispersion and the methods for dispersion compensation are explained in detail, as well as self-phase modulation (SPM). Then a model of passive mode-locking is introduced leading to the so-called Haus master equation for the steady-state pulse solution. The three main passive mode-locking mechanisms are presented followed by the related soliton type solutions to the equation and their properties. Finally, the stability of CWML against Q-switched operation and pulse break-up is discussed.

## 4.1 Pulse shaping effects

All cavity elements are associated with a respective pulse shaping effect, i.e. a modification of the pulse intensity and/or phase. One such effect is the saturable absorption considered in the previous chapter and related to the SA. The active medium discussed in Chapter 2 also is important for the formation of the steady-state pulse. However, in Ln SSLs (both bulk and fiber) there is no appreciable saturation of the laser gain by interaction with a single pulse because of the relatively low emission cross-sections leading to high saturation energies and negligible gain depletion. The gain medium lifetime in $Ln^{3+}$-doped materials is much longer than the cavity round-trip time and saturation still takes place in terms of average intracavity intensity which only reduces the low signal gain compared to the situation without lasing but there is no change in the instantaneous gain during the interaction with a single pulse. However, the spectral extent of the gain can play the role of a spectral filter (similar to the SA, the cavity mirrors, etc.) which affects the steady-state regime. The cavity losses, both useful such as the output coupler (OC) and unwanted losses, also play a role in the formation of the steady-state and its characteristics. The spectral limiting (filter) effect is mainly due to the OC because it is most difficult to be manufactured broadband. In the following the focus will be on two pulse shaping effects of crucial importance in femtosecond SSLs: dispersion and SPM.

### 4.1.1 Dispersion

The origin of dispersion in dielectric media is the frequency-dependence of the linear part of the dielectric susceptibility $\chi^{(1)}(\omega)$ whose real part is related to the refractive index $n(\omega)$. Considering a linearly polarized optical pulse traveling through a transparent isotropic medium with length $L$, different frequency components will experience time delay with respect to each other. The frequency-dependent phase shift can be expressed as

$$\phi(\omega) = k(\omega)L\,,$$

where

$$k(\omega) = \frac{n(\omega)}{c}\,\omega$$

is the wave number. For anisotropic media, the refractive index corresponding to the laser polarization has to be considered. The phase shift can be expanded as a Taylor series around the center frequency $\omega_0$,

$$\phi(\omega) = \phi(\omega_0) + \frac{\partial\phi}{\partial\omega}(\omega-\omega_0) + \frac{1}{2!}\frac{\partial^2\phi}{\partial\omega^2}(\omega-\omega_0)^2 + \frac{1}{3!}\frac{\partial^3\phi}{\partial\omega^3}(\omega-\omega_0)^3 + \cdots.$$

The 0[th]-order term represents a constant phase shift. The 1[st] order derivative term $\partial\phi/\partial\omega$ will introduce a linear phase shift for different frequencies and is called group delay (GD) because it is related to the group velocity of the pulse in the medium. The pulse envelope and phase propagate with different velocities. The GD describes the delay of the pulse as compared to a pulse with a flat phase (i.e. for vanishing dispersion).

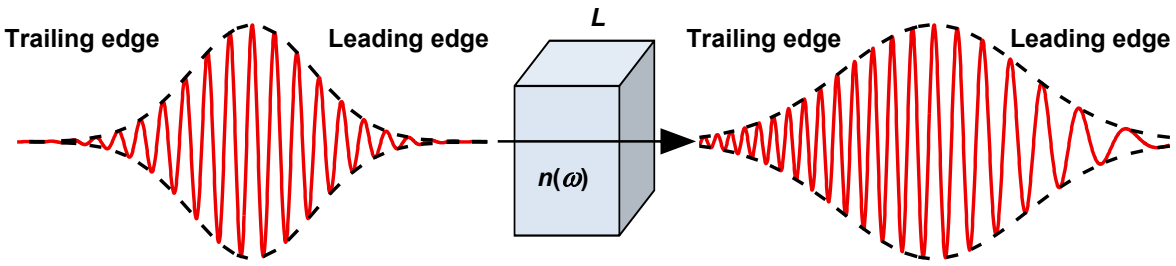


Fig. 4.2 Pulse broadening and chirping upon propagation in a medium with positive GDD.

The 2[nd] order derivative term $\partial^2\phi/\partial\omega^2$ is called group-delay dispersion (GDD). It indicates a linear frequency dependence of the GD for different frequency components: e.g., for positive GDD higher frequency components will be delayed with respect to lower frequency components as shown in Fig. 4.2. This defines a positive or up-chirp (frequency modulation) of the pulse which is simultaneously temporally broadened behind the medium.

The 3[rd] order term $\partial^3\phi/\partial\omega^3$ representing the Third Order Dispersion (TOD) introduces a frequency dependence of the GDD leading to a more complex distortion of the pulse shape.

These dispersion terms can be defined and quantified per unit length, e.g. the GD per unit length corresponds to the reverse of the group velocity $v_g$. From the Sellmeier equations which describe the wavelength dependence of the refractive index of a transparent material, one can calculate all the dispersion terms. Table 4.1 summarizes the relations between the two definitions and the defining equations in terms of wavelength and refractive index.

Table 4.1 Relation between dispersion and dispersion per unit length.

| Term | Defining equation | Term per unit length | Defining equation |
|---|---|---|---|
| Group delay (GD) | $\frac{\partial\phi}{\partial\omega} = \beta_1 L = \frac{L}{v_g}$ | Group velocity $v_g$ | $\beta_1 = \frac{\partial k}{\partial\omega} = \frac{1}{v_g} = \frac{1}{c}(n - \lambda\frac{dn}{d\lambda})$ |
| Group delay dispersion (GDD) | $\frac{\partial^2\phi}{\partial\omega^2} = \beta_2 L$ | Group velocity dispersion (GVD) | $\beta_2 = \frac{\partial^2 k(\omega)}{\partial\omega^2} = \frac{\lambda^3}{2\pi c^2}\frac{d^2 n}{d\lambda^2}$ |
| Third order dispersion (TOD) | $\frac{\partial^3\phi}{\partial\omega^3} = \beta_3 L$ | Third order dispersion (TOD) | $\beta_3 = \frac{\partial^3 k(\omega)}{\partial\omega^3} = \frac{-\lambda^4}{4\pi^2 c^3}(3\frac{d^2 n}{d\lambda^2} + \lambda\frac{d^3 n}{d\lambda^3})$ |

For Gaussian pulse shapes, the propagation task through a dispersive medium with GDD can be analytically solved [8, 89]. This is due to the fact that a Gaussian pulse shape is maintained: (i) upon switching between intensity and field, (ii) upon Fourier transform, and (iii) under the effect of GDD (in the frequency domain). Operating with complex Gaussian functions and back converting to the time domain, one obtains expressions for the pulse duration and chirp after the dispersive medium. For unchirped input pulses the expressions are greatly simplified and the output pulse is broadened (stretched) according to:

$$\tau_L = \tau_0\sqrt{1 + (4\ln 2\frac{\beta_2 L}{{\tau_0}^2})^2}$$

where $\tau_L$ ($\tau_0$) is the output (input) pulse duration (FWHM intensity).

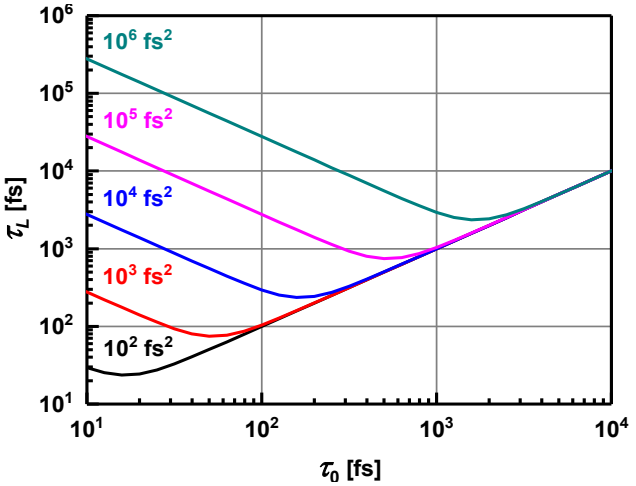


Fig. 4.3 Output versus input pulse duration (FWHM intensity) for a Gaussian pulse propagating in a medium with GDD (numbers indicate the absolute value of the GDD assumed).

Figure 4.3 illustrates the pulse broadening as a function of the initial pulse duration and the GDD. One can see that a relatively short input pulse, i.e. one for which $\beta_2 L > {\tau_0}^2$ is

satisfied, experiences a much stronger broadening. Thus, whether a pulse is understood as short or long depends on the GDD and this can strongly vary with wavelength, e.g., the dispersive broadening can be much more pronounced in the UV compared to the near-IR for a given transparent material.

Similar to GDD, TOD becomes an important factor when TOD $> {\tau_0}^3$, typically only when the pulse duration is below 10 fs in the near-IR.

It shall be outlined here that dispersion is a linear effect which does not change the intensity distribution of the pulse spectral components – only their relative phase in the frequency domain is modified. Accordingly, the FWHM intensity of this distribution, equal to $\Delta\nu = 2\ln 2/\pi\tau_0$ for an unchirped input Gaussian pulse, remains unchanged. The product of the temporal and spatial FWHMs is an important quantity for ultrashort pulses called the time-bandwidth product (TBP):

$$\tau_L \Delta\nu = \frac{2ln2}{\pi}\sqrt{1 + (4\ln 2\frac{\beta_2 L}{{\tau_0}^2})^2}$$

For the unchirped input Gaussian pulse ($L$=0) this product equals 0.441 while the actual TBP of the output pulse shows the extent to which a chirped pulse can be recompressed to its initial duration using a dispersive material with opposite sign of the GVD or what the pulse duration would be if the given GDD is pre-compensated. In any case the goal is always to have a minimum TBP because such pulses, called bandwidth- or Fourier-limited, ensure the best simultaneous temporal and spectral resolution in subsequent experiments where they are applied. The Gaussian pulse shape is a useful approximation to derive analytically the above expressions and also in many other cases. Strictly speaking, only for this pulse shape linear chirp in the time domain (linear dependence of the instantaneous frequency on time) corresponds to a quadratic dependence of the spectral phase on frequency. The Gaussian pulse shape is sometimes used for fitting the pulse shape in mode-locked lasers but theoretically it is more related to active mode-locking and the corresponding equations. As will be seen later, in passively mode-locked SSLs the pulse shape is mostly assumed (also on the basis of theoretical models) to be $\mathrm{sech}^2$ in intensity. For unchirped pulses with this shape one can derive that TBP = 0.315. This product is not very different also for other pulse shapes and so are most of the conclusions made above, e.g. the dependence in Fig. 4.3.

### 4.1.2 Dispersion compensation

Dispersion compensation plays also a key role in the generation of femtosecond pulses. A frequency dependent refractive index will lead to a mode spacing $c/2nL$ which is not constant and the longitudinal modes will not superimpose properly in order to form an ultrashort pulse. The laser cavity may normally exhibit GDD as high as few 1000 $\mathrm{fs}^2$ per round trip, mainly due to the active medium although SA and other substrates may also contribute. Such values have to be compensated by GDD with opposite sign in order to avoid dispersive broadening.

Also, as will be shown later, for soliton formation, negative GDD is required rather than vanishing GDD. There are different elements that can be used for dispersion compensation. The two briefly discussed here are the most widely employed and they were also used in the experimental part of the present work, in the 2 μm spectral region.

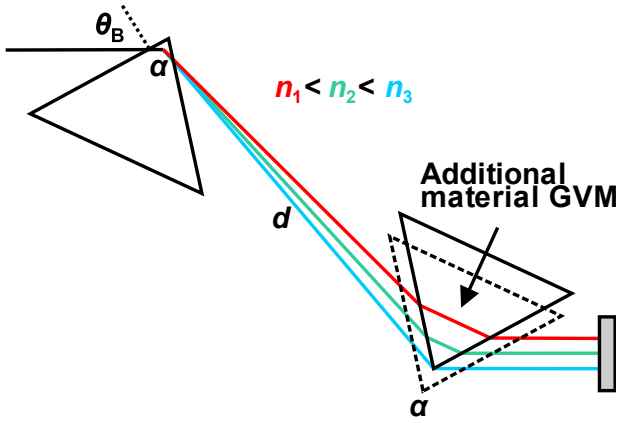


Fig. 4.4 Scheme of a prism pair for GVD compensation. $\theta_B$ and α: Brewster and apex angles.

Antiparallel prism pairs with compensated angular dispersion (i.e. suppressed wavelength selectivity effect) are one of the most commonly used elements for the generation of negative GVD [90]. As shown in Fig. 4.4, different spectral components propagate along different paths between the prisms, in the second prism and after it, which leads to negative overall GVD. Grating pairs have the same property but they are not suitable for intracavity applications due to the higher losses while prisms can be designed as symmetric Brewster angle prisms for the given wavelength (i.e. such that the apex angle α is calculated from the Brewster angle $\theta_B$ to ensure a symmetric beam path) with vanishing Fresnel losses for p-polarization. The resulting 2nd order dispersion which depends on the separation of the two prisms is known as angular GVD whereas the insertion of the prisms introduces additional GVD due to material dispersion. To recombine the spatially offset frequency components behind the second prism, the pair can be complemented by a second one which is a mirror image of it (if ring cavities are employed) or equivalently a plane retro-reflecting cavity mirror can be employed after the second prism (in linear cavities), as shown in Fig. 4.4. In both cases, by introducing a knife edge in the region where the spectral components are spatially separated one can perform some independent tuning of the central wavelength or suppress some unwanted spectral components.

The angular and material GVD of a Brewster prism pair, assuming a separation much larger than the glass path, are given for a single pass by [8],

$$\text{Angular GVD} = \frac{-2\lambda^3}{\pi c^2}\left(\frac{\partial n}{\partial \lambda}\right)^2,$$

$$\text{Material GVD} = \frac{\lambda^3}{2\pi c^2}\frac{\partial^2 n}{\partial \lambda^2}.$$

Initially such prism pairs were employed in dye lasers operating in the visible and Ti:sapphire lasers operating near 800 nm where the material GVD is positive. Thus, angular GVD allowed one to reach zero total GDD or to achieve negative GDD. In all cases, translation of the second prism in Fig. 4.4 enables fine tuning of the total GDD. Figure 4.5 shows the calculated GVD around 2 µm for several commonly used prism materials.

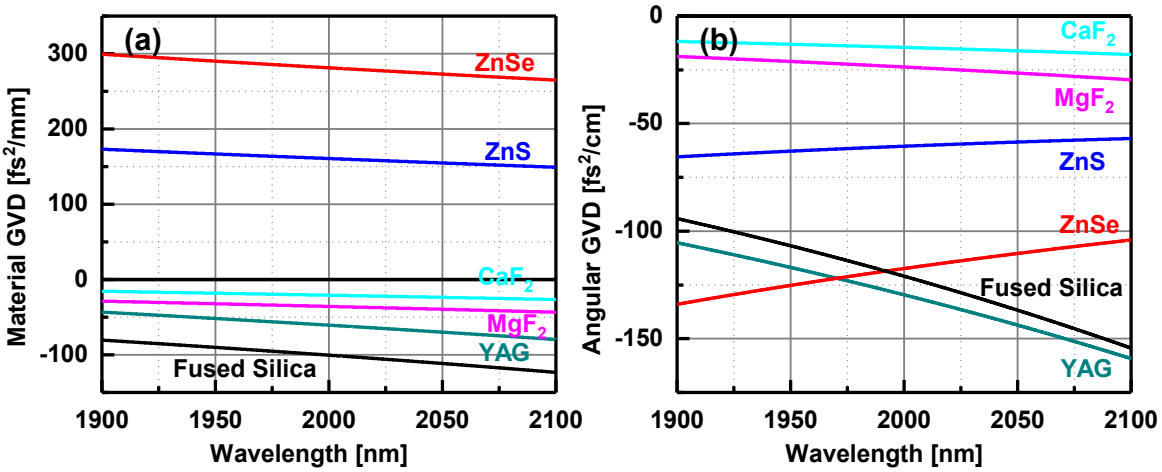


Fig. 4.5 Material (a) and angular (b) GVD of commonly used prism pairs (single pass) for GDD compensation in the 2 µm spectral range. Note that the beam path in the prisms is on the mm scale while between them it is on the cm scale which explains the different units.

Table 4.2 GVD values at 2.02 µm. The Sellmeier equations used are from the references.

| Prism material | Material GVD [$fs^2$/mm] | Angular GVD [$fs^2$/cm] |
|---|---|---|
| $CaF_2$ [91] | − 22.4 | − 15.2 |
| $MgF_2$ [92] o-wave | − 30.0 | − 18.2 |
| YAG [93] | − 64.6 | − 135.3 |
| ZnS [94] | 158.5 | − 59.7 |
| ZnSe [95] | 278.1 | − 114.3 |
| Fused silica [96] | − 105.0 | − 127.4 |

Table 4.2 summarizes the GVD values calculated for several materials at 2.02 µm. Fluoride and oxide materials exhibit anomalous (negative) material GVD around 2 µm. Thus the prism pair can only introduce negative total GDD. Only the low band-gap chalcogenide materials exhibit normal (positive) GVD at this wavelength and permit universal adjustment of the introduced GDD.

While fused silica shows some absorption in this spectral range, $CaF_2$, $MgF_2$ or YAG can be used to provide negative GDD also simply as plates of different thickness. Figure 4.6 shows the double pass (i.e. round-trip in a linear cavity) GDD introduced by placing such 10 mm thick plates at Brewster's angle inside the cavity.

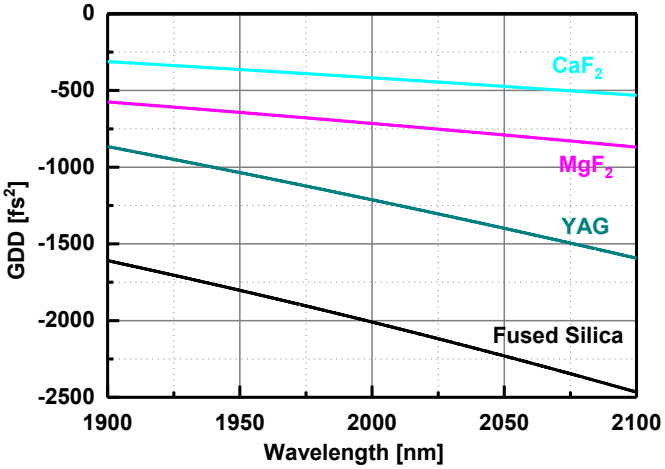


Fig. 4.6 Round-trip GDD introduced by placing a 10-mm thick plate inside the cavity.

The wavelength dependence in Figs. 4.5 and 4.6 is indicative of the TOD because TOD is the 1st derivative of the GVD. It shall be taken into account for extremely short pulses.

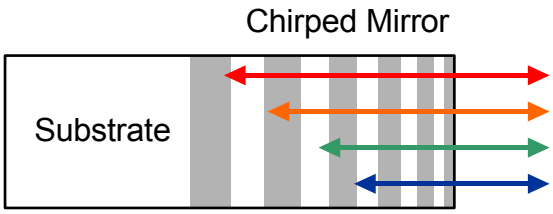


Fig. 4.7 Schematic drawing of a chirped mirror.

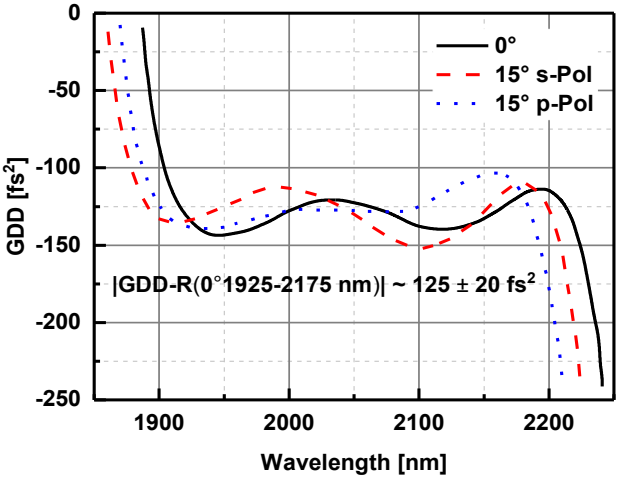


Fig. 4.8 GDD of a chirped mirror for 2 µm SSLs (data from Layertec GmbH).

So-called chirped mirrors present another option for broadband GVD compensation with low insertion losses [97]. The principle can be understood from Fig. 4.7: By appropriate design of the Bragg mirror, longer wavelengths are reflected deeper in the mirror structure and follow a longer optical path which leads to negative GVD and GDD.

However, the straightforward implementation of this idea leads to strong oscillations of the GDD (as a function of frequency or wavelength) known as dispersion ripples. These oscillations can be greatly reduced by numerical optimization which results in complex deviations from the simple chirped design. Figure 4.8 shows typical characteristics of such a chirped mirror applied in the experimental part in 2 μm mode-locked SSLs.

The dispersion ripples in Fig. 4.8 are within ±15 % of the average specified negative GDD. However, Fig. 4.8 represents theoretical curves provided by the supplier because characterization of such mirrors after their fabrication was impossible for them, in contrast to similar products designed for operation at shorter wavelengths.

It shall be emphasized that chirped mirrors, similar to Brewster plates, can modify the GDD only in discrete steps, in contrast to the prism pairs which enable continuous adjustment.

### 4.1.3 Self-phase modulation (SPM)

The optical Kerr effect (also known as AC Kerr effect) shows an extremely rapid response because it is due to a non-resonant process and no electronic transitions take place. On the time scales considered in the present work it can be thought of being instantaneous (< 1 fs) and its dispersion across the optical spectrum of the laser pulse can be ignored. The electric polarization **P** as a function of the electric field **E** can be expanded in a Taylor series [8],

$$\mathbf{P} = \varepsilon_0(\chi^{(1)}\mathbf{E} + \chi^{(2)}\mathbf{EE} + \chi^{(3)}\mathbf{EEE} + \cdots).$$

Taking only the linear and 3rd order terms in this expansion (e.g. for centrosymmetric media where the 2nd order terms are vanishing), the refractive index can be expressed as intensity $I$ dependent [8],

$$n(I) = n(0) + \frac{3\chi^{(3)}}{8n(0)}|\mathbf{E}|^2 = n + n_2 I\,,$$

where $n_2$ denotes the nonlinear refractive index and $n$=$n$(0)..

Through this intensity dependence, the refractive index may vary both in space and in time. The spatial variation leads to self-focusing (Kerr lens) because for all materials $n_2$ is positive. The temporal variation leads to the so-called Self-Phase Modulation (SPM). After a propagation length $L$ in a medium, SPM introduces a time-dependent phase shift to the pulse,

$$\Delta\varphi(t) = 2\pi n_2 \frac{L}{\lambda_0} I(t) = \frac{\omega_0}{c} n_2 L I(t)\,,$$

where $\lambda_0$ and $\omega_0$ denote the center wavelength and frequency. This time-dependent phase shift then leads to frequency modulation or chirping of the propagating pulse,

$$\Delta\omega(t) = \frac{\partial}{\partial t}\Delta\varphi(t) = \frac{\omega_0}{c} n_2 L \frac{\partial I(t)}{\partial t}.$$

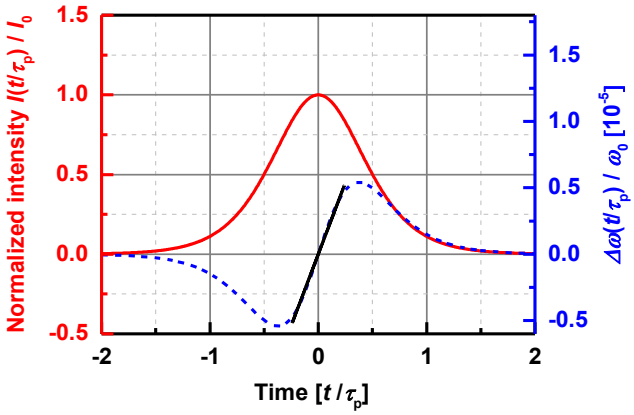


Fig. 4.9 Calculated SPM of a sech$^2$ pulse in terms of normalized intensity and chirp for $L/c\,\tau_0$=100 and $n_2 I_0$=4×10$^{-6}$ where $I_0$ is the peak intensity, $L$ is the material length, and $\tau_p$ is the pulse duration.

For a Gaussian pulse shape in time (and assuming plane waves in space) the chirp is obviously linear near the pulse center. Figure 4.9 shows that this is true also for a sech$^2$-shaped input pulse. SPM generates new frequencies and broadens the optical spectrum but does not change the temporal pulse profile ($I_0$ and $\tau_p$). SPM can be used intracavity (where the intensity is much higher) to broaden the spectrum of a mode-locked SSL [8]. Since the nonlinear refractive index is always positive, the leading edge of the pulse will experience a red shift and the trailing edge a blue shift, thus introducing a positive or up-chirp to an initially unchirped pulse. As will be discussed in the following, the interaction of SPM with GVD is essential for soliton mode-locking. It is clear that positive chirp or at least its linear part can be compensated by negative GVD. By broadening the pulse spectrum, SPM increases the TBP. A broader spectrum obviously supports shorter pulse durations. By combining SPM with negative GVD, the chirp can be eliminated and the pulse duration reduced to the one calculated from the TBP of an unchirped pulse having the same broadened spectral extent.

## 4.2 Haus master equation

Theoretically, mode-locked SSLs are mostly analyzed in the time domain because of the large number of oscillating longitudinal modes. In numerical modeling, it is easier to consider dispersion in the frequency domain because this can be done without approximations. Assuming small changes due to each pulse shaping mechanism affecting its intensity and/or phase, it is possible to analytically treat the problem entirely in the time domain which relies on a master equation first solved by Haus [98]. Essentially this assumption which allows one to expand exponentials up to linear terms means that the order of the different elements in the model is unimportant and the pulse will have the same characteristics wherever outcoupled. Assuming only time but no spatial dependence on the transversal coordinates, Haus first derived an unchirped closed-form solution with sech$^2$ intensity dependence of the pulse shape for the case of a slow SA and saturable gain medium (dye) without SPM and GVD effects but considering a parabolic expansion of the gain (Lorentzian gain shape function assumed) in frequency which accounts for dispersion and works as a filter limiting the bandwidth.

Additional assumptions included weak (expandable up to 2nd order terms) saturation of the SA and gain medium by the instantaneous pulse fluence. Almost simultaneously, Haus derived the same pulse shape as a closed-form solution in a similar model of mode-locked SSLs where the weakly saturated SA is fast (instantaneous) and the gain is not saturated by a single pulse at all [99]. Following this pioneering work [100], similar analytical approaches were applied to many different lasers and mode-locking techniques. In particular, the addition of SPM and GVD was shown to lead to the same intensity profile but the closed-form solution was chirped with a *ln*(sech) phase dependence on time [101, 102]. That is why the master equation is called nowadays also Haus equation: It is also a very useful approach for numerical treatment of the problem whereby iterating the pulse-shaping effects in many round trips a steady-state is reached with certain pulse parameters. No ansatz for the pulse shape is necessary in this case and most of the assumptions stated above can be avoided. Numerical simulations start normally with some kind of noise assumed. Then the pulse develops from this noise due to the pulse shaping mechanisms which favor some intensity/energy spike reaching finally a steady-state after many round trips, cf. Fig. 4.10.

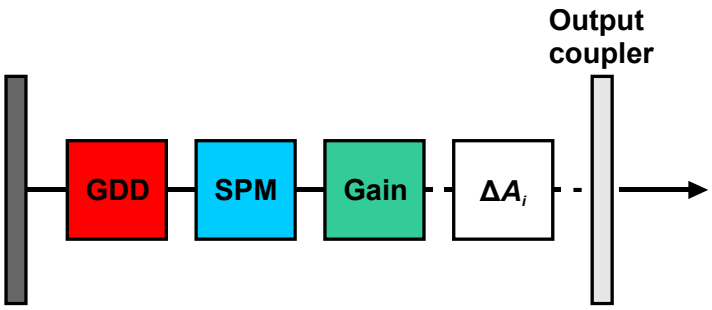


Fig. 4.10 Model of a mode-locked laser explaining the derivation of the Haus master equation. Blocks indicate different shaping effects acting on the complex pulse envelope A(t).

The principles for calculation of such a steady-state can be summarized as follows:

- The pulse that evolves in the cavity after many round trips until a steady-state is reached, is described as a complex amplitude $A(t)$ in the time domain.
- In the steady-state the pulse reproduces itself after one round trip. In mode-locked laser theory a steady-state is defined by the intensity and the chirp. In analytical treatments with the above pulse shape ansatz, the 4 parameters that are derived are the pulse duration, its maximum intensity, a linear chirp coefficient and the central frequency (or the frequency offset) because it might deviate from the maximum of the gain assumed to be Lorentzian in shape.
- Two additional parameters are necessary in order to obtain analytically a closed-form solution. The steady-state pulse may experience a small time shift after one round trip and also a small constant phase shift. The first effect means that pulse shaping effects may shift the pulse in time and its propagation velocity is different from the group velocity as derived for passive optical materials. Experimentally, this generalized

pulse velocity defines the observed pulse repetition rate from the mode-locked laser. The second effect corresponds to a correction in the phase velocity. Both effects are necessary to take into account also in numerical simulations in order to obtain a steady-state but were considered to be largely irrelevant to experimental optimization of the operating regime. However, more recently, great attention is paid to the carrier-envelope phase (CEP) stability of such mode-locked SSLs especially when they generate few-cycle pulse durations. The phase slip observed outside the cavity is directly related to the phase shift in the Haus model because the pulse train is a result of the periodic outcoupling of the circulating intracavity pulse in the model each time it hits the OC.

- The changes $\Delta A_i$ of the pulse complex envelope $A(t)$ due to different pulse shaping mechanisms in the cavity (such as gain, saturable loss or absorption, dispersion, SPM, non-saturatble loss etc.) must cancel each other with vanishing overall effect on the pulse intensity and chirp.

Table 4.3 Main linearized operators $\Delta A_i$ that define the change of the pulse envelope $A(t)$ at resonance [1, 102]. The envelope $A(t)$ is normalized in such a way that $|A(t)|^2$ corresponds to the instantaneous power $P(t)$ of a plane wave. $L$ is the round trip length of the relevant element.

| Laser cavity element | Linearized operator | Constants |
|---|---|---|
| GDD | $\Delta A \approx iD\frac{\partial^2}{\partial t^2}A$ | $D = \frac{\beta_2 L}{2}$ : dispersion parameter<br>(half of the GDD per cavity round trip) |
| SPM | $\Delta A \approx -i\delta_L \lvert A\rvert^2 A$ | $\delta_L = \frac{kn_2 L}{S_L}$ : SPM coefficient<br>$S_L$: laser mode size in the Kerr medium |
| Gain | $\Delta A \approx [g + D_g\frac{\partial^2}{\partial t^2}]A$ | $D_g = \frac{g}{\pi^2 \Delta_g^2}$ : gain dispersion at resonance<br>$g$: saturated amplitude gain coefficient<br>$\Delta_g$: gain bandwidth (FWHM) |
| Non-saturable loss | $\Delta A \approx -lA$ | $l$: amplitude loss coefficient without the SA |
| Constant phase shift | $\Delta A \approx i\psi A$ | $\psi$: phase shift |
| Fast SA | $\Delta A \approx -q_0 A + \gamma_A \lvert A\rvert^2 A$ | $\gamma_A = \frac{q_0}{I_{sat} S_A}$ : SA coefficient<br>$q_0$: maximum saturable amplitude loss<br>$I_{\mathrm{sat}}$: saturation intensity of the fast SA<br>$S_{\mathrm{A}}$: laser mode size in the SA |
| Slow SA | $\Delta A = -q_0\left(1 - \epsilon + \frac{\epsilon^2}{2}\right)A$ | $\epsilon(t) = \int_{-\infty}^{t} \lvert A(t')\rvert^2 \, dt' / S_A F_{sat}$<br>$q_0$: maximum saturable amplitude loss<br>$F_{\mathrm{sat}}$: saturation fluence of the slow SA<br>$S_{\mathrm{A}}$: laser mode size in the SA |

Table 4.3 summarizes the most important pulse shaping effects in passively mode-locked lasers and their linearized operators (i.e. assuming small changes).

## 4.3 Passive mode-locking mechanisms

One distinguishes three main passive mode-locking mechanisms according to the relaxation time of the saturable loss or SA and the gain medium, see Fig. 4.11 [1].

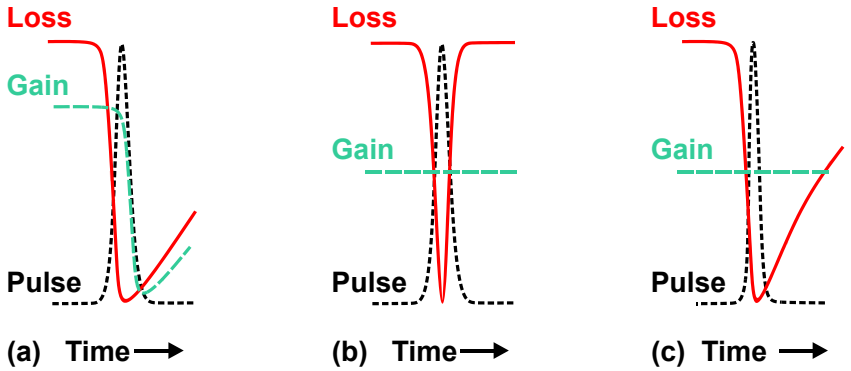


Fig. 4.11 Different mechanisms for passive mode-locking: (a) slow SA with gain saturation of the active medium, (b) fast SA and (c) slow SA mode-locking without gain saturation (after [1]).

- Slow SA mode-locking with instantaneous gain saturation: Found only in color center SSLs. The SA is shaping (shortening) the leading edge of the pulse whereas depletion of the gain leads to negative gain (due to the remaining non-saturable losses) for the trailing edge which is also shortened. The resulting net positive gain window supports sub-100-fs pulse fomation, much shorter than the characteristic (ns) time constants of the SA and the gain medium. Noise outside the pulse is suppressed by negative gain.

- Fast SA mode-locking with non-saturable gain: The net positive gain window is formed solely by the SA whose saturation is intensity dependent. KLM is very close to an ideal fast SA due to the extremely rapid response of the AC Kerr effect.

- Slow SA mode-locking with non-saturable gain: Although there is no obvious shaping effect for the trailing edge, the SA delays the pulse in time thus “swallowing” any noise growing behind at the trailing edge. Only slow SAs and saturable gain media (the latter accelerate) have this property to modify the pulse velocity ($1^{st}$ order time derivatives in the master equation) because saturation is fluence dependent in this case

## 4.4 Solitons

Under solitons one understands highly localized pulses traveling at a constant speed without changing their shape. Real optical solitons only exist for propagation in fibers where all the pulse shaping effects are distributed and occur simultaneously. In bulk lasers, e.g. SPM and GVD are due to different discrete elements and occur separately (i.e. in the laser active medium and in the prism pair) with the pulse shaping effects balanced only within a complete round trip. The pulse reproduces itself after every round trip but its parameters in different positions inside the cavity are slightly different. The term used for such pulse formation when it is dominated by the SPM and GVM effects is soliton-like mode-locking. It should be

outlined that numerically, the ultrashort pulse propagation and the mode-locked laser modeling are treated in the same manner because the split-step method applied for pulse propagation separates all the shaping effects and different thin slices of the medium are considered that present only one of them, each slice introducing only small modifications to the pulse. Thus the analogy is well substantiated.

With the expressions from Table 4.3 (fast SA assumed), the Haus master equation reads:

$$\sum_i \Delta A_i = \left\{ i\left[ D\frac{\partial^2}{\partial t^2} - \delta_L |A(t)|^2 \right] + \left[ g - l - q_0 + D_g \frac{\partial^2}{\partial t^2} + \gamma_A |A(t)|^2 \right] \right\} A(t) = 0,$$

which is known as the generalized Ginzburg-Landau equation. The time coordinate is in a frame moving with the pulse. For simplicity, 1st order derivative terms responsible for the time shift of the pulse (the actual pulse propagation velocity) and the phase shift term responsible for the actual phase velocity are omitted. The saturation of the fast SA in the above equation is weak (i.e. only terms linear in intensity are included) and this allows one to find analytical solutions. A slow SA is treated in a similar way and an assumption of weak saturation (up to quadratic terms in fluence, cf. Table 4.3) enables again an analytic treatment. In the absence of gain and loss, the above equation reduces to the nonlinear Schrödinger equation (the terms in the first square brackets) which has been widely studied in soliton theory. For negative GVD ($D < 0$) and positive SPM ($n_2 > 0$) the well-known fundamental soliton solution is found by perturbation theory [8] (this theory predicts also "higher" order non-stationary solitons whose more complex shape is reproduced periodically) which reads:

$$A(t) = A_0 \operatorname{sech}\left(\frac{t}{\tau}\right) e^{-i\psi_s(z)}$$

Such a pulse propagates without distortion in a medium with the above two properties and only its phase changes along the propagation coordinate $z$ in accordance with $\psi_s(z)$. The soliton pulse duration in terms of FWHM intensity is $\tau_\mathrm{p} = 1.763\tau$ ($2\operatorname{arcosh}(\sqrt{2}) \approx 1.763$). The spectral intensity of such an unchirped pulse has the same sech$^2$ profile with a FWHM = $1.763/(\pi^2\tau)$ [103]. From these expressions one obtains the previously mentioned TBP = 0.315. For given GVD and SPM coefficients, the pulse energy $\epsilon_\mathrm{p}$ and the pulse duration of the fundamental soliton obey the so called "area theorem" [100].

$$\tau_\mathrm{p} = 1.763\frac{2|\mathrm{D}|}{\delta_\mathrm{L}\epsilon_\mathrm{p}},$$

which can be easily obtained by integration of the intensity over time. This relationship is very useful for identification of soliton-like regimes in mode-locked lasers because it predicts reduction of the pulse duration inversely proportional to the average output power which can be increased e.g. by the pump power. It shall be repeated here that by "solitons", one means the fundamental solution to the nonlinear Schrödinger equation which can be easily confirmed

by simple substitution with the above defined pulse shape. However, solutions to the Ginzburg-Landau equation are also called solitons in a more general sense.

Ultrashort laser pulses are often characterized by intensity autocorrelations [1]. While the autocorrelation function of a Gaussian pulse is also Gaussian with a FWHM increased by a factor of $\sqrt{2}$, for $\mathrm{sech}^2$-shaped pulses the fit of the autocorrelation (AC) functions shall be performed with a more complex expression derived in [103]:

$$G_2(\tau) = \frac{3(\tau \cdot \cosh(\tau) - \sinh(\tau))}{\sinh^3(\tau)}$$

From the fit, the pulse width $\tau$ can be derived and from it - the FWHM intensity $\tau_p$.

## 4.5 Mode-locking stability

There exist two essential limits for the mode-locking stability in SSLs, the transition to Q-switched mode-locking (QSML) at powers lower than the threshold for stable steady-state operation and soliton break-up above the limits of the CWML regime. In the following, these two phenomena as well as the stability criteria will be briefly discussed.

### 4.5.1 Q-switched mode-locking (QSML) instabilities

When a CW laser is disturbed during operation, e.g. by fluctuations of the pump power, its output power does not immediately return to its steady-state. Instead, a number of spikes called relaxation oscillations are emitted before the CW steady-state is reached again. This is typical for SSLs with their lifetimes which are much longer than the cavity lifetime (the damping time in which the radiation accumulated is dissipated in the absence of further pumping due to the outcoupling and parasitic losses). This situation may occur also in a passively mode-locked SSL because the SA favors higher energies which increase the cavity Q-factor. This tendency to Q-switching is called then Q-switching instability.

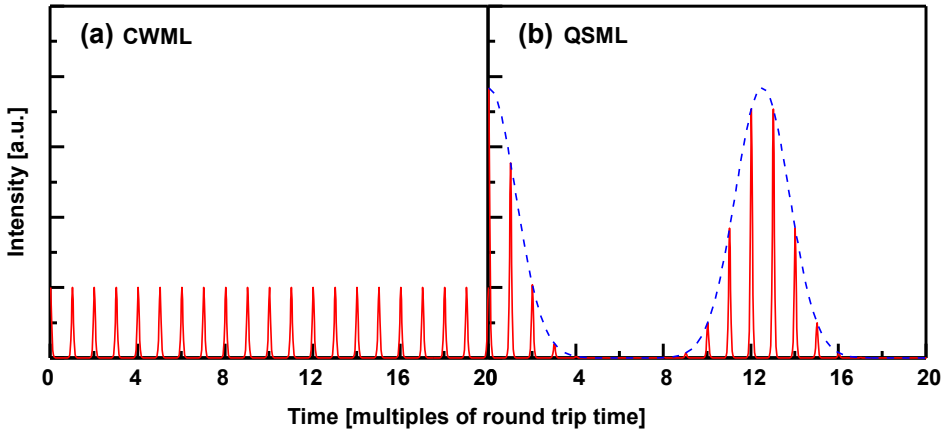


Fig. 4.12 Schematic trace of stable CWML (a) and a mode-locked laser exhibiting large Q-switching instabilities (QSML with 100% modulation) (b). The average laser power is the same.

Saturation of the gain could provide a stabilizing feedback but as already mentioned the gain is not saturated by a single ultrashort pulse in $Ln^{3+}$ SSLs. Figure 4.12 illustrates the QSML regime in comparison with true CWML. As shown in Fig. 4.12b, while the ultrashort pulse train follows at a repetition rate around 100 MHz, Q-switching leads to an additional intensity modulation with frequency typically in the kHz range. Such a modulation is normally unwanted because all other pulse characteristics vary within the Q-switched envelope of the train and the high peak intensity may lead to damage to the SA. However, for certain applications (e.g. material processing) QSML with 100% modulation as the one shown in Fig. 4.12b may be useful, at least in the picosecond regime. Note that this figure illustrates a stable regime (QSML) when a bunch of ultrashort pulses (a macro-pulse) is emitted at low repetition rate as in a steady-state Q-switched laser. In most cases, however, Q-switching instabilities lead to noisy behavior and such "stable" macro-pulses cannot be seen with fast a photodiode and an oscilloscope.

For SSLs operating in the picosecond regime, a simple stability criterion in terms of intracavity pulse energy $\epsilon_\mathrm{p}$ has been derived for stable CWML without Q-switching instabilities [104]:

$$\epsilon_\mathrm{p}^2 > \epsilon_\mathrm{p,c}^2 = \epsilon_\mathrm{sat,L}\epsilon_\mathrm{sat,A}\Delta R\ ,$$

where $\epsilon_\mathrm{p,c}$ is the critical (minimum) intracavity pulse energy required for stable CWML.

$\epsilon_\mathrm{sat,L} = S_\mathrm{eff,L}F_\mathrm{sat,L}$ is the saturation energy of the gain medium, i.e. the energy that depletes the gain to 1/e of its low signal value. To prevent the laser from QSML, the effective mode area $S_\mathrm{eff,L}$ in the gain medium should be as small as possible. However, this mode area should be also matching the pump size to achieve high efficiency and the overlap should ensure that higher-order transverse modes are suppressed. The saturation fluence of the laser medium $F_\mathrm{sat,L} = h\nu/2\sigma_g$ (the factor 2 accounts for 2 passes per round trip in a linear cavity) is inversely proportional to the gain cross section $\sigma_\mathrm{g}$, i.e. materials with higher gain show weaker tendency for QSML [104]. It shall be outlined that contrary to the general reasoning, the upper-state lifetime of the active medium is not directly involved in the criterion for stability against QSML [104].

Both the saturation energy $\epsilon_\mathrm{sat,A}$ and the modulation depth $\Delta R$ of the SA enter the criterion for stable CWML. Reducing both of them will improve the stability. By focusing the beam tighter onto the SA, the effective mode area $S_\mathrm{eff,A}$ can be reduced and thus $\epsilon_\mathrm{sat,A} = S_\mathrm{eff,A}F_\mathrm{sat,A}$ will be lower. However, at higher powers this may not only lead to optical damage but also will require a trade-off with the pulse break-up tendency. On the other hand, reducing the modulation depth $\Delta R$ will lead to a longer steady-state pulse duration and weaker self-starting tendency for CWML operation [105, 106].

In the femtosecond regime, the tendency towards QSML is significantly reduced [104]. As the energy of a pulse grows slightly, SPM and/or any pulse shortening effect will broaden the pulse spectrum. A broader spectrum reduces the effective gain and provides a negative

feedback thus relaxing the criterion for stable CWML which in its modified version reads [104]

$$\epsilon_{\mathrm{sat,L}} 2gK^2\epsilon_{\mathrm{p}}^3 + \epsilon_{\mathrm{p}}^2 > \epsilon_{\mathrm{sat,L}}\epsilon_{\mathrm{sat,A}}\Delta R\,,$$

with

$$K = \frac{0.315}{1.763}\frac{4\pi n_2 L_L}{DS_{\mathrm{eff,L}}\lambda_0\Delta_g}\,,$$

Here $L_L$ and $S_{\mathrm{eff,L}}$ are the single-pass length and the effective area in the Kerr medium assumed here to coincide with the active medium and the other parameters were defined in Table 4.3.

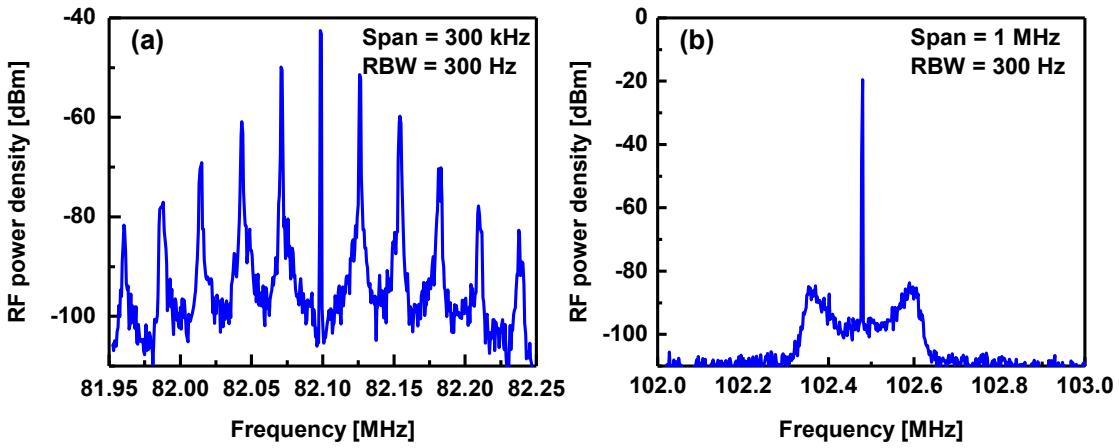


Fig. 4.13 RF spectra of the first beat note for typical QSML of the Ho:YAG laser studied in this work: (a) strong Q-switching instability with strong side bands and (b) weak Q-switching instability with weak side bands. Such regimes were obtained by misalignment of the cavity (cf. Chapter 5).

QSML in bulk SSLs leads to characteristic radio-frequency (RF) spectra with side bands of the fundamental beat note or modulation with periods of several tens of kHz. Such RF spectra present a powerful tool to measure different kinds of noise and fluctuations in mode-locked lasers [107]. As an example, Fig. 4.13 shows RF spectra recorded in the QSML regime of the Ho:YAG ceramic laser studied in Chapter 5. Apart from the fundamental repetition rate beat note at 82.1 MHz, one can clearly see in Fig. 4.13a additional bands with a separation of 27 kHz. A weak Q-switched instability leading to modulation of the CW pulse train results in RF spectra as the one shown in Fig. 4.13b.

### 4.5.2 Soliton break-up

As the steady-state pulse energy of a mode-locked SSL grows (e.g., by increasing the pump power) it might happen that the slow SA is completely saturated and cannot further stabilize a single soliton-like pulse. High order solitons accommodating more energy exist as solutions

to the nonlinear Schrödinger equation but they are not steady-state and reproduce their shape (in a laser) only after a certain number of round trips corresponding to their period. Such solitons have been indeed observed by sampling the output at the soliton period to record the corresponding AC trace [108].

The high order solitons under certain conditions may break up into two fundamental solitons with lower energy and longer duration (according to the area theorem). Such a double pulse sequence will prevail thanks to better stability against noise. Decreasing the magnitude of the introduced negative GDD will also lead to a formation of high order soliton since the pulse duration decreases and at a certain point the gain cannot support the broadened spectrum. This finally leads to the break-up into two pulses with longer duration.

Normally the excess energy is carried by two or more pulses with a separation comparable to the cavity round-trip time. Achieving a so-called harmonic mode-locking (operation at multiple of the repetition rate as known from active mode-locking [109]) is interesting for increasing the repetition rate. Many observations of this kind can be found in the literature but in passively mode-locked SSLs the spacing between the pulses is irregular and subject to spontaneous changes [110]. An interesting steady-state femtosecond regime was described in [111] for a SESAM mode-locked Ti:sapphire laser with an intracavity spectral filter, in which the pulses were very close to each other (separation comparable to the pulse length). This study was performed by changing the GDD and monitoring the output energy and duration of the single and double pulses. The soliton break-up observed could not be explained in the framework of the nonlinear Schrödinger equation because the pulse broadening of the double pulses was less than the predictions. The explanation presented was based on the combined effects of saturable absorption, spectral filter, and soliton-soliton interaction as known from the nonlinear Schrödinger equation.

For two pulses with exactly the same amplitude and phase (no phase difference), periodic collapse occurs as a result of the soliton interaction [111]. However, when the pulses get closer (separation less than ~ 5 times the SA recovery time), the second pulse will reach the SA when it is still partly bleached and will experience less loss, which will lead to slightly different amplitudes of the two pulses [111]. A phase difference between the two pulses will relocate the spectral distribution of the pulse energy and in the presence of a gain filter effect this can provide another feedback mechanism. It turns out that stable pulse pairs exist with small separation if the relative phase is such that attractive and repulsive forces average out. These are generalized fundamental solitons, however, which obey the generalized Ginzburg-Landau equation.

Apart from the AC function, such soliton bound-states can be recognized from their characteristic optical spectra. The superposition of the two coherent pulses with a temporal separation $T$, and phase difference $\phi$ will form an interference pattern in the spectral domain. Let the amplitude of the two pulses be approximately equal and the envelope $A(t)$ is normalized in such a way that $|A(t)|^2$ gives the intensity $I(t)$ of each of them, as in Table 4.3. If the second pulse is shifted in time by $T$ and exhibits a phase difference of $\varphi$, the Fourier transform of the doublet will be given by:

$$A_D(\Omega) = \mathcal{F}\left[A(t) + A(t+T)e^{i\phi}\right] = A(\Omega) + e^{i(T\Omega+\phi)}A(\Omega) = (1 + e^{i(T\Omega+\phi)})A(\Omega),$$

where $A(\Omega) = \mathcal{F}[A(t)]$. Since the fast oscillating terms are separated and the slowly varying envelope function $A(t)$ is considered here, the relative frequency $\Omega = \omega - \omega_0$ appears as an argument where $\omega_0$ is the center (carrier) frequency of the field. The spectral intensity $I_D(\Omega)$ of the doublet is then:

$$I_D(\Omega) = A_D(\Omega)A_D(\Omega)^* = 2[1 + \cos(T\Omega + \phi)]I(\Omega),$$

Without time or phase shift ($T$=0, $\varphi$=0) the two amplitudes simply add resulting in 4-fold increase of the intensity. In the general case, however, the spectral intensity corresponding to a single pulse $I(\Omega)$ is modulated at a frequency $\Omega_{mod} = 1/T$. Figure 4.14 shows the calculated spectrum of such a pulse doublet with a zero phase difference.

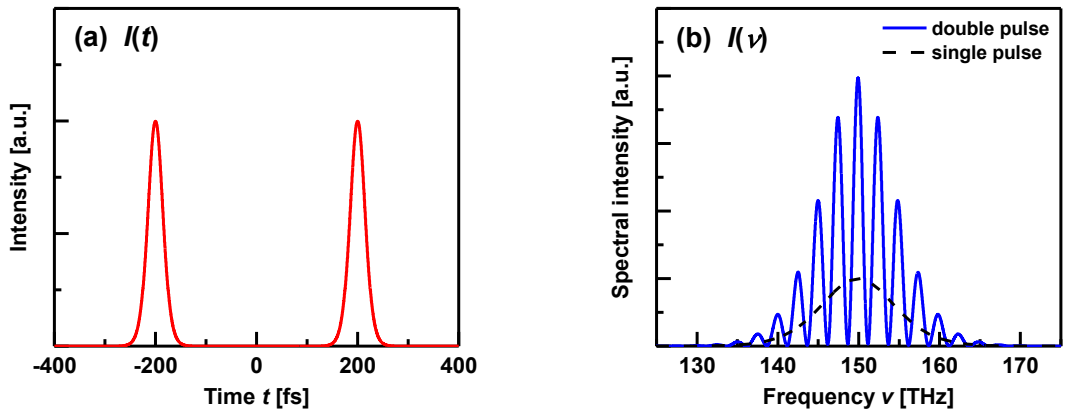


Fig. 4.14 A doublet of closely spaced ultrashort pulses of equal amplitude and phase (a) and its spectrum (b). The pulse duration (FWHM) is $\tau_p$ = 50 fs assuming sech$^2$-shape and the separation amounts to 400 fs. The carrier frequency corresponds to $\lambda_0$ = 2 μm (150 THz). For comparison, the single pulse spectrum is also shown by a dashed line in (b).

The modulation period measured in nanometers will be $\Delta\lambda_{mod} \approx \lambda_0^2/cT$ where $\lambda_0 = 2\pi/\omega_0$.

As will be seen in Chapter 5, such stable bound states have been observed for the first time in the present work for a mode-locked $Ln^{3+}$ SSL without any spectral filter.

# Chapter 5
# Passively mode-locked 2-μm lasers: experimental results

The first mode-locking of a 2 μm laser (Ho:YAG) was realized in 1981 by an acousto-optic modulator (active mode-locking) [112], however, this was a Xe flash lamp pumped laser operating at liquid $N_2$ temperature only in pulsed mode (up to 5 Hz). Mode-locking was obtained both in free-running and Q-switched modes and pulse durations of $\tau_p = 0.57$ ns were measured in the latter case. The first room temperature steady-state mode-locking (again by acousto-optic modulator) was achieved in 1991 with Cr,Tm:YAG and Cr,Tm,Ho:YAG crystals pumped by a Kr-ion laser (the Cr co-doping served as a sensitizer) [113] and with Tm:YAG pumped by a Ti:sapphire laser [114]. The Cr,Tm:YAG laser generated pulses as short as 45 ps at 2.013-2.025 μm for an average output power $P_{out}$ = 160 mW at ~ 123 MHz [113] and the Tm:YAG laser generated pulses of $\tau_p$ = 35 ps at 2.01 μm for $P_{out}$ = 70 mW at 300 MHz [114]. The pulse duration from the Cr,Tm,Ho:YAG laser was 800 ps for $P_{out}$ = 60 mW at ~ 123 MHz, however, the operation of this laser was unstable [113].

Only few years later, another milestone was accomplished with the first sub-ps operation demonstrated with a Tm-fiber laser passively mode-locked by nonlinear polarization rotation [115]. This laser operated in the soliton regime, producing pulse durations of $\tau_p$ ~ 350-500 fs at ~ 1.8-1.9 μm. with $P_{out}$ of only 320 μW at ~ 17.5 MHz. In the following years, great progress was achieved with such Tm-fiber lasers (later on also with Er- and Ho-co-doping or Raman frequency conversion for extended spectral coverage). More recently, their output characteristics have been greatly improved both in terms of pulse duration (e.g. $\tau_p$ = 45 fs pulses with $P_{out}$ = 13 mW at 67.5 MHz, after external prism pair compression [116]), and $P_{out}$ (2.5 W at the same repetition rate, with a CW pumped Tm-fiber amplifier for $\tau_p$ = 48 fs [117]).

Notwithstanding these impressive results, fiber lasers tend to be more limited for certain applications such as the generation of frequency combs and carrier-envelope phase (CEP) stabilization as few-cycle seed sources for further (laser or parametric) amplification because of excess noise which arises from spontaneous emission, the low cavity quality factor, and large intracavity nonlinearities [118], as well as because of the structured spectral shape [115, 116]. These limitations stimulate the research on bulk mode-locked lasers as an alternative solution.

In 2009, the first passive CWML of a bulk 2-μm $Ln^{3+}$ laser was demonstrated employing the monoclinic Tm:KLuW crystal with a transmission-type SWCNT-SA [80]. Stable and self-starting operation with $\tau_p$ = 9.7 ps was obtained at 1.944 μm for $P_{out}$ reaching 240 mW at 126 MHz. This result triggered extensive research by other groups employing different host materials and SAs. With a GaSb-based SESAM and the disordered tetragonal crystal

Tm,Ho:$NaY(WO_4)_2$, sub-ps operation could be demonstrated [119]. Pumped by a Ti:sapphire laser, this mode-locked Tm laser produced transform-limited pulsed with $\tau_p = 570$ fs at 2.055 μm for $P_{out} = 130$ mW at 118 MHz. With the same type of SA and different hosts ~ 200 fs pulses were generated at ~ 2.06-2.1 μm employing again Tm,Ho:$NaY(WO_4)_2$ [120] and some sesquioxide-based hosts (Tm:$Sc_2O_3$ crystal [121] and Tm:$Lu_2O_3$ ceramic [122]). The investigation of carbon nanostructures as SAs continued, demonstrating pulse durations of 354 fs at 2.01 μm using a reflection-type graphene-SA with Tm:CLNGG (disordered garnet) as a gain medium [62]. Employing a transmission-type SWCNT-SA resulted in the shortest pulses so far: $\tau_p = 175$ fs with Tm:$Lu_2O_3$ [123] and $\tau_p = 141$ fs with Tm:KLuW [124].

This chapter summarizes the main experimental results achieved in the present work on passive mode-locking of bulk Tm and Ho lasers near 2 μm. First, the laser cavity used is described including some general aspects common for all experiments. The CWML laser results cover three garnet ceramics (Tm:YAG, Tm:LuAG and Ho:YAG) which operated in the picosecond regime with GaSb-based SESAMs, the uniaxial Tm:CALGO crystal which generated shorter pulses reaching sub-ps duration with the same SESAMs, and finally a more comprehensive and systematic study of the monoclinic Tm:MgW crystal applying different SAs (SESAMa, SWCNTs, and graphene) and intracavity GVD compensation techniques, which led to the generation of the shortest, sub-100 fs pulses by a bulk mode-locked laser near 2 μm.

## 5.1 Experimental set-up

For efficient operation of a long cavity laser with longitudinal pumping, a beam waist shall be formed in the active medium and the cavity design should ensure good mode matching with the focused pump beam over the Rayleigh range. Usually the pump mode size is slightly smaller than the laser mode size in order to stabilize the laser against higher transversal modes which, having slightly different eigen-frequencies, tend to deteriorate the mode-locking. In this case, as briefly mentioned in Chapter 4, the Kerr lens effect may act spatially as a pinhole. In the presence of such self-focusing and also due to the thermal lensing effect in the active medium (e.g. heat released as a result of non-radiative relaxation), in a real laser the mode size differs from the one calculated by the standard ABCD matrix formalism.

A cavity focus is created most often by employing two concave folding mirrors ($M_1$ and $M_2$ in Fig. 5.1) in X- or Z-shaped cavities [125]. For short (few mm) crystal lengths as typically used, there is no need to manufacture Brewster rhombs and the active element is simply a plate inclined under Brewster's angle for the corresponding polarization. Such a plate introduces astigmatism which can be compensated in the beam waist by the incidence angle on the two concave folding mirrors. In the experiments described in this chapter these two folding mirrors had a Radius of Curvature (RoC) of −100 mm. As shown in the example in Fig. 5.2c, the calculated beam waist in the gain medium with such mirrors, depending on the exact separations, can be of the order of ~ 30 μm (S) × 60 μm (T), where S and T denote the sagittal and tangential planes, respectively.

The benefit of such a symmetric X- or Z-shaped cavity is that it can be easily extended for dispersion compensation, SA or other elements in the two arms and still have a single output. In the X-type cavity employed in the present work (Fig. 5.1), the right arm ($M_2$ to the end mirror) can be adapted for different SAs, i.e. reflection- or transmission-type SAs, while the left arm ($M_1$ to the output coupler, OC) can be used for dispersion compensation or wavelength tuning purposes.

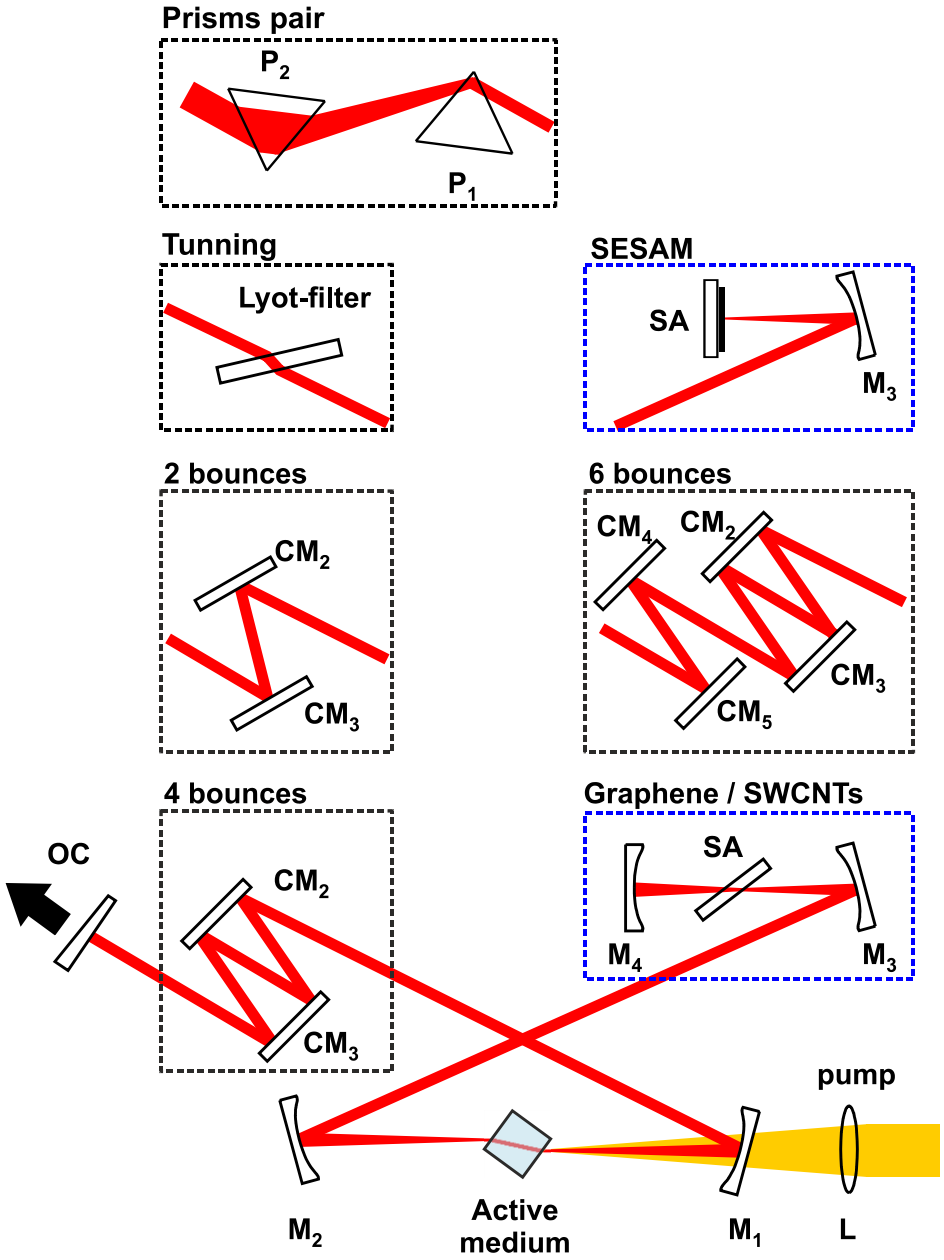


Fig. 5.1 Scheme of the cavity designed for different mode-locked 2 µm lasers: Black boxes represent alternative intracavity GVD compensation or tuning elements and blue boxes - different SAs. The optional Lyot filter inserted under Brewster's angle is a standard low-loss cavity element applied for wavelength tuning in CW lasers whose operation is based on birefringence [126].

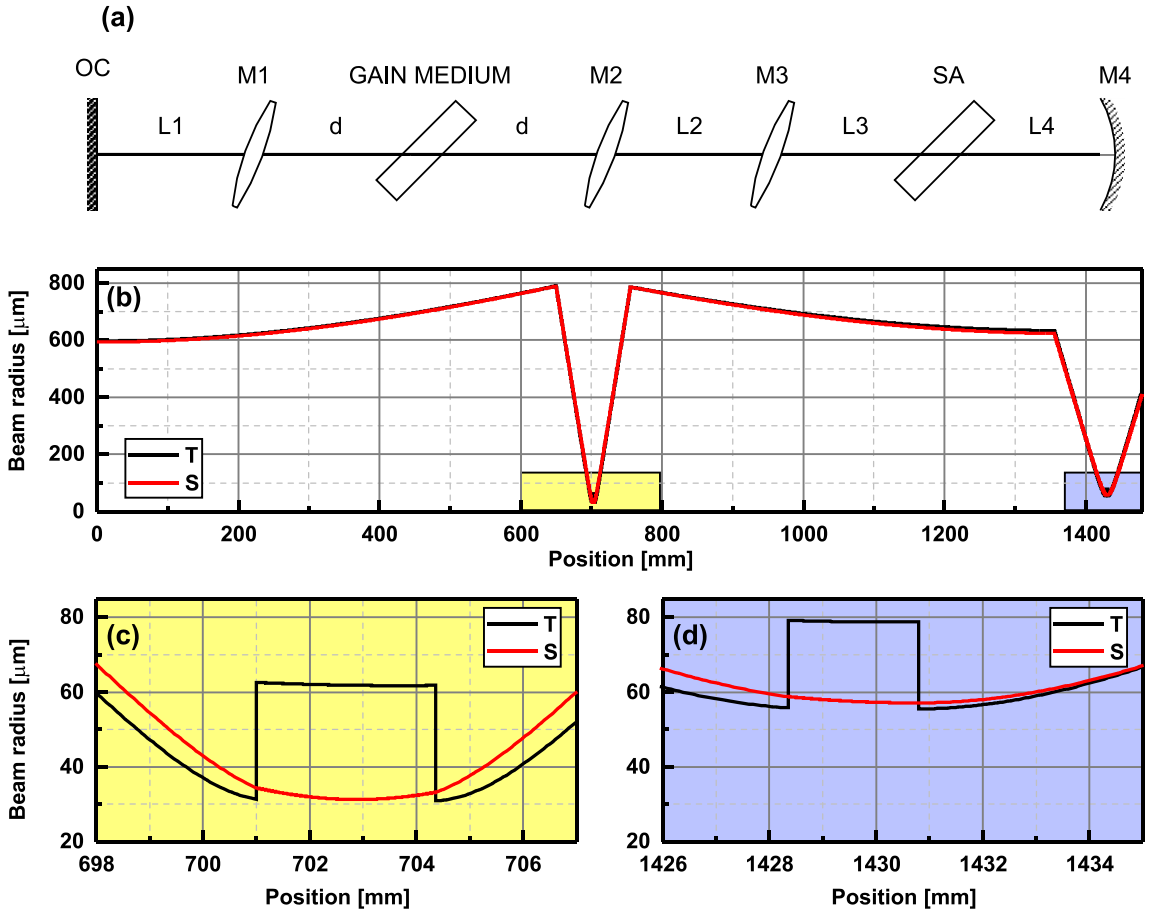


Fig. 5.2 Equivalent cavity scheme (a) and calculated beam sizes for the specific configuration of the mode-locked Tm:MgW laser (b), zoomed near the two beam waists, (c) and (d). The RoC of $M_3$ and $M_4$ is -150 and -50 mm, respectively, and the distances shown (abscissa) are measured from the OC.

Table 5.1 Mode-locked 2 µm lasers studied and their most important parameters: PP / CM represent prism pair / chirped mirrors for intracavity GVD compensation. S / T represent sagittal / tangential plane for the transmission-type SAs under Brewster's angle.

| Host | Doping concentration [at. %] | Pump source | $\lambda_P$ [nm] | SA | RoC $M_3/M_4$ [mm] | Beam radius on SA [µm] | GVD |
|---|---|---|---|---|---|---|---|
| Tm:YAG | 4 / 10 | Ti:sapphire | 785 | SESAM | −100/NA | 70 | PP |
| Tm:LuAG | 4 | Ti:sapphire | 787 | SESAM | −150/NA | 100 | PP |
| Ho:YAG | 1 | Tm:fiber | 1908 | SESAM | −100/NA | 70 | – |
| Tm:CALGO | 6 | Ti:sapphire | 798 | SESAM | −100/NA | 70 | PP |
| | | | | SESAM | −100/NA | 70 | Plate |
| Tm:MgW | 0.89 | Ti:sapphire | 796 | SWCNT | −150/−50 | 60(S)/80(T) | PP / CM |
| | | | | Graphene | −150/−50 | 57(S)/79(T) | CM |

Some important cavity parameters are listed in Table 5.1. All samples used were uncoated and inclined under Brewster's angle. The main pump source applied in this work was a tunable narrowband (~ 1 nm) Ti:sapphire laser (modified CW Tsunami, Spectra-Physics) which delivered maximum output power up to ~ 3 W in the fundamental mode. The pump laser was tuned to match the absorption maximum of the different laser materials as indicated in Table 5.1 (cf. Chapter 2). In the study of Ho:YAG ceramics, a commercial Tm:fiber laser (IPG Photonics) was employed with an output power up to 5.2 W in the fundamental mode and a linewidth of 0.3 nm. In all cases the pump beam was focused by an $f = 70$ mm lens (L in Fig. 5.1).

The second beam waist required to increase the fluence on the SA, cf. Chapter 4, is created by the curved folding mirror $M_3$ (for reflection-type SAs which act as a plane end mirror) and by $M_3$ and an additional curved end mirror $M_4$ (Fig. 5.1) for transmission-type SAs which were also mounted under Brewster's angle. Mirrors with different RoC were available for optimization. The 3rd cavity waist occurs on the OC, see Fig. 5.2b.

Table 5.2 Laser characteristics and diagnostics equipment used.

| Characterized parameter | Equipment |
|---|---|
| Average output power $P_{out}$ | Power meter (TPM-300, Gentec) |
| Optical spectrum | Spectrum analyzer (waveScan, extended IR, APE GmbH) |
| RF spectrum | Fast InGaAs PIN photodiode (ET-50000, EOT Inc);<br>Spectrum analyzer (R&S FSP7, Rohde & Schwarz). |
| Pulse duration | Autocorrelator (pulseCheck, APE GmbH);<br>Home-made FROG |

The mode-locked 2 μm lasers were characterized in terms of average output power $P_{out}$, optical spectrum, RF spectrum and pulse duration $\tau_p$ (FWHM intensity). The equipment used is listed in Table 5.2. For sub-100 fs pulse durations, also a home-made Frequency Resolved Optical Gating (FROG) apparatus was applied, with a commercial Si-detector spectrometer (Ocean Optics USB4000).

## 5.2 Mode-locking of garnet ceramics

The basic features and advantages of laser ceramics as active media were outlined in Chapter 2 where also the spectroscopic characterization performed was presented. In the present work, three garnet ceramics were studied for the first time in mode-locked lasers for the generation of ultrashort pulses near 2 μm.

### 5.2.1 Tm:YAG ceramics

As discussed before, crystalline Tm:YAG lasers were one of the first 2 μm lasers to be mode-locked in the steady-state in 1991. Prior to this work passively mode-locked Tm:YAG

crystalline lasers had not been reported at all and Tm:YAG ceramics had never been employed in mode-locked lasers.

Two transparent YAG ceramics, doped with 4 and 10 at. % $Tm^{3+}$, were available for the present laser experiments. These ceramics were fabricated by solid-state reactive sintering of commercial α-$Al_2O_3$, $Y_2O_3$ and $Tm_2O_3$ powders using MgO powder and tetraethoxysilane (TEOS) to favor the sintering process, all with purity better than 99.99% [127]. Both ceramic active elements had a thickness of 3.2 mm and an aperture of 3.2×3.2 $mm^2$. For cooling, the ceramics were mounted in a Cu holder and wrapped in Indium foil to ensure good thermal contact with all the four lateral faces. The holder was cooled with water at 20°C. The Ti:sapphire laser pump beam was focused through the dichroic mirror $M_1$ which was highly transmitting at this wavelength. In a single pump pass, the 4 and 10 at. % Tm:YAG ceramics absorbed about 75% and 95% of the incident pump light, respectively, which agrees rather well with the calculated values using the cross-section data in Chapter 2 (77% and 97%, respectively) and no saturation of the absorption by the pump was observed.

OCs with transmission in the 0.5%-3.0% range at the laser wavelength were used in this experiment. The cavity scheme applied contained a prism pair for GDD compensation and a GaSb-based SESAM as a SA (cf. Table 5.1). The two $CaF_2$ Brewster prisms inserted produced a round-trip GDD between -500 and -3000 $fs^2$, depending on their separation. The negative GDD turned out to be essential for stabilizing the CWML. However, no significant variation of the pulse duration was observed in dependence on the GDD in the ps regime.

The known characteristics of the available GaSb-SESAMs were summarized in Table 3.1. Self-starting mode-locking was achieved with SESAMs No.2, No.3 and No.4 for both ceramic samples. For SESAM No.1, a strong tendency of QSML was observed leading to damage of the SESAM. This can be attributed to the expected higher modulation depth $\Delta R$ with the 3-QW design, as discussed in Chapter 4. The laser characteristics in the CWML regime are summarized in Table 5.3. In all cases the output spectrum was centered near 2.01 μm. With a prism separation of ~ 15 cm the repetition rate of the laser was ~ 99 MHz.

Table 5.3 Comparison of the mode-locked Tm:YAG ceramic laser performance with different GaSb-SESAMs and 3.0% OC. $\Delta\lambda$ corresponds to the FWHM and $P_{out}$ denotes the average output power.

| SESAM | 4 at. % Tm | | | | 10 at. % Tm | | | |
|---|---|---|---|---|---|---|---|---|
| | $\tau_p$ [ps] | $\Delta\lambda$ [nm] | TBP | $P_{out}$ [mW] | $\tau_p$ [ps] | $\Delta\lambda$ [nm] | TBP | $P_{out}$ [mW] |
| No.1 | NA, damage occurs | | | | | | | |
| No.2 | 3.2 | 2.17 | 0.514 | 140 | 3.3 | 2.52 | 0.616 | 62 |
| No.3 | 3.0 | 2.56 | 0.569 | 135 | 3.3 | 2.55 | 0.623 | 39 |
| No.4 | 3.0 | 2.2 | 0.489 | 105 | 3.6 | 2.04 | 0.544 | 57 |

In general, the performance in terms of pulse duration was similar for SESAMs No.2, No.3 and No.4. The difference in output power is presumably due to the non-saturable losses

$\Delta R_{ns}$, unfortunately not precisely known for the SESAMs used. The two different ceramic samples produced similar laser characteristics such as wavelength, duration, bandwidth, and TBP; only $P_{out}$ was lower for the higher doping, by a factor of ~ 2. The latter is most likely related to the increased reabsorption. However, the wavelength shifted by only 1 nm for the increased doping, from 2.011 to 2.012 µm.

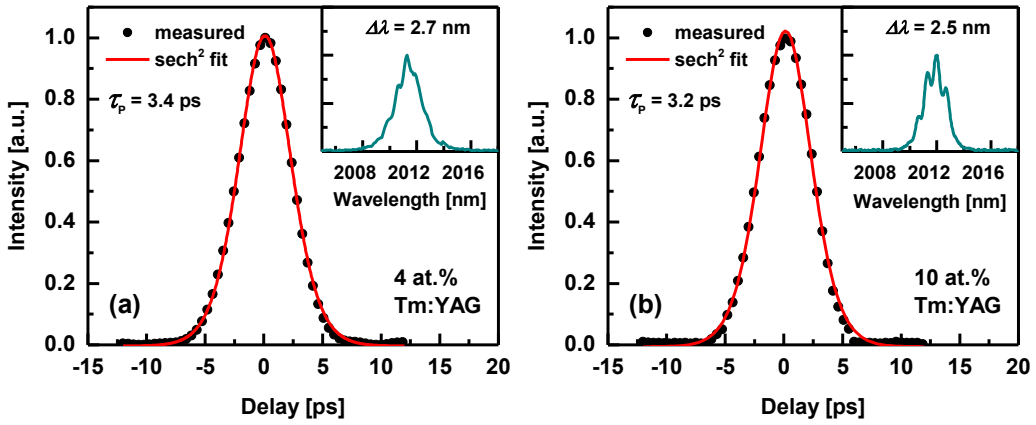


Fig. 5.3 Recorded AC-traces (black symbols) and fits (red lines) assuming a sech$^2$-pulse shape of the mode-locked Tm:YAG ceramic laser with SESAM No.4 and the corresponding optical spectra (insets): (a) 4 at. % Tm:YAG ceramics with 0.5% OC and (b) 10 at. % Tm:YAG ceramics with 1.5% OC.

Intensity autocorrelation (AC) traces recorded for the 4 and 10 at. % Tm:YAG ceramics with SESAM No.4 are shown in Fig. 5.3 for comparison. Lower out-coupling leads to lower overall losses and from theoretical point of view to shorter pulse durations [100]. However, in this experiment the pulse duration did not show a clear dependence on the OC transmission. For the relatively low out-coupling studied, increasing the transmission of the OC, only $P_{out}$ increased proportionally, e.g., for SESAM No.2 and the 4 at. % Tm:YAG, $P_{out}$ increased from ~ 40 mW for 0.5% OC to ~ 150 mW for 3.0% OC.

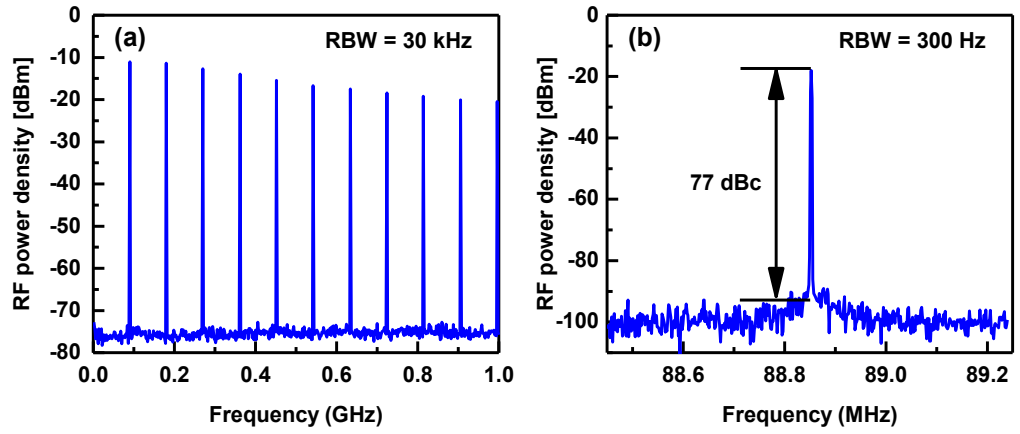


Fig. 5.4 RF spectra of the mode-locked 4 at. % Tm:YAG ceramic laser with the 0.5% OC: (a) 1.0 GHz wide span, (b) fundamental beat note in a 800 kHz wide span. RBW: resolution bandwidth.

As a further evidence for stable single-pulse CWML without Q-switching instabilities, the RF spectra were recorded, shown for the 4 at. % Tm:YAG ceramics in Fig. 5.4. Despite the slight drop of the harmonic beat notes in Fig. 5.4a, no peaks were observed in between. The fundamental beat note at 88.83 MHz displays a remarkably high extinction ratio of 77 dB above carrier, as shown in Fig. 5.4b, and no side bands related to Q-switching are seen.

After the publication of the above results [128], other researchers reported mode-locking of diode-pumped Tm:YAG ceramics using graphene-SAs [129]. Their best results were similar both in terms of shortest pulse duration ($\tau_p$ = 2.8 ps at 2.016 µm) and maximum average power ($P_{out}$ = 158 mW at 98.7 MHz).

### 5.2.2 Tm:LuAG ceramics

Tm:LuAG ceramics had not been employed before the present work in mode-locked lasers. However, one report on crystalline Tm:LuAG laser mode-locked by GaAs-based SESAMs was published very recently: With diode pumping this laser generated 38 ps pulses at ~ 2.023 µm with $P_{out}$ = 1.2 W at 129.2 MHz [130].

A 4 at. % Tm:LuAG ceramics was available for the present study, fabricated by the same procedure as Tm:YAG. The 3 mm thick active element had an aperture of ~ 5×5 mm$^2$. It was mounted in a similar way in the same cavity as the one used for the Tm:YAG ceramics. The single-pass average absorption of the pump light was ~ 71 %, in good agreement with the calculated 72% (cf. Fig. 2.5). No roll-off in the input-output power dependence in CW operation (prism pair removed and SESAM substituted by a plane 100% reflecting mirror) was observed up to the maximum pump level applied for OC transmission in the 0.5-5% range, which is an indication of the high quality of the ceramic.

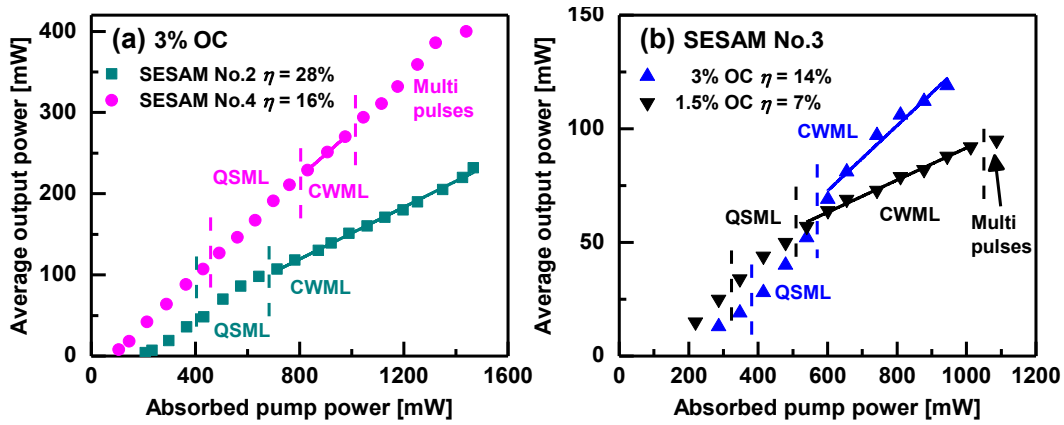


Fig. 5.5 Average output power versus absorbed pump power of the mode-locked Tm:LuAG ceramic laser using different SESAMs with the 3.0% OC (a) and using different OCs with SESAM No.3. $\eta$ is slope efficiency versus absorbed pump power in the CWML regime (linear fit).

For mode-locking, the same batch of GaSb-based SESAMs was tested. However, the mode size on the SESAM had to be increased to prevent damage although this contradicts the CWML criterion discussed in Chapter 4. By applying an $M_3$ with a RoC of −150 mm (the

largest available), a waist radius at the SESAM position of ~ 100 µm (calculated value) was achieved (cf. Table 5.1). As expected, the central wavelength of the Tm:LuAG ceramic laser was slightly longer, around 2.022 µm. With a prism separation of 21 cm the repetition rate was ~ 93 MHz.

The input-output power dependences are compared in Fig. 5.5 for different SESAMs and OCs and the laser characteristics are summarized in Table 5.4. Initially, SESAM No.3 was tested and the pulse duration got shorter, from $\tau_p$ = 3.8 to 3.0 ps, as the cavity losses were reduced by the OC, however, the slope efficiency also dropped to 7%. Moreover, multi-pulse operation occurred as $P_{out}$ reached 95 mW for the 1.5% OC.

Figure 5.6a shows the intensity AC trace recorded in such a multi-pulse (4 pulses) regime resulting in 7 peaks. The situation was greatly improved with the 3% OC, as can be seen from Fig. 5.6b.

It shall be noted that with the 1.5% OC, damage to the SESAM No.3 occurred in the QSML region in Fig. 5.5. Due to this reason, the 3.0% OC was employed for comparison of the different SESAMs in the stable CWML regime.

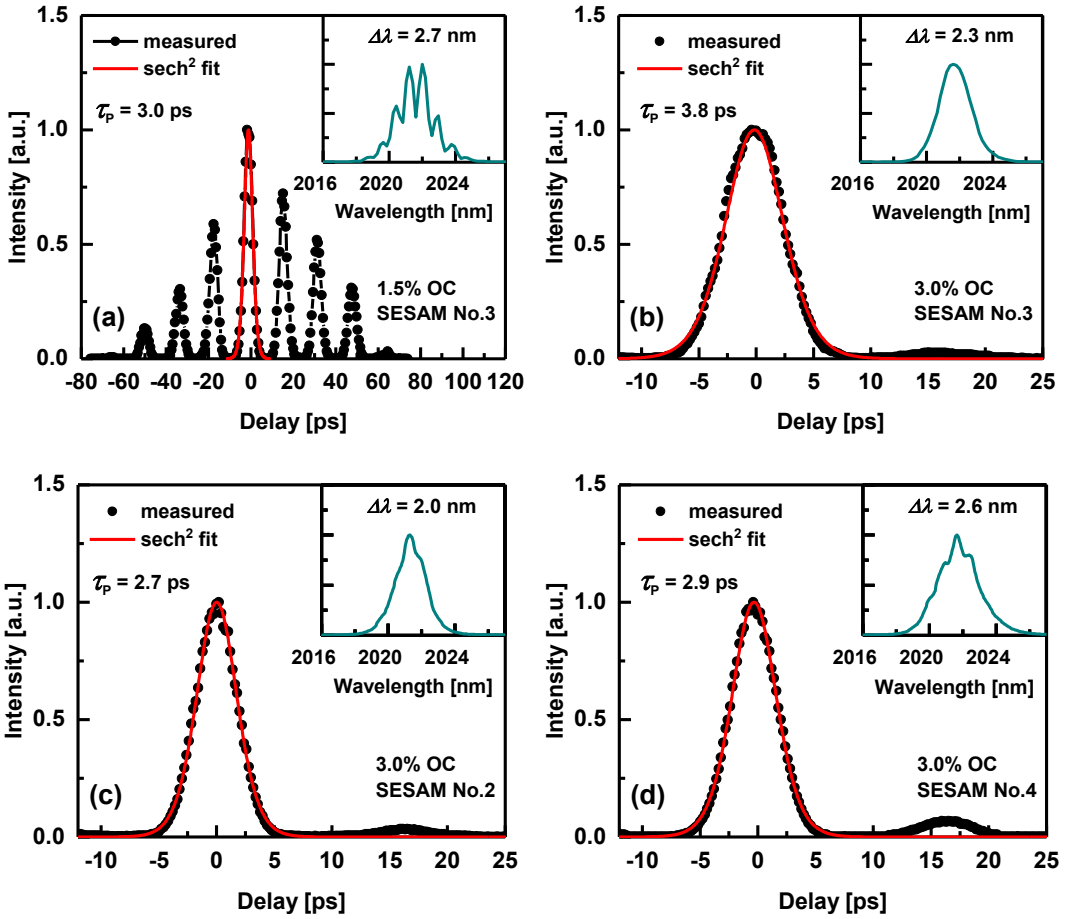


Fig. 5.6 Measured AC traces (black symbols) and fits (red lines) assuming a sech$^2$-pulse shape of the mode-locked Tm:LuAG ceramic laser with (a) SESAM No.3 and 1.5% OC; (b) SESAM No.3 and 3.0% OC; (c) SESAM No.2 and 3.0% OC; (d) SESAM No.4 and 3.0% OC. Insets: optical spectra.

Self-starting CWML operation was achieved with SESAMs No.2, No.3, and No.4 easily, without damage. Depending on the SESAM parameters, the mode-locked laser undergoes different operation regimes in the applied pump power range (CW, QSML, CWML, multi-pulses), as shown in Fig. 5.5. The AC traces and spectra can be compared in Figs. 5.6b-d. As could be expected, implementing the SESAM with the highest modulation depth $\Delta R$ (SESAM No.1 with 3 QWs), only led to strong tendency of Q-switching instabilities and optical damage.

Table 5.4 Comparison of the mode-locked Tm:LuAG ceramic laser performance with different GaSb-based SESAMs and OCs. $\Delta\lambda$ corresponds to the FWHM, $P_{out}$ is the average output power, and $F_{th}$ is the (spatially) averaged fluence on the SESAM at the CWML threshold.

| SESAM | OC | $\tau_p$ [ps] | $\Delta\lambda$ [nm] | TBP | $P_{out}$ [mW] | $F_{th}$ [μJ/cm$^2$] |
|---|---|---|---|---|---|---|
| No.1 | NA, damage occurs | | | | | |
| No.2 | 3.0% | 2.7 | 2.0 | 0.40 | 232 | 100 |
| No.3 | 3.0% | 3.8 | 2.3 | 0.64 | 119 | 65 |
| | 1.5% | 3.0 | 2.7 | 0.60 | 95* | |
| No.4 | 3.0% | 2.9 | 2.6 | 0.55 | 270<br>400* | 218 |

*limit when multi-pulses occur

Also in the case of Tm:LuAG ceramics it was essential to have the intracavity prism pair (with calculated round trip GDD of −2020 fs$^2$) for ultimate stability. However, again the prisms had no pulse shortening effect.

The performance of SESAM No.2 was the best in terms of CWML operation range, extending from 700 mW up to the maximum absorbed pump power, cf. Fig. 5.5a. Pulses as short as 2.7 ps were obtained with $P_{out}$ = 232 mW. A satellite pulse was observed at a separation of 16 ps (the same as for the multi-pulses discussed before), with an amplitude of only 3% of the main pulse. It can be seen together with the corresponding slight spectral modulation in Fig. 5.6c. The TBP amounted to 0.40 in this case.

Using SESAM No.3, CWML started from an absorbed power of ~ 600 mW, with a slope efficiency of 14%. A maximum $P_{out}$ = 119 mW was reached for CWML. The corresponding AC trace and optical spectrum are presented in Fig. 5.5b. The satellite amplitude was ~ 2% of the main pulse and the TBP amounted to 0.64.

Best performance with respect to $P_{out}$ (270 mW) and slope efficiency ($\eta$=28%) was obtained with SESAM No.4. However, compared to SESAM No.3, CWML started at a rather high average intracavity fluence on the SESAM of $F_{th}$ = 218 μJ/cm$^2$ and the stability range was narrower in terms of absorbed pump power, Fig. 5.5a. The pulses were shorter, $\tau_p$ = 2.9 ps, compared to SESAM No.3 but the amplitude of the satellite increased to about 7% of the main pulse at the same separation, cf. Fig. 5.6d. This led to more pronounced modulation

in the spectrum. The corresponding TBP = 0.55 is slightly closer to the Fourier limit compared to SESAM No.3. When $P_{out}$ exceeded the CWML limit, multi-pulse operation was observed in this case, too.

It shall be noted that the satellite separation from the main pulse was exactly 16 ps in all cases. This matches rather well the round trip time of the entire SESAM structure taking into account the high refractive index ($n$ = 3.34) of GaSb. In other words, a part of the pulse energy incident upon the SESAM, is transmitted through the distributed Bragg reflector and retro-reflected from the rear surface of the GaSb substrate, leading to formation of the satellite pulse. This spurious Fabry–Pérot effect is also confirmed by the modulation of the emission spectra in Fig. 5.6 ($\Delta\lambda_{mod}$ = 0.8 nm), which correlates with the free-spectral range of the ~ 520 µm thick GaSb substrate. More pulses are expected at higher power as they are able to saturate the QWs being further amplified by the gain medium. However, the observed Fabry–Pérot effect in the SESAM structure does not limit the bandwidth of the mode-locked Tm:LuAG oscillator for the present pulse durations. This will become clear in the following where shorter pulses will be reported with the same SESAMs using other active media. The spurious Fabry–Pérot effect could be easily suppressed in the future by adding a few more layer pairs to the distributed Bragg reflector and/or by further roughening the SESAM rear surface.

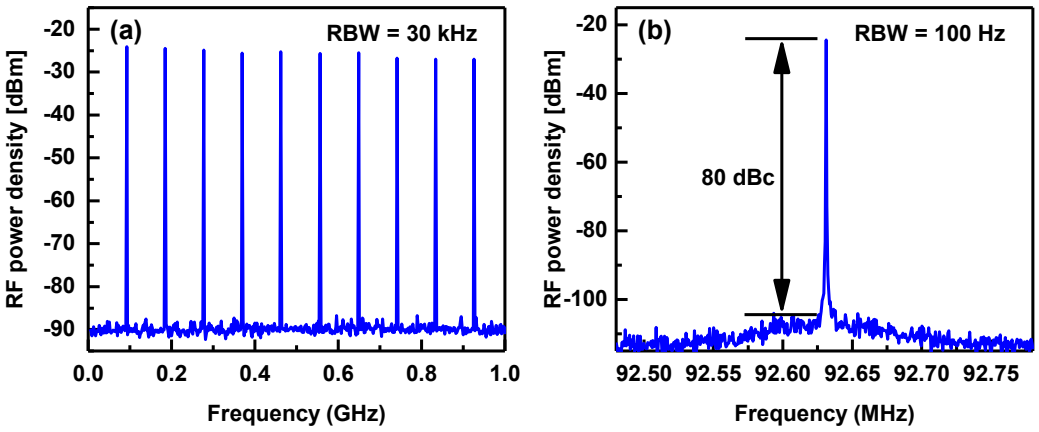


Fig. 5.7 RF spectra of the mode-locked Tm:LuAG ceramic laser: (a) 1.0 GHz wide-span, (b) fundamental beat note in a 300 kHz wide-span. RBW: resolution bandwidth.

Finally, the stability of the mode-locked Tm:LuAG ceramic laser was characterized by RF spectra and the results for SESAM No.2 are shown in Fig. 5.7. The narrow fundamental beat note was centered at 92.63 MHz with a very high extinction ratio of 80 dB above the noise level, cf. Fig. 5.7b. The RF spectra indicate again stable and clean CW mode-locking without Q-switching instabilities. Similar extinction ratios around 80 dB above the noise level were achieved when operating the Tm:LuAG laser in the CWML regime with SESAMs No.3 and No. 4. Compared to Tm:YAG (Fig. 5.4), the flat RF comb in Fig. 5.7a within the 1 GHz span and the higher extinction ratio indicate more stable operation of the mode-locked Tm:LuAG laser.

Compared to the so far only report on a Tm:LuAG crystalline laser mode-locked by a SESAM [130] , one order of magnitude shorter pulses and two orders of magnitude better pulse contrast are achieved in the present work. This is attributed to the faster relaxation time of the SESAM employed in the present work. With respect to the previously described performance of the mode-locked Tm:YAG ceramic laser [128], higher efficiency and output power are demonstrated at comparable pulse characteristics.

### 5.2.3 Tunable mode-locked Ho:YAG ceramic laser

As already mentioned, Ho:YAG lasers were the first 2 μm lasers which were actively mode-locked. Recently, also passive CWML with a Tm,Ho:YAG crystal pumped by a Ti:sapphire laser has been demonstrated [131]: with an InGaAs/AlAsSb QWs-based SESAM, pulses of $\tau_p$ = 60 ps were obtained at 2.091 μm for $P_{out}$ = 160 mW at 106.5 MHz, without GVD compensation. A similar laser with chirped mirrors for negative GDD was studied in [132] employing GaAs- and GaSb-based SESAMs. The latter turned out to me more promising delivering pulses as short as 21.3 ps at 2.091 μm for $P_{out}$ = 63 mW at ~ 107 MHz. The only CWML results reported for a singly Ho-doped YAG crystal/ceramics deal with active mode-locking by acousto-optic modulation: Pumping by a Tm:YLF laser, pulses as short as 102 ps at ~ 2.097 μm with $P_{out}$ = 1.04 W at ~ 83 MHz were obtained [133], and pumping with a Tm-fiber laser, the shortest pulse duration was $\tau_p$ = 241.5 ps at 2122 μm for $P_{out}$ = 1.84 mW at ~ 82 MHz [134].

In the present experiment, the Tm-fiber laser used for pumping emitted at 1.908 μm, very close to the absorption maximum of Ho:YAG (cf. Chapter 2) and within the FWHM of the peak. After the collimating optics, the beam had a diameter of 4.5 mm with a divergence angle of 0.57 mrad and an $M^2$ factor of 1.03. The calculated pump beam radius at the input facet of the Ho:YAG ceramic sample was 28 μm and the cavity was designed for a laser mode radius ~ 30 μm. The single-pass absorption amounted to only ~ 36±1%, because of the strong Fresnel reflection at Brewster's angle of the unpolarized pump light (its s-component).

The 1 at. % Ho:YAG ceramic sample, prepared by a similar fabrication process as the Tm:YAG/LuAG ceramics [135], had a thickness of 4 mm and an aperture of ~ 3×3 $mm^2$. In this experiment, the GaSb-based SESAM No.2 (without additional AR coating) was applied as a SA. The beam radius on the SESAM was adjusted for best CWML stability by the choice of $M_3$ (cf. Table 5.1). The laser was studied without intracavity GDD compensation and the repetition rate was 82-83 MHz.

Self-starting CWML operation was achieved with this laser for OCs with transmission of 0.5 and 1.5%. The results in terms of average output power and slope efficiency are shown in Fig. 5.8. In both cases the CWML regime starts at an intracavity power ~ 5.3 W. This corresponds to an average fluence of 420 μJ/$cm^2$ on the SESAM. As the pump power was increased, the laser directly switched from CW to CWML regime without any Q-switching instability, cf. Fig. 5.8. No QSML region existed and RF spectra as the one shown in Fig. 4.12 for illustration purposes were obtained only when the cavity was misaligned. This was mainly due to the one order of magnitude higher gain cross section $\sigma_g$ of Ho:YAG compared to the

Tm-doped garnets (cf. Figs. 2.6-2.8). The resulting lower gain saturation fluence $F_{\mathrm{sat,L}}$ stabilizes the laser against Q-switching instabilities, as discussed in Chapter 4.

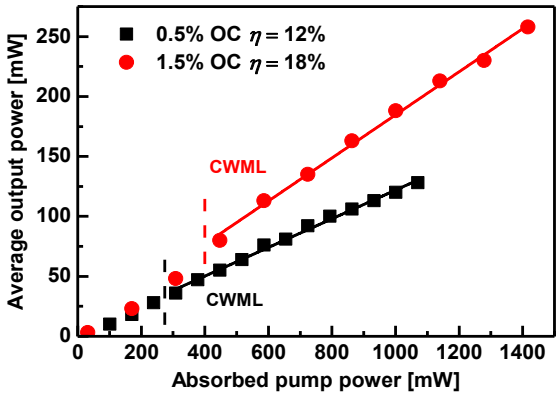


Fig. 5.8 Average output power versus absorbed pump power of the mode-locked Ho:YAG ceramic laser for different output couplers (OCs). The vertical lines indicate the transition from CW to clean CWML operation. $\eta$: slope efficiency obtained from linear fits.

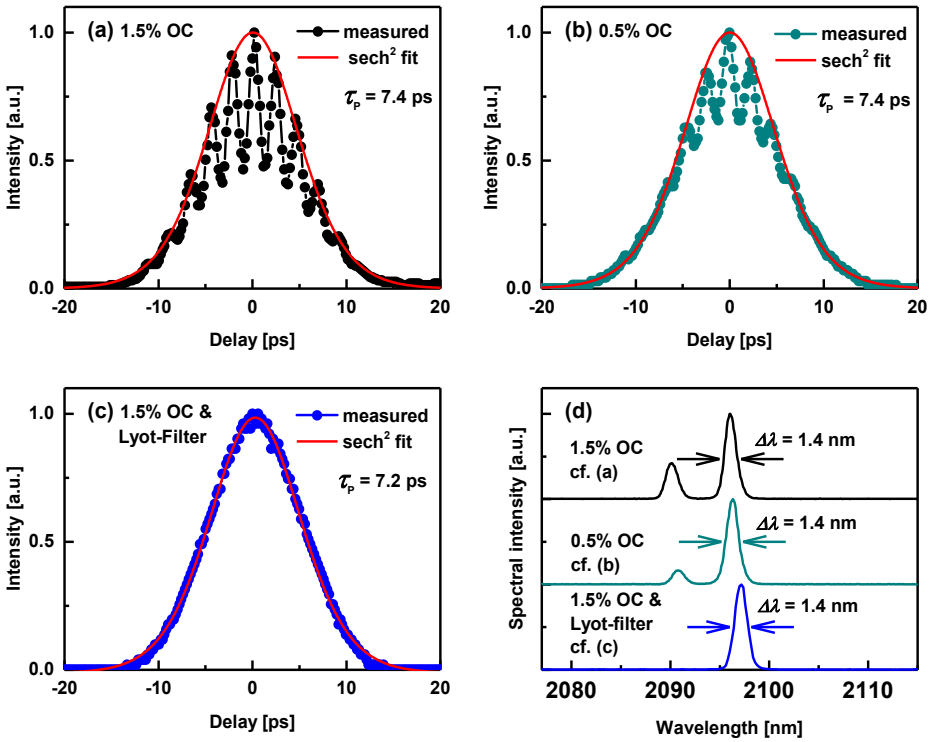


Fig. 5.9 SESAM mode-locked Ho:YAG ceramic laser: Measured AC traces (black symbols) and fits (red lines) assuming a sech$^2$-pulse shape without (a,b) and with the Lyot filter (c) in the cavity (OC: output coupler). (d) Optical emission spectra corresponding to (a), (b) and (c).

With the 1.5% OC, the mode-locked laser delivered a maximum $P_{\mathrm{out}}$ of 258 mW for 1.4 W of absorbed pump power, with a slope efficiency of 18%. The maximum absorbed pump power with the 0.5% OC was limited to 1.1 W ($P_{\mathrm{out}}$ 128 mW). Above this level, damage on the surface of the SESAM was observed. The damage threshold of this SESAM

was estimated from this to be about 2.0 mJ/cm$^2$ of on-axis fluence. As long as the laser was operated below this value, CWML was very stable and could be maintained without interruption during the entire day.

The AC traces and optical emission spectra of the mode-locked Ho:YAG ceramic laser are presented in Fig. 5.9 at maximum $P_{out}$. As in the CW regime (Fig. 5.10 gives only an idea of this because it was recorded with a wavelength tuning element), stable dual-wavelength emission centered at 2.090 and 2.096 µm occurred. Each peak exhibited a spectral width of $\Delta\lambda = 1.4$ nm for both 1.5% and 0.5% OCs (Fig. 5.9d). A pulse duration $\tau_p = 7.4$ ps was derived from the measured AC traces under the assumption of sech$^2$-pulse shapes (Figs. 5.9a and b). The AC traces are modulated with a frequency of 0.43 THz, which corresponds to the spectral difference of the two emission wavelengths (Fig. 5.9a and b). The depth of this modulation is related to the intensity ratio of the two peaks in Fig. 5.9d. The effect thus is reminiscent of the multi-pulse regime discussed in Chapter 4 but obviously cannot be qualified as pulse break-up because it occurs also in the CW regime. Dual emission of the same pair of wavelengths was reported for the SESAM mode-locked Tm,Ho:YAG laser in [132] but in contrast to the present measurements, no modulation of the AC trace was detected, most likely because of the much longer pulse durations. Thus, this behavior can be attributed to the nature of Ho:YAG and agrees with the calculated gain cross sections in Fig. 2.8.

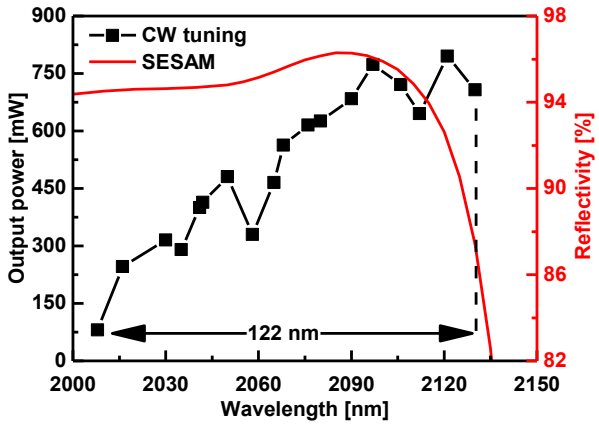


Fig. 5.10 Spectral tunability of the CW Ho:YAG ceramic laser obtained with a Lyot filter (1.5% OC) and reflectivity curve of the employed GaSb-based SESAM. The SESAM had been substituted by a plane mirror for the tunability measurement.

Such dual-wavelength CWML regimes were observed by other researchers in different spectral ranges and suggested as a promising approach for the generation of THz radiation or as synchronized sources for double-pulse pump-probe measurements [136-138]. In this work the synchronous dual-wavelength emission aspect was not further pursued since the main goal was the generation of non-modulated pulses with shortest durations. Two different methods were applied to suppress the dual-wavelength operation of the mode-locked Ho:YAG ceramic laser.

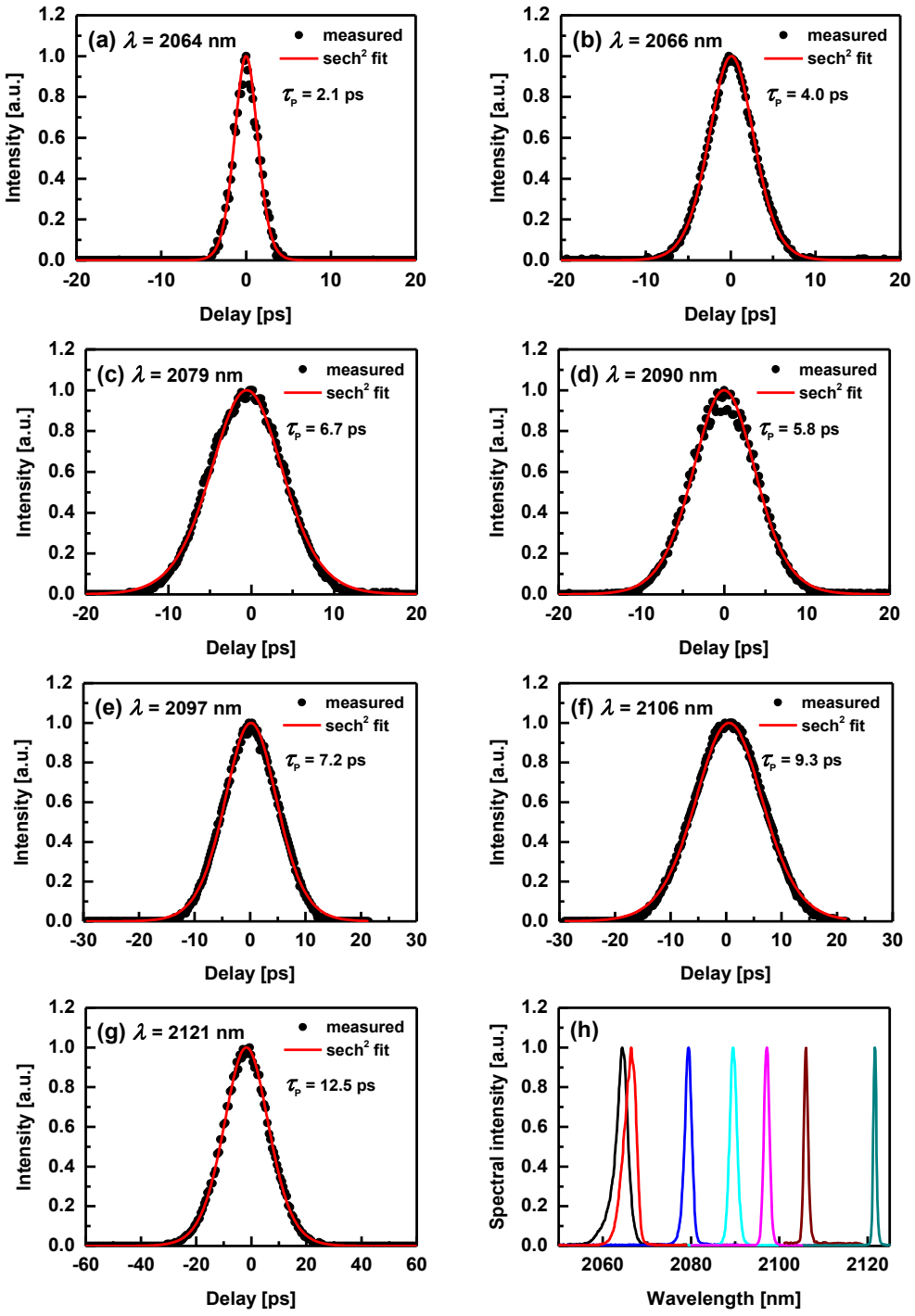


Fig. 5.11 Tuning of the mode-locked Ho:YAG laser with the 0.5% OC: (a)-(g) measured AC traces (black symbols) and fits (red lines) assuming a $\mathrm{sech}^2$-pulse shape and (h) optical emission spectra.

At first, the $CaF_2$ prism pair was inserted together with a knife edge in the cavity arm containing the OC. Neither the targeted single-wavelength emission nor a significant pulse shortening were achieved despite the large amount of GDD (up to −1700 $fs^2$). Thus the prism pair was removed.

Then a birefringent (Lyot) filter was inserted instead of the prism pair. In this configuration the dual-wavelength emission was eliminated and clean pulses without modulation were generated at 2.096-2.097 μm, as shown in Figs. 5.11e and 5.12f. The non-modulated pulses are slightly shorter (7.2 ps) and the TBP amounts to 0.69.

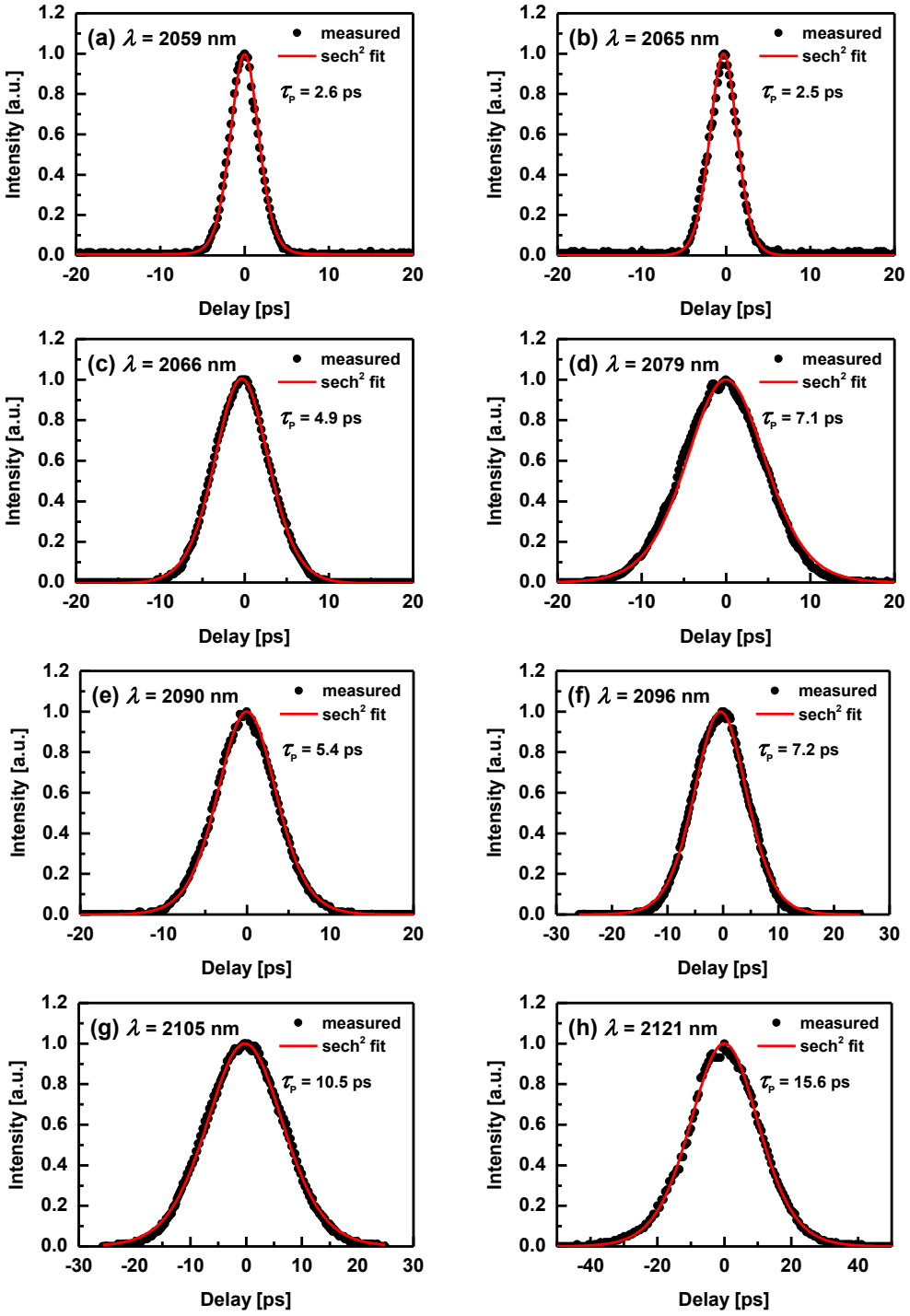


Fig. 5.12 Tuning of the mode-locked Ho:YAG laser with the 1.5% OC: (a)-(h) measured AC traces (black symbols) and fits (red lines) assuming a $\mathrm{sech}^2$-pulse shape.

Prompted by the broad CW lasing tunability achieved (122 nm) of the Ho:YAG ceramic laser and the broad reflection band of the GaSb-based SESAM shown in Fig. 5.10, the same Lyot filter was employed to study the tunability in the CWML regime. The Lyot filter was a 3-mm thick quartz plate with the optical axis at 60° to the surface, a special design which does not substantially restrict the bandwidth to suppress fs pulse generation [126].

Tunable CWML was achieved with both the 0.5% and 1.5% OCs. The AC traces and the corresponding optical emission spectra are shown in Fig. 5.11 for the 0.5% OC and in Fig. 5.12 for the 1.5% OC. The achieved tunability is demonstrated in Fig. 5.11h for the former and in Fig. 5.13 for the latter case.

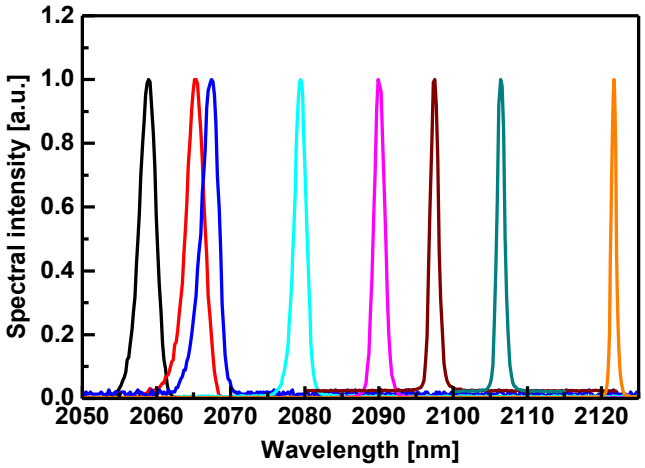


Fig. 5.13 Optical emission spectra of the tunable mode-locked Ho:YAG laser with the 1.5% OC.

The pulse duration and $P_{out}$ dependences of the tunable mode-locked Ho:YAG laser are illustrated in Fig. 5.14 and all important parameters are compiled in Table 5.5.

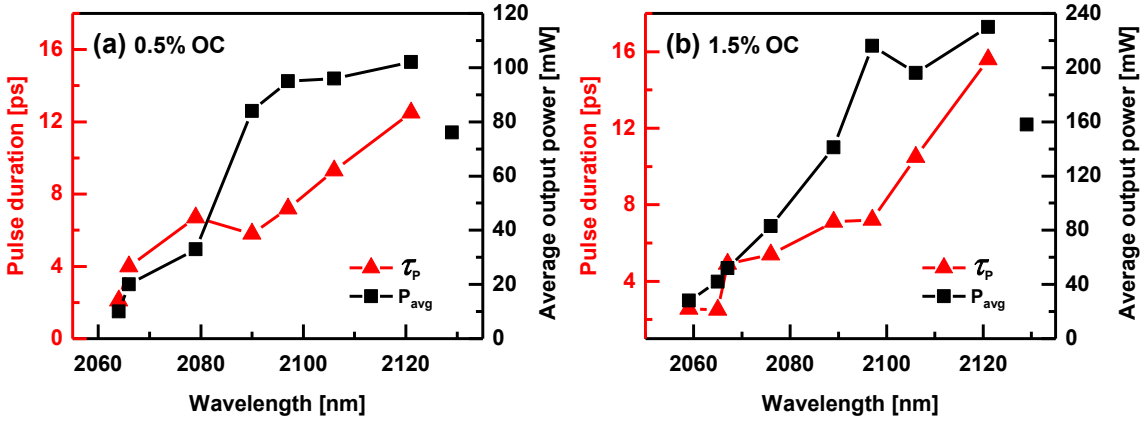


Fig. 5.14 Spectral tunability of the mode-locked Ho:YAG ceramic laser with a Lyot filter in the cavity: Pulse duration and average output power obtained with the 0.5% (a) and 1.5% (b) OCs.

With the 0.5% OC, tuning in the CWML regime was possible from 2.064 to 2.121 µm, leading to a total tuning range of 57 nm. The laser was still pulsing up to 2.129 µm but no

stable mode-locking was achievable. This is attributed to the abrupt drop in the SESAM reflectivity above ~ 2.120 μm (Fig. 5.10). The pulse duration decreased from 12.5 ps at 2.121 μm to 2.1 ps at 2.064 μm and $P_{out}$ reached 102 mW at 2.121 μm. The pulse shortening towards shorter wavelengths could be related to an increase of the modulation depth of the SESAM since it was originally designed for 2.040 μm. The shortest pulse duration of 2.1 ps was obtained at 2.064 μm for $P_{out}$ = 10 mW.

Table 5.5 Summary of the tunable mode-locked Ho:YAG ceramic laser output characteristics.

| 0.5% OC at 1.07 W absorbed pump power | | | | | | | | | |
|---|---|---|---|---|---|---|---|---|---|
| $\lambda$ [nm] | 2129 | 2121 | 2106 | 2097 | 2090 | 2079 | 2066 | 2064 | 2059 |
| $P_{out}$ [mW] | 76 | 102 | 96 | 95 | 84 | 33 | 20 | 10 | |
| $\tau_p$ [ps] | | 12.5 | 9.3 | 7.2 | 5.8 | 6.7 | 4 | 2.1 | NA |
| $\Delta\lambda$ [nm] | N/A | 0.8 | 1.2 | 1.4 | 1.8 | 1.9 | 3.1 | 3 | |
| TBP | | 0.67 | 0.75 | 0.69 | 0.71 | 0.88 | 0.87 | 0.44 | |
| 1.5% OC at 1.55 W absorbed pump power | | | | | | | | | |
| $\lambda$ [nm] | 2129 | 2121 | 2106 | 2097 | 2089 | 2076 | 2067 | 2065 | 2059 |
| $P_{out}$ [mW] | 158 | 230 | 196 | 216 | 141 | 83 | 52 | 42 | 28 |
| $\tau_p$ [ps] | | 15.6 | 10.5 | 7.2 | 5.4 | 7.1 | 4.9 | 2.5 | 2.6 |
| $\Delta\lambda$ [nm] | N/A | 0.8 | 1.2 | 1.3 | 1.7 | 1.8 | 2.5 | 2.9 | 2.6 |
| TBP | | 0.83 | 0.85 | 0.64 | 0.63 | 0.89 | 0.86 | 0.51 | 0.47 |

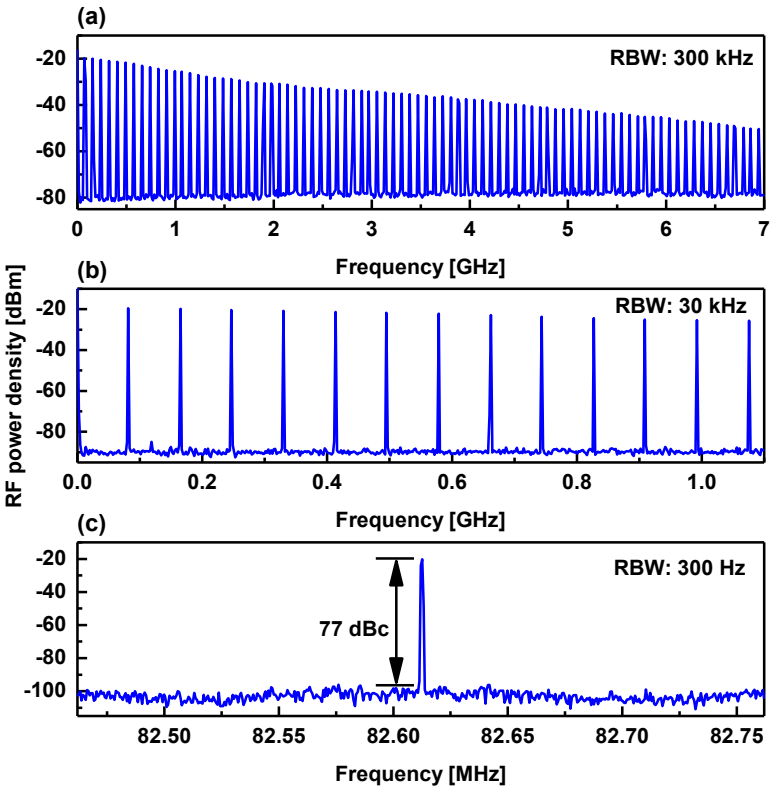


Fig. 5.15 RF spectra of the mode-locked Ho:YAG ceramic laser with the 0.5% OC: (a) 7 GHz and (b) 1.1 GHz wide-span, (c) fundamental beat note in a 300 kHz wide-span. RBW: resolution bandwidth.

With the 1.5% OC, tuning in the CWML regime was possible from 2.059 to 2.121 µm. The tuning range was slightly broader (by 5 nm) compared to the 0.5% OC. In general, the pulses were slightly longer compared to the results with the 0.5% OC: Their duration decreased from 15.6 ps at 2.121 µm to 2.5-2.6 ps in the short wavelength limit and $P_{out}$ reached 230 mW at 2.121 µm. The TBP in Table 5.5 varies from 0.44 to 0.89 which is almost 3 times the Fourier limit. Insertion of the $CaF_2$ prism pair did not result in further pulse shortening to utilize the available spectral bandwidth, just as without the birefringent filter.

The stability of the SESAM mode-locked Ho:YAG ceramic laser operating with the Lyot filter but without the prism pair at 2.097 µm is demonstrated in Fig. 5.15 in terms of RF spectra recorded in different spans. The narrowband fundamental beat note at 82.6 MHz exhibits a high extinction ratio of 78 dB above noise level (Fig. 5.15c). The RF spectra indicate clean CWML without Q-switching instabilities or any multi-pulse behavior. Note that the laser could be continuously tuned during operation without interruption of the CWML regime.

## 5.3 Sub-ps Tm:CALGO laser

Despite the broad and smooth gain cross-sections of Tm:CALGO and Tm:CALYO crystals which, as explained in Chapter 2 (cf. Fig. 2.11), make them potentially interesting for the generation of ultrashort pulses near 2 µm, only tens of picoseconds pulse durations are found in the literature: In 2015, passive mode-locking of Tm:CALGO was first reported using a commercial GaAs-based SESAM. The shortest pulse durations were 27 ps at 1949.5 nm, with $P_{out}$ = 330 mW at ~ 129 MHz [139]. Employing the same SESAM, also dual-wavelength (1.9589 and 1.9606 µm) CWML of Tm:CALYO was reported [138]: In this case the pulses were even longer, ~ 35 ps for $P_{out}$ = 830 mW at ~ 145 MHz.

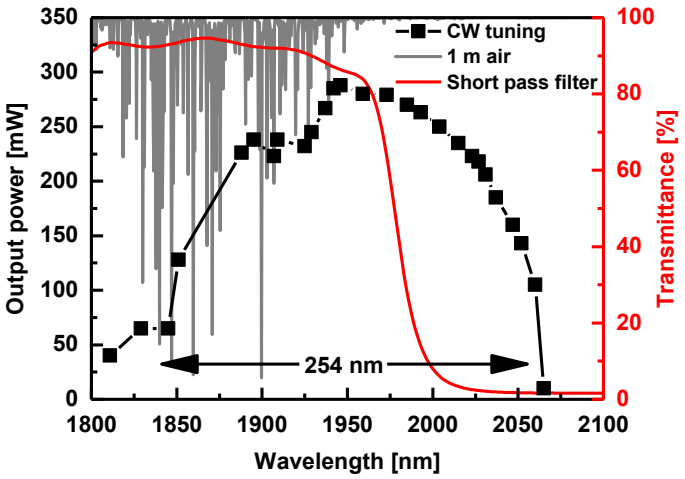


Fig. 5.16 Spectral tunability of the CW Tm:CALGO laser obtained with a Lyot filter (1.5% OC) and transmittance of the applied short pass filter. The grey line represents calculated transmittance of 1 m air from HITRAN database.

Most of the femtosecond mode-locked bulk lasers reported before operated above 2 µm [123, 124]. This is related to the strong water absorption in air below 1.95 µm (cf. Fig. 5.16), which will introduce unstable losses (depending on the humidity) in the cavity beam path and preclude spectral broadening as a prerequisite for pulse shortening towards sub-ps durations. In addition strong dispersion is expected in the presence of sharp absorption lines. As shown in Fig. 2.11, the gain maximum of Tm:CALGO is below 2 µm. This was experimentally confirmed by the CW tuning range recorded with the same X-shaped cavity shown in Fig. 5.16 without GDD compensation and the SESAM substituted by a plane total reflector: The Lyot filter permitted CW tuning across 254 nm with maximum $P_{out}$ near 1.946 µm. Thus the picosecond pulse regime obtained by other researchers was not surprising. To overcome this limitation, a special short pass filter was adapted in the present work as an OC. As shown in Fig. 5.16, the transmittance of this short pass filter increased sharply below 2 µm, introducing huge losses at shorter wavelengths which forced the laser to operate above 2 µm.

The 6 at. % (in the melt) Tm:CALGO crystal employed was grown by the Cz method and provided by the research team of [46]. The active element was processed as a 3.8 mm long Brewster rhomb with an aperture of ~ 4×4 mm$^2$ designed for σ-polarization due to the higher gain cross section (Fig. 2.11). The Ti:sapphire pump wavelength was tuned to 798 nm to match the absorption maximum for σ-polarization, cf. Table 5.1. The measured absorption amounted to 65.5%, in reasonable agreement with the calculated 72.8 % (cf. Fig. 2.10a). It did not change with the pump level or under lasing conditions.

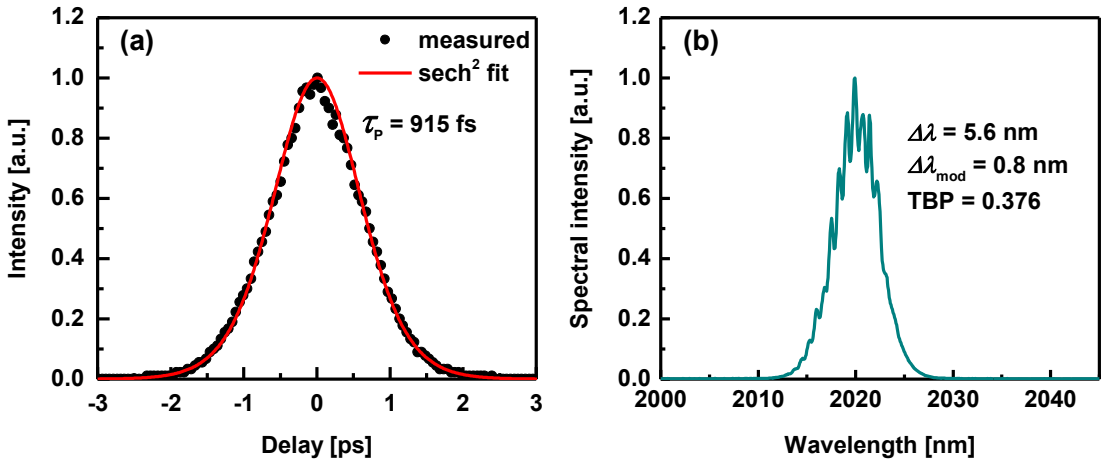


Fig. 5.17 Tm:CALGO laser mode-locked by the GaSb-based SESAM No.2 without GDD compensation: (a) measured AC trace (black symbols) and fit (red line) assuming a sech$^2$-pulse shape, and (b) optical emission spectrum.

Mode-locking of the Tm:CALGO laser was studied with the GaSb-based SESAMs No.2-5 from Table 3.1. For initial tests, no GDD compensation was applied in the laser cavity and the repetition rate was 102 MHz. Best performance in terms of stability, damage resistivity and pulse duration was achieved with SESAM No.2. At the oscillating wavelength of 2.020 µm the transmission of the OC amounted to 2.8%. The pulse duration was $\tau_p$ = 915 fs, cf. Fig. 5.17a. With a spectral width of 5.6 nm one arrives at TBP = 0.376. Slight spectral modulation

can be seen in Fig. 5.17b. It should have the same origin (parasitic Fabry-Perot effect) as in the mode-locked Tm:LuAG laser (cf. Fig. 5.6) since the period was again $\Delta\lambda_{mod} = 0.8$ nm.

With SESAMs No.3 and No.4, the tendency towards multi-pulse operation was stronger. This is probably due to the 1-QW structures which exhibit the lowest modulation depths. Single QWs are expected to be saturated more easily and thus further pulses, as those resulting from the Fabry-Perot effect will be favored. Still, it was possible to measure the pulse durations: $\tau_p = 1.6$ ps for SESAM Nr.3 and $\tau_p = 1.0$ ps for SESAM Nr.4.

Applying SESAM No.5 in which the QWs were relatively far from the surface, a pulse duration of $\tau_p = 7$ ps was measured. Thus thinner cap layer seems to play an important role for shortening the SA recovery time which affects the mode-locked laser pulse duration. The results can be compared with the performance of the commercial GaAs-based SESAM (BATOP GmbH) described in [4]. The relaxation time $\tau_2$ for this SESAM was specified as 34 ps while the obtained pulse duration for stable steady-state CWML was $\tau_p = 27$ ps.

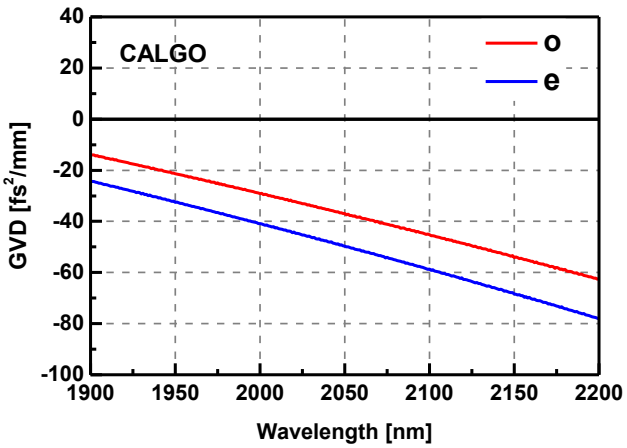


Fig. 5.18 Calculated GVD of CALGO near 2 µm (single-pass).

SESAM No.2 (cf. Table 3.1) was selected for further study and the $CaF_2$ prism pair was inserted into the cavity as a next step, see Fig. 5.1. The GVD versus wavelength, calculated with the new Sellmeier equations of CALGO fitted in [140], is shown in Fig. 5.18. The value for o-polarization at 2.020 µm is close to zero (−32.2 fs²/mm). The prism separation was optimized and at about 15 cm, the shortest pulses with ultimate stability were observed. The calculated contributions of the prism pair are both negative, as explained in Chapter 4. With the values from Table 4.2 which apply for a single pass, the round-trip GDD calculated for the above prism separation and a material path of 4 mm is −632 fs². The SESAM contribution was assumed to be −300 fs² from simulations [88], giving a total round-trip GDD ~ −1200 fs².

Figure 5.19 shows the input-output mode-locked laser characteristics with SESAM No.2 and the prism pair. Stable and self-starting mode-locking was achieved starting from $P_{out}$ = 18 mW. The calculated beam waist radius at the position of the SESAM was 70 µm, resulting in an average fluence of 78 µJ/cm² at the CWML threshold. The maximum output power reached $P_{out}$ = 58 mW at ~ 101 MHz. The relatively low slope efficiency in the CWML regime ($\eta$ = 8.8%) is related to the decreasing gain at wavelengths above 2 µm.

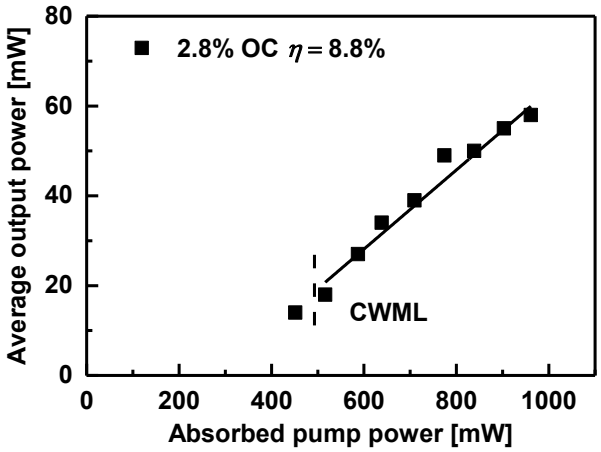


Fig. 5.19 Average output power versus absorbed pump power for the mode-locked Tm:CALGO laser. The vertical dashed line indicates the transition from CW to clean CWML operation.

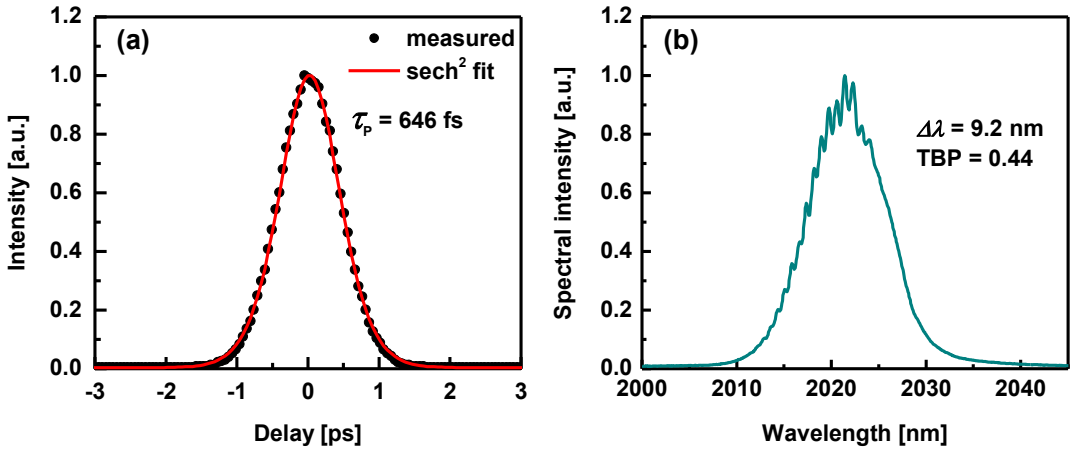


Fig. 5.20 Tm:CALGO laser mode-locked by the GaSb-based SESAM No.2 with GVD compensation: (a) measured AC trace (black symbols) and fit (red line) assuming a sech$^2$-pulse shape, and (b) optical emission spectrum.

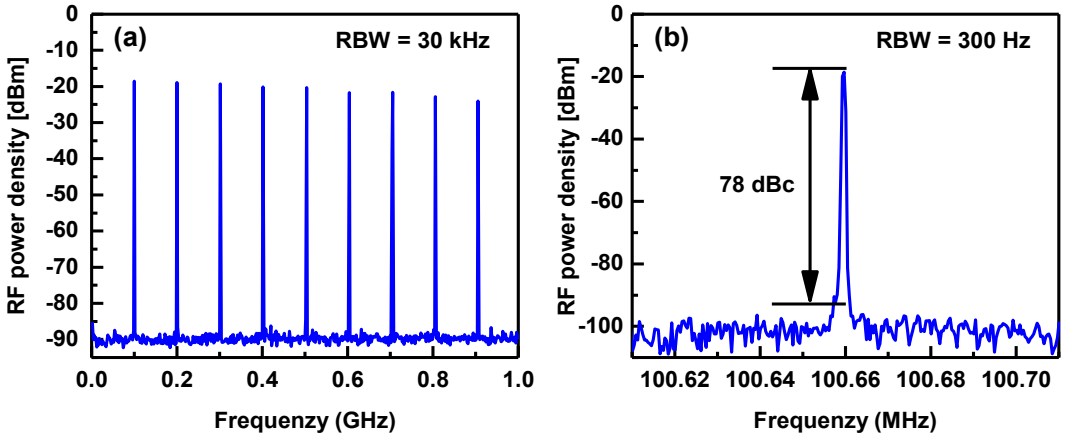


Fig. 5.21 RF spectra of the mode-locked Tm:CALGO laser: (a) 1 GHz wide-span, (b) fundamental beat note in a 100 kHz wide-span. RBW: resolution bandwidth.

The pulse duration decreased with increasing pump level: from $\tau_p \sim 750$ fs at the CWML threshold down to $\tau_p = 646$ fs at the maximum output power, as shown in Fig. 5.19a. The central wavelength was 2.021 μm. The TBP of 0.44 (Fig. 5.20b) is just 1/3 above the Fourier limit which leaves little room for pulse compression. Due to the rather low magnitude of the negative round-trip GDD, it is most likely that the soliton shaping mechanism was weak. This conclusion seems supported by the fact that in the CWML power range the soliton "area theorem" as described in Chapter 4 was not fulfilled.

However, the negative GDD of the prism pair was essential to achieve stable CWML and improve the signal-to-noise ratio in the RF spectra (cf. Fig. 5.21). Both records indicate clean CWML without Q-switching instabilities. The fundamental beat-note was 78 dB above noise level which is much better compared with the situation without the prism pair in the cavity.

## 5.4 Femtosecond Tm:MgW laser

The spectroscopic properties of the new monoclinic Tm:MgW crystal were presented in Chapter 2. Laser operation in the CW and passively Q-switched regime was achieved only very recently, in 2017 [52, 141], but these results are outside the scope of the present thesis and will not be presented here. The work on passive mode-locking was started in fact simultaneously. It was triggered not only by the calculated broad and smooth gain spectra, cf. Fig. 2.17, but also by the expected natural selection of wavelengths above 2 μm. Thus, a more systematic study was devoted to this unique laser material to which exclusive access was granted by the crystal growers.

The uncoated sample of Tm:MgW available for the mode-locked laser experiments was manufactured from the same 0.89 at. % doped as-grown material used for spectroscopic purposes, cf. Chapter 2. It was rectangular in shape, 3 mm thick along the *X*-axis, with an aperture of 4(*Y*)×3.5(*Z*) mm$^2$. Mode-locking was first investigated applying the GaSb-based SESAMs for the two possible polarization configurations with the sample inclined under Brewster's angle. The Ti:sapphire pump laser was tuned to 796 nm (maximum absorption for E||*Y* and very close to the maximum for E||*Z*, cf. Fig. 2.16a and Table 5.1). Then SWCNT-SAs were applied with a prism pair or chirped mirrors for GDD compensation. Finally, mode locking was studied also with graphene-SAs and chirped mirrors for GDD compensation.

### 5.4.1 SESAM mode-locked Tm:MgW laser

Initially, the Tm:MgW sample was oriented for the *E*||*Z* polarization (both pump at 802 nm and laser) and SESAM No.2 was employed without GDD compensation in a ~ 1.43 m long cavity. With the 1.5% OC, the free running laser wavelength was below 2 μm and the spectrum was affected by air absorption. A strong tendency of multi-wavelength emission was observed (cf. Fig. 5.22) which most likely was associated with mode-locking, however, the spectra were very unstable (cf. Fig. 5.22), with several well defined dips whose position coincided with the air absorption lines. This precluded stable CWML and further characterization. Other SESAMs or GDD compensation did not improve the situation. On the

other hand, as could be expected, tuning of the laser with the Lyot filter to wavelengths beyond 2 μm led to stable mode-locking but the pulse durations were of the order of few ps.

For E||*Y* polarization, stable and self-starting CWML was achieved with SESAM No.3 which contained a single QW and a 10 nm thick cap layer, without GDD compensation. Without the Lyot filter, the naturally selected laser wavelength was ~2.021 μm. At an incident pump power of 1.86 W (absorbed pump power 0.80 W), $P_{out}$ reached 30 mW.

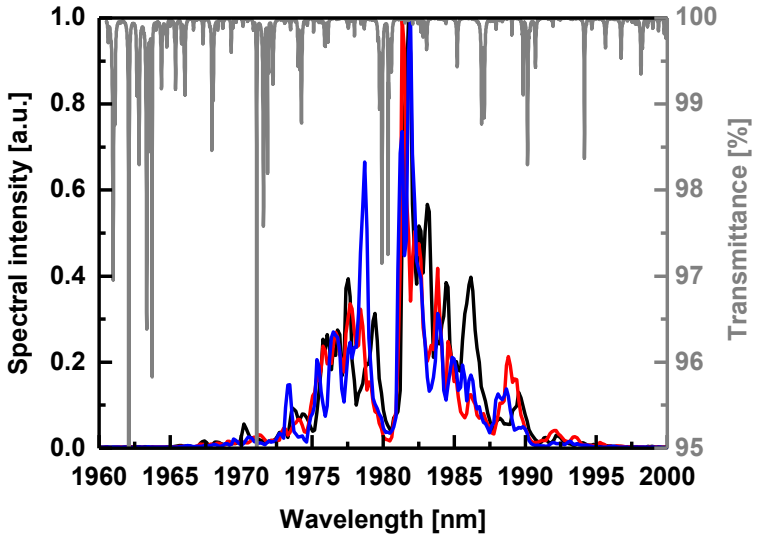


Fig. 5.22 Multi-wavelength emission of the Tm:MgW (E||*Z*) laser with the GaSb-based SESAM No.2 and the prism pair (blue, red and black curves). Grey line represents the calculated transmittance of 1 meter air from HITRAN database.

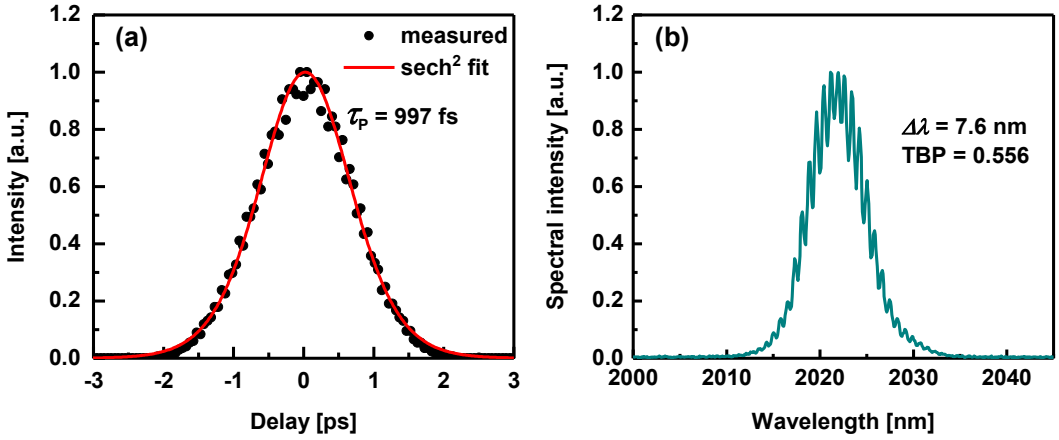


Fig. 5.23 Mode-locked Tm:MgW laser (E||*Y*) by the GaSb-based SESAM No.3: (a) measured AC trace (black symbols) and fit (red line) assuming a sech$^2$-pulse shape, and (b) optical emission spectrum.

The recorded AC trace could be almost perfectly fitted using a sech$^2$-pulse shape profile which yields a pulse duration $\tau_p = 997$ fs (Fig. 5.23a). With the simultaneously measured spectral width of 7.6 nm (cf. Fig. 5.23b) this leads to TBP = 0.556. Although such a TBP

indicates some possibility for pulse compression, insertion of 10 mm thick $CaF_2$ windows under Brewster's angle did not result in pulse shortening but rather is some lengthening for the maximum round trip GDD of −1075 $fs^2$ achievable with 3 plates. Obviously, soliton-like pulse shaping was absent in this laser. While the SESAM is expected to introduce negative GVD, the contribution of the active element is unknown. Adding positive GVD (a 3 mm ZnS plate under Brewster's angle) also did not compress the output pulses.

### 5.4.2 SWCNT-SA mode-locked Tm:MgW laser

The further mode-locking experiments were confined to the $E||Y$ polarization due to its higher gain cross-section and the naturally selected longer emission wavelength. Transmission-type SWCNT-SAs were inserted in the cavity as shown in Figs. 5.1-5.2. The RoC of $M_3$ was −150 mm (cf. Table 5.1 which contains the calculated beam size) because with −100 mm, damage on the SA was observed before mode-locking could be stabilized. Additionally a retro-reflecting Ag mirror (RoC = −100 mm) was placed behind the dichroic $M_2$ cavity mirror for a second pump pass, to utilize the residual pump power. The estimated double-pass absorption was 69.1% assuming equal absorption (44.9%) in the two passes. The latter is in good agreement with the calculated value (46.5%) from the spectroscopic data (cf. Fig. 2.16a). Initially, the $MgF_2$ prism pair with a separation of 12.5 cm was inserted for GDD management.

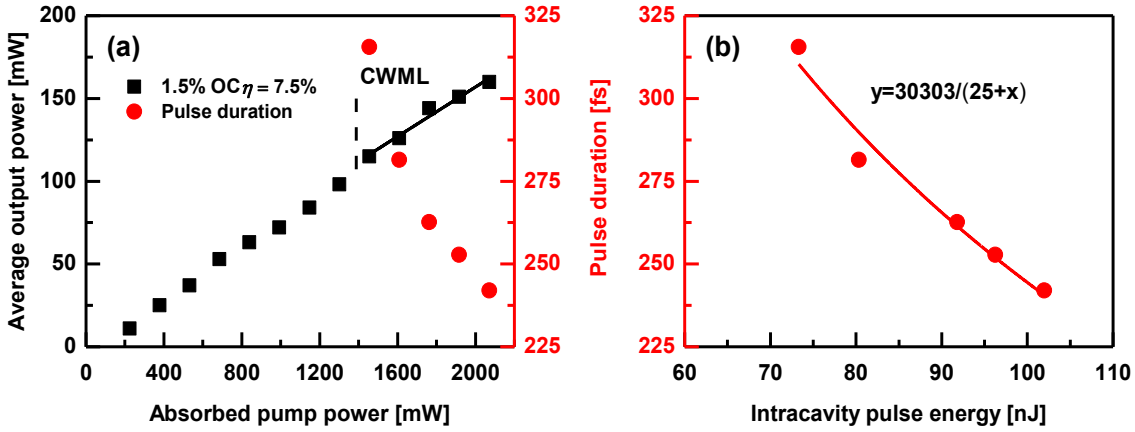


Fig. 5.24 (a) Average output power and pulse duration versus absorbed pump power of the mode-locked Tm:MgW laser with the SWCNT-SA and a prism pair for GDD compensation. The same pulse duration $\tau_p$ data plotted versus the calculated intracavity pulse energy $\epsilon_p$ are shown in (b) together with a fit assuming inversely proportional dependence: $\tau_p = a/(b + \epsilon_p)$.

With the 1.5% OC, the mode-locked laser operated at 2.020 µm. As shown in Fig. 5.24a, stable self-starting CWML was achieved from a threshold corresponding to $P_{out}$ = 115 mW and an average fluence of 506 µJ/$cm^2$ on the SWCNT-SA (calculated for an elliptic spot under Brewster's angle). Increasing the pump power, $P_{out}$ increased with a slope of 7.5% up to a maximum value of 160 mW (at ~ 104.6 MHz) whereas $\tau_p$ decreased from 315 to 242 fs.

The shortest output pulses were generated for a prism material path of ~ 5 mm (single pass). The total round trip GDD due to the prism pair amounted to −992 fs$^2$ in this case. The dependence of the pulse duration on the intracavity pulse energy (which is proportional to the output power) corresponds to a soliton-like pulse shaping but the "area theorem" as described in Chapter 4, is not strictly fulfilled as can be seen in Fig. 5.24b where a correction term $b$ = 25 nJ was necessary for the fit. Figure 5.25 shows the AC trace and the corresponding spectrum of the shortest pulses generated. With a spectral width of 20.6 nm, one arrives at TBP = 0.367, which is very close to the Fourier limit of 0.315.

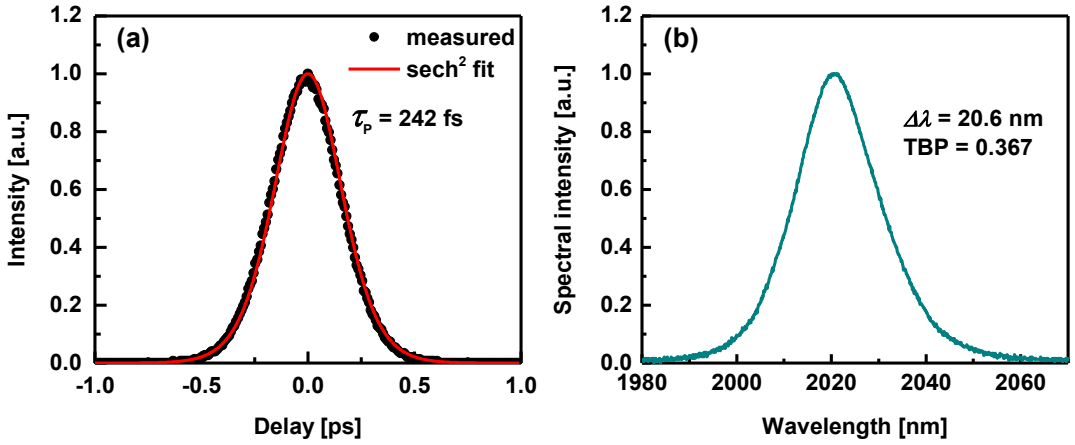


Fig. 5.25 Mode-locked Tm:MgW laser by SWCNT-SA with a prism pair for GDD compensation: (a) measured AC trace (black symbols) and fit (red line) assuming a sech$^2$-pulse shape, and (b) optical emission spectrum.

The 0.5% and 3.0% OCs were also tested in the same laser configuration. With the 0.5% OC, similar pulse duration but lower output power ($P_{out}$ = 45 mW), roughly proportional to the lower transmission, were obtained at the maximum pump level applied. With the 3.0% OC, mode-locking could not be obtained because of the increased cavity losses.

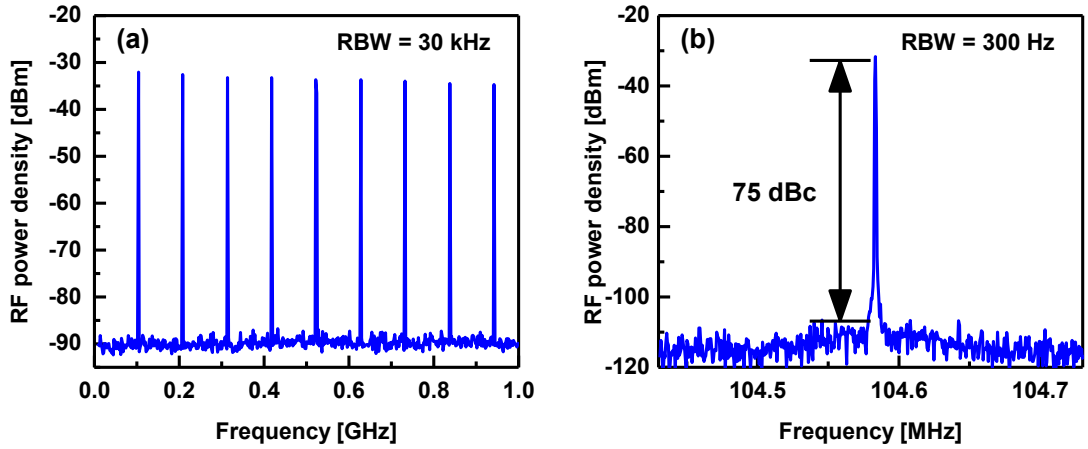


Fig. 5.26 RF spectra of the SWCNT-SA mode-locked Tm:MgW laser: (a) 1 GHz wide-span and (b) fundamental beat note in a 300 kHz wide-span. RBW: resolution bandwidth.

The Tm:MgW laser mode-locked by the SWCNT-SA was very stable, running for hours without any interruption under normal laboratory conditions. The recorded RF spectra (Fig. 5.26) confirmed the absence of Q-switching instabilities. The fundamental beat note centered at ~ 104.6 MHz was 75 dB above noise level.

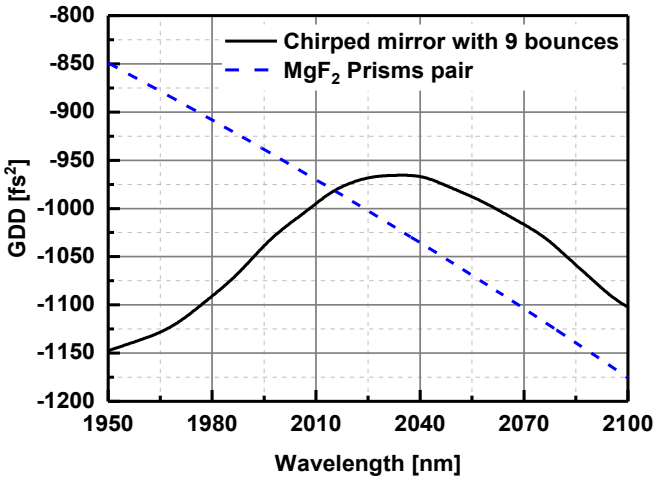


Fig. 5.27 The $MgF_2$ prism pair (separation: 12.5 cm, material path length: 5 mm) with negative round trip GDD ~ −1000 $fs^2$ at 2.020 µm and chirped mirrors (4 bounces scheme from Fig. 5.1 resulting in a total number of 9 bounces per round trip) with similar GDD at the laser wavelength.

Chirped mirrors were also applied for GDD compensation as explained in Fig. 5.27 (cf. Fig. 5.1). In this case also the curved end mirror $M_4$ was a chirped one resulting in a total of 9 bounces per round trip in order to reach as close as possible GDD value to the $MgF_2$ prism pair. However, the derivation of GDD value obtained was about 2/3 of that for the prism pair.

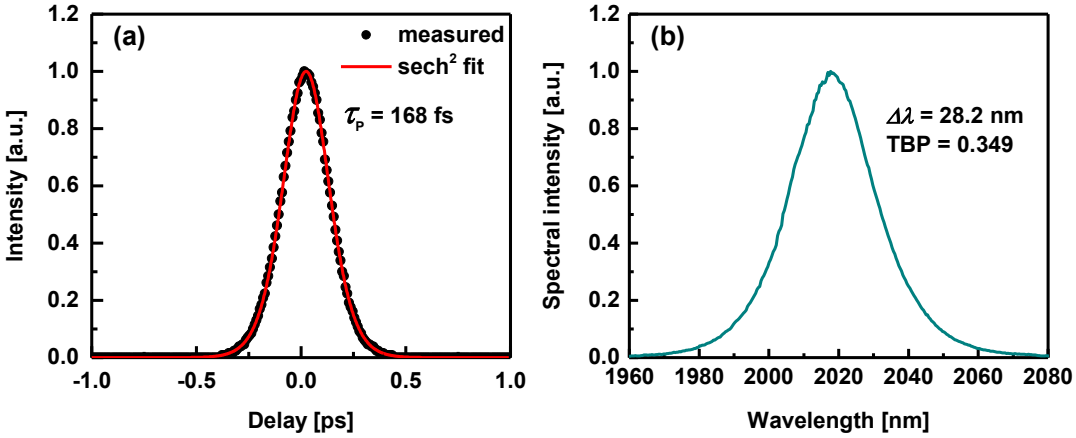


Fig. 5.28 Mode-locked Tm:MgW laser by SWCNT-SA and chirped mirrors for GDD compensation: (a) measured AC trace (black symbols) and fit (red line) assuming a $sech^2$-pulse shape, and (b) optical emission spectrum.

With the 0.5% OC, $P_{out}$ = 37 mW at 2.018 µm was obtained for an absorbed pump power of 1.15 W. The shortest pulse duration was $\tau_p$ = 168 fs (Fig. 5.28a) and with the spectral width

of 28.2 nm one obtains TBP = 0.349 (Fig. 5.28b), which is again very close to the Fourier limit of 0.315. With the 1.5% OC, a similar pulse duration was achieved but the average output power reached $P_{out}$ = 124 mW which was much higher compared to the prism pair ($P_{out}$ = 84 mW for the same absorbed pump power). This is attributed to the lower insertion losses of the chirped mirrors (~ 0.02% per bounce) in comparison to the prism pair.

### 5.4.3 Graphene-SA mode-locked Tm:MgW laser

Both the spectroscopic properties of Tm:MgW and CWML results presented before indicate that $E||Y$ polarization configuration is preferable for femtosecond pulse generation. On the other hand chirped mirrors turned out to be advantageous compared to the prism pair as discussed for the SWCNT-SA mode-locked Tm:MgW laser. Thus, employing graphene-SA, the study was confined to this polarization and chirped mirrors for intracavity GVD compensation.

The mono-, bi-, and tri-layer graphene-SAs available for the present experiment are denoted as 1G 2G and 3G on quartz. The cavity scheme resulting in a total of 9 bounces per round trip on the chirped mirrors was employed with a single pump pass. With the 0.5% OC, stable and self-starting CWML was achieved with all graphene-SAs at an absorbed pump power of 1.15 W, cf. Fig. 5.29. Table 5.6 summarizes the relevant parameters: As more layers of graphene are used, $P_{out}$ decreased from 44 to 22 mW, which is attributed to the increasing non-saturable losses. The 1G amd 3G SAs generated similar pulse durations, while the 2G sample produced a shorter pulse with a ~ 20% larger spectral width. Note that in all cases the TBP was very close to the Fourier limit which explains the almost perfect AC trace fits with $\text{sech}^2$ pulse shape, an indication of soliton-like pulse shaping.

Table 5.6 Mode-locked Tm:MgW laser performance with 1G, 2G, and 3G SAs on quartz for 0.5% OC.

| SA | $\tau_p$ [fs] | $\lambda_L$ [μm] | $\Delta\lambda$ [nm] | TBP | $P_{out}$ [mW] |
|---|---|---|---|---|---|
| 1G on quartz | 182 | 2.017 | 23.9 | 0.321 | 44 |
| 2G on quartz | 148 | 2.015 | 29.2 | 0.320 | 32 |
| 3G on quartz | 173 | 2.015 | 25.7 | 0.328 | 22 |

Fused quartz or silica normally exhibit absorption starting from 2 μm which means additional unwanted cavity losses. Thus the next batch of bi-layer graphene-SAs were manufactured on 2-mm thick $CaF_2$ substrates. Such 2G on $CaF_2$ was employed for the further studies in which the performance of the mode-locked Tm:MgW laser was compared for different OCs and intracavity GDD. The GDD was managed by introducing different number of bounces on the chirped mirrors. Operating with 2, 4 and 6 bounces (single pass) on the plane CMs (as shown in Fig. 5.1), the introduced round-trip GDD, including the contribution of the chirped curved mirror $M_4$ and the $CaF_2$ substrate, amounted to −735, −1235, and

−1735 fs$^2$, respectively. The different numbers of bounces in the cavity correspond to repetition rates of 66, 76 and 87 MHz, respectively. At a fixed absorbed pump power of 1.15 W, CWML could be achieved in most of the cases.

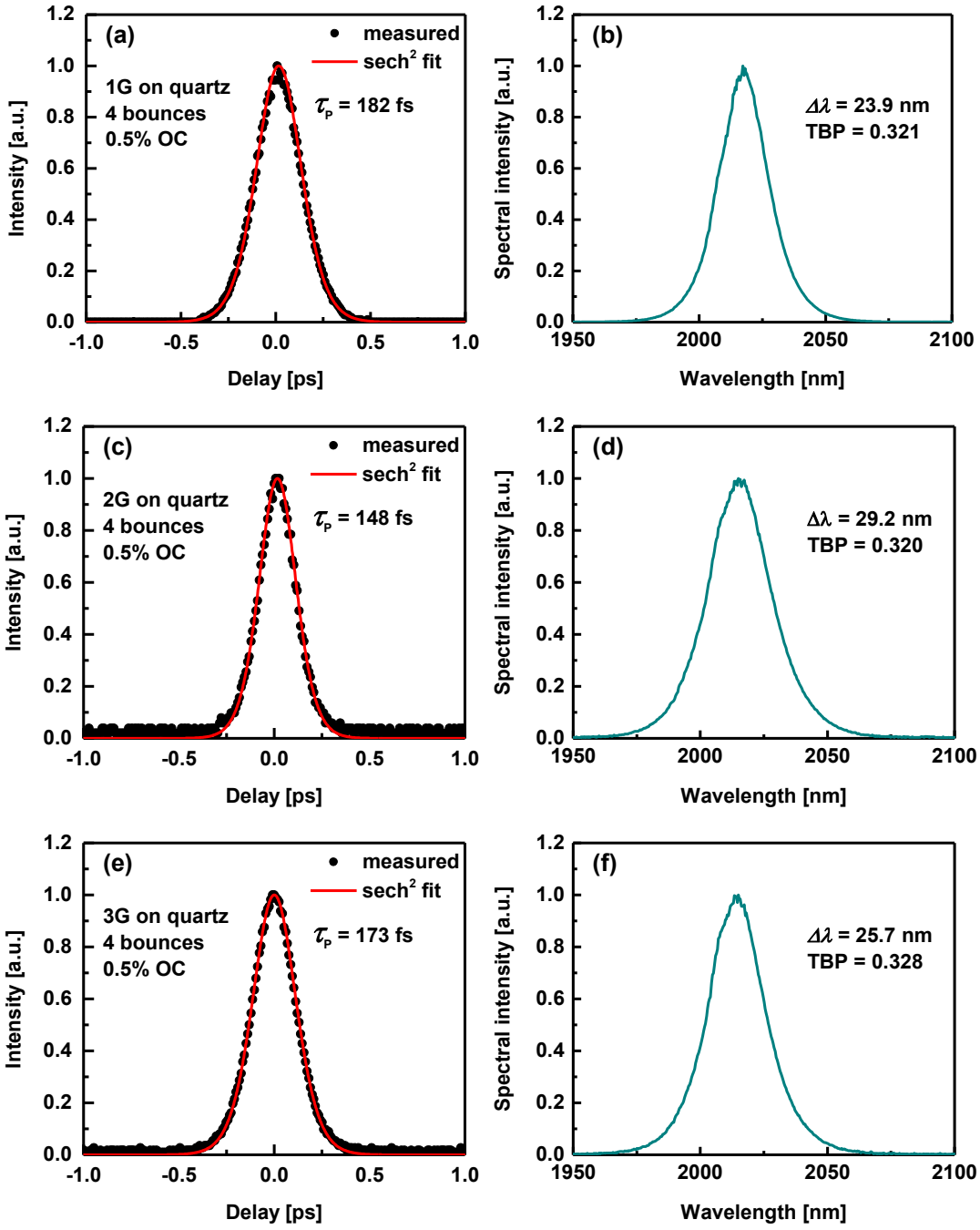


Fig. 5.29 Mode-locked Tm:MgW laser with 1G, 2G, and 3G on quartz: (a), (c), and (e) present measured AC traces (black symbols) and fits (red line) assuming a sech$^2$-pulse shape, and (b), (d), and (f) present the optical emission spectra.

The mode-locked laser characteristics in terms of pulse duration and average output power are summarized in Table 5.7. Note that a configuration with 0 bounces corresponding

to minimum introduced negative round-trip GDD of −125 fs$^2$ by the chirped mirror $M_4$ was also tested, however, the Tm:MgW laser operated only in the CW regime.

Using the 2 bounce scheme, stable and self-starting CWML was achieved with the 1.5% OC, reaching $P_{out}$ = 96 mW (pulse energy of 1.45 nJ) and $\tau_p$ = 96 fs (Fig. 5.30a). The spectral width of 45.8 nm (Fig. 5.30b) resulted in TBP = 0.324. The laser operated at 2.016 µm.

Table 5.7 Mode-locked Tm:MgW laser with 2G on $CaF_2$: performance for different OCs and intracavity GDD at an absorbed power of 1.15 W.

| | 0 bounce | 2 bounces | | 4 bounces | | 6 bounces | |
|---|---|---|---|---|---|---|---|
| | | $\tau_p$ [fs] | $P_{out}$ [mW] | $\tau_p$ [fs] | $P_{out}$ [mW] | $\tau_p$ [fs] | $P_{out}$ [mW] |
| 0.2% OC | CW | 100* | 20 | 91 | 18 | 111 | 15 |
| 0.5% OC | CW | 106* | 54 | 86 | 39 | 116 | 33 |
| 1.5% OC | CW | 96 | 96 | 116 | 91 | 152 | 62 |

* multi-pulse operation occurs.

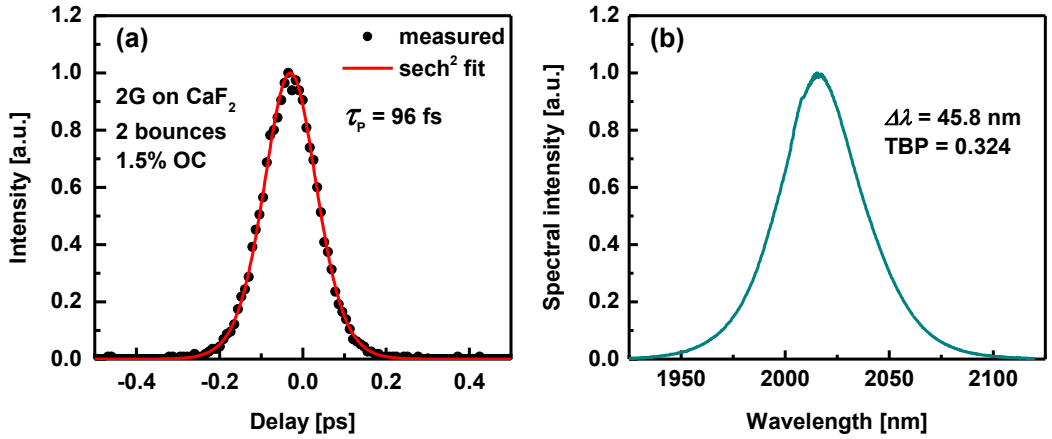


Fig. 5.30 Mode-locked Tm:MgW laser with 2G on $CaF_2$, 2 bounce GDD compensation scheme and the 1.5% OC: (a) measured AC trace (black symbols) and fit (red line) assuming a sech$^2$-pulse shape, and (b) optical emission spectrum.

Shorter steady-state pulses are expected for lower output coupling in the quasi-3-level Tm laser system due to the modified gain profile. However, as discussed in Chapter 4, when the intracavity power was too high (*cases in Table 5.7), pulse break-up (multi-pulse) was observed. With the 0.2% OC, a bound state double-pulse could be stabilized similar to observations described in [111]. Figure 5.31a shows the AC trace of such a bound state, from which a separation of 433 fs was derived. The measured AC trace was fitted assuming a double-pulse with equal amplitudes and pulse duration of 100 fs (sech$^2$ shape), and such a separation. Complete modulation of the optical spectrum was observed in this case (cf. Fig. 5.31b). The FWHM of the modulated spectrum was slightly narrower and thus the TBP remained almost unchanged in the double-pulse regime. The spectral modulation profile depends on the phase difference $\phi$ of the two pulses (cf. Fig. 5.32). The measured spectrum

could be almost perfectly fitted assuming a phase difference $\phi$=3π/4. Such a bound state double-pulse operation is sometimes referred to as a $\phi$=3π/4 doublets [111]. Well separated pairs by up to few picoseconds, with equal or up to 4 times different energy content were also observed in this laser.

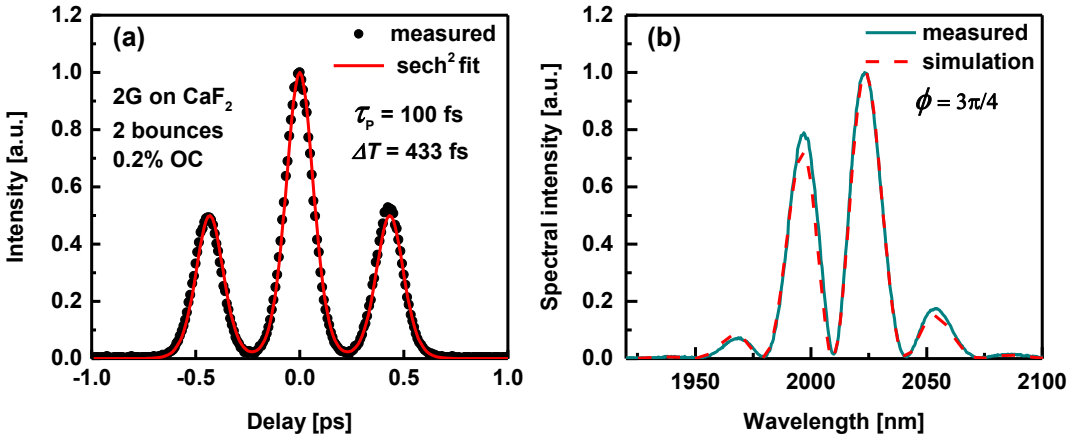


Fig. 5.31 AC trace (a) and optical spectrum (b) for the double-pulse regime of the Tm:MgW laser. The simulated spectrum in (b) is calculated assuming equal amplitude of two 100-fs long sech$^2$-shaped pulses separated by 433 fs with a relative phase of $\phi$ = 3π/4 corresponding to a bound state.

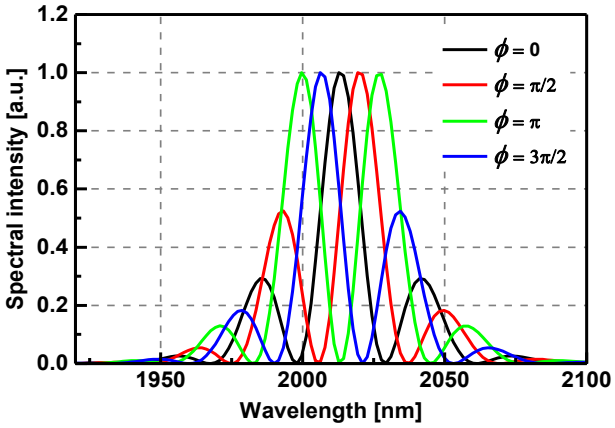


Fig. 5.32 Calculated spectra assuming two equal in amplitude 100-fs long sech$^2$-shaped pulses with a separation of 433 fs. $\phi$ indicates the phase difference of the two pulses.

The 4 bounce configuration which introduced a round-trip GDD around −1235 fs$^2$ led to the shortest pulse of $\tau_p$ = 86 fs (0.5% OC) at 2.017 µm. For more negative GDD (6 bounce configuration) the pulses started to broaden. Figure 5.33 shows the AC trace of the shortest pulse achieved together with a longer scale measurement up to 50 ps (inset) as a proof for single pulse operation. The corresponding spectral width of 53 nm (Fig. 5.34d) results in TBP = 0.335 which is very close to the Fourier limit. Note that broad Raman peaks were also observed around 2.200 µm which is related to the broad spectral extent of the pulse.

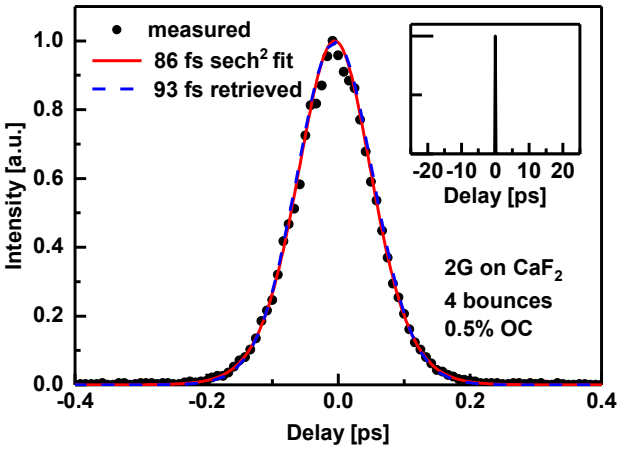


Fig. 5.33 AC trace (black symbols) of the shortest pulse and fit (red line) assuming a $\text{sech}^2$-pulse shape. The dashed blue line is the AC of the retrieved FROG trace. Inset: AC trace in a 50 ps time window.

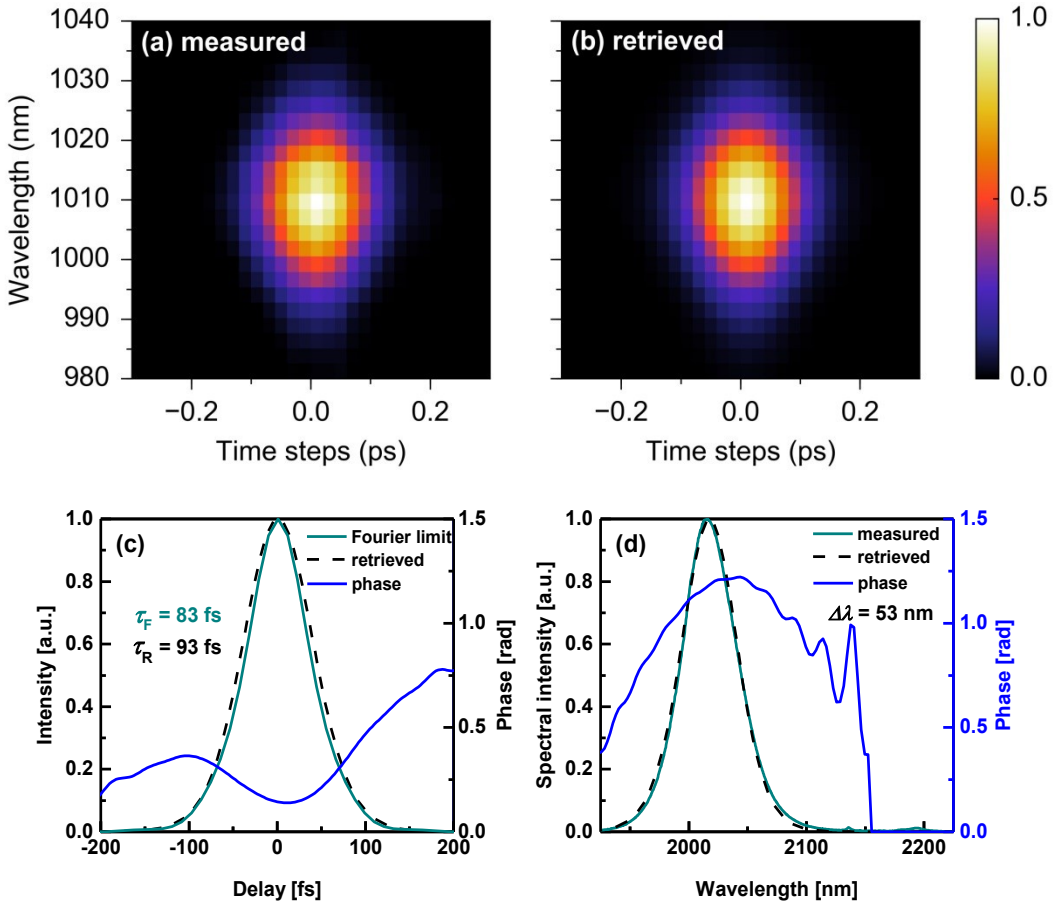


Fig. 5.34 Measured (a) and retrieved (b) SHG-FROG trace, together with the derived temporal (c) and spectral (d) intensity and phase (green curve: directly measured spectrum by an InGaAs spectrometer). $\tau_R$: retrieved pulse duration, $\tau_F$: Fourier limit pulse duration.

The shortest pulses were characterized also by second-harmonic generation frequency resolved gating (SHG-FROG) technique using a 1 mm thick type-I $LiNbO_3$ crystal. Figure 5.34 shows the measured FROG trace (a) next to the retrieved FROG trace (b), together with the derived temporal (c) and spectral (d) intensity and phase. From the FROG-retrieval, a pulse duration of 93 fs was obtained with an almost symmetric pulse shape. The derived pulse shape and duration were in excellent agreement with the directly measured autocorrelation trace, cf. Fig. 5.33. The spectral width resulting from the FROG retrieval was 53 nm, coinciding with the one estimated from the directly measured spectrum, cf. Fig. 5.34d. The FROG error on a 64×64 grid size was 0.004. The residual linear chirp parameter was derived from a parabolic fit to the spectral phase whereby its sign was confirmed by placing additional $CaF_2$ plates in front of the FROG setup. Doing so, a value of −640 $fs^2$ was obtained which is consistent with the operation of ultrashort pulse oscillators in the negative GDD regime for maximum stability.

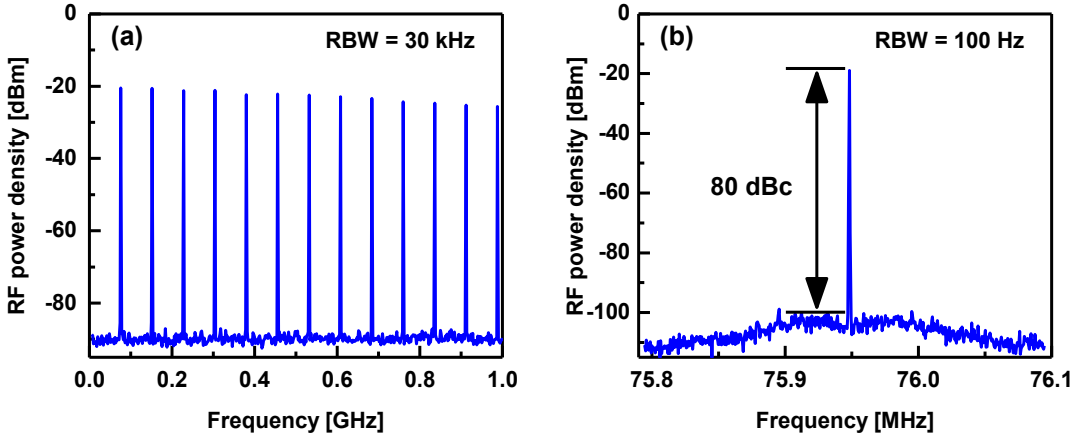


Fig. 5.35 RF spectra of the mode-locked Tm:MgW with 2G on $CaF_2$, 4 bounce GDD compensation and the 0.5% OC: (a) 1 GHz wide-span and (b) fundamental beat note in a 300 kHz wide span. RBW: resolution bandwidth.

To verify the stability of the mode-locked Tm:MgW laser, RF spectra were recorded in different span ranges. The results for the shortest pulse configuration are presented in Fig. 5.35. The harmonic beat notes show almost constant extinction ratio (Fig. 5.35a) whereas the fundamental beat note at 75.95 MHz displays an extinction ratio of 80 dB above the carrier (Fig. 5.35b). Such an extinction ratio was typical also for the other stable single pulse operation regimes included in Table 5.7.

### 5.4.4 Summary of the mode-locked Tm:MgW laser results

Table 5.8 summarizes the best results achieved in terms of pulse duration with the mode-locked Tm:MgW lasers. Although GDD compensation was attempted with the SESAM mode-locked Tm:MgW laser this did not result in pulse shortening and no improvement of the TBP could be achieved either.

Table 5.8 Mode-locking results achieved with the Tm:MgW laser. PP and CM stand for prism pair and chirped mirrors for intracavity GDD (group delay dispersion) compensation, respectively. $\tau_p$: pulse duration (FWHM), $\lambda_L$: laser wavelength, $\Delta\lambda$: bandwidth (FWHM), $P_{abs}$: absorbed power, $P_{out}$: average output power, $f_{rep}$: repetition rate, SA: saturable absorber, OC: output coupler.

| SA | GDD | $\tau_p$ [fs] | $\lambda_L$ [nm] | $\Delta\lambda$ [nm] | $P_{abs}$ [W] | $P_{out}$ [mW] | $f_{rep}$ [MHz] | OC [%] |
|---|---|---|---|---|---|---|---|---|
| SESAM | – | 997 | 2021 | 7.6 | 0.8 | 30 | 104.9 | 1.5 |
| SWCNTs | PP | 242 | 2020 | 20.6 | 2.07 | 160 | 104.6 | 1.5 |
| | CM | 168 | 2018 | 28.2 | 1.15 | 124 | 76.0 | 1.5 |
| | | | | | 1.15 | 37 | 76.0 | 0.5 |
| Graphene | CM | 96 | 2016 | 45.8 | 1.15 | 96 | 66.0 | 1.5 |
| | | 86 | 2017 | 53.0 | 1.15 | 39 | 76.0 | 0.5 |

Comparing with the results achieved with the mode-locked Tm:CALGO laser, one can conclude that the available SESAMs enable sub-ps pulse generation but further optimization of their parameters will be necessary for implementation in the 100 fs pulse duration range. This conclusion is supported by the much shorter pulse durations achieved with the SWCNT and graphene SAs.

## 5.5 Summary and comparison of the mode-locked laser results

The results obtained in this chapter are compared with the state-of-the-art in terms of pulse duration and average power for such bulk 2-µm mode-locked lasers in Fig. 5.36.

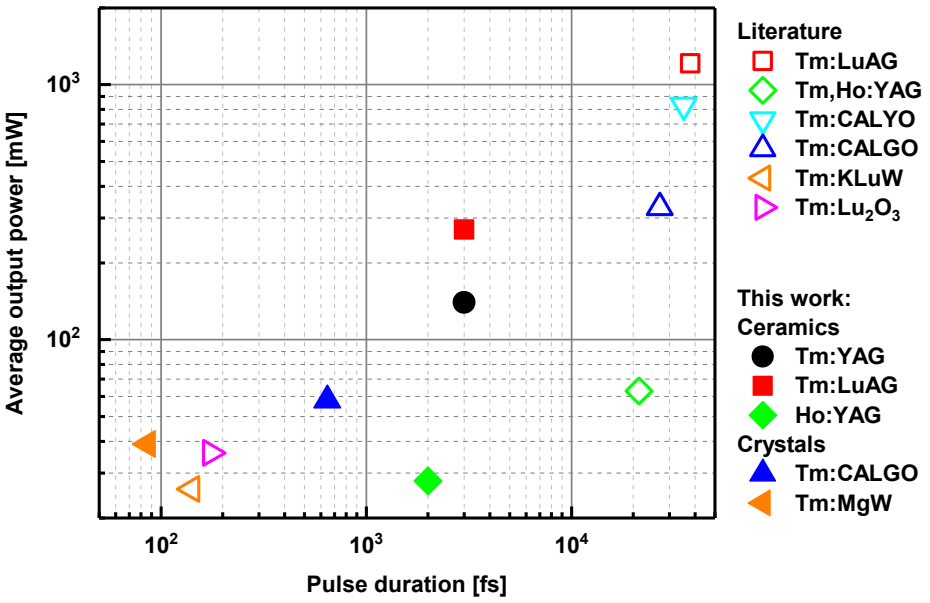


Fig. 5.36 Overview of the state-of-the-art concerning passively mode-locked bulk 2 µm lasers.

Table 5.9 presents a complete compilation of the mode-locking results obtained with such lasers from the literature and the present work. Comparing the host materials, it can be seen

that the best results in terms of shortest pulses were obtained with glass, tungstates, sesquioxides as well as CALGO and CALYO. This is mainly attributed to the flat and smooth gain spectra profiles as discussed in Chapter 2. The physical factors contributing to such advantageous gain profiles can be identified as inhomogeneous broadening due to the existence of multiple sites or distortion of the crystal field around the dopant ion. However, anisotropic materials offer also additional flexibility is selecting the most advantageous orientation.

Table 5.9 Summary of mode-locked Tm and Ho laser results (from the literature and this work). PP and CM stand for prism pair and chirped mirrors for intracavity GDD (group delay dispersion) compensation, respectively. $\tau_p$: pulse duration (FWHM), $\lambda_L$: laser wavelength, $\Delta\lambda$: bandwidth (FWHM), $P_{out}$: average output power, $f_{rep}$: repetition rate, SA: saturable absorber.

| Hosts | Material Form | SA | GDD | $\tau_p$ | $\lambda_L$ [nm] | $\Delta\lambda$ [nm] | $P_{out}$ [mW] | $f_{rep}$ [MHz] |
|---|---|---|---|---|---|---|---|---|
| Ho:YAG [112] | Crystal | *Active* | No | 570 ps | NA | NA | NA | NA |
| Cr,Tm:YAG [113] | Crystal | *Active* | No | 45 ps | 2013 | 0.22 | 160 | 62 |
| Tm:KLuW [80] | Crystal | SWCNTs | No | 9.7 ps | 1944 | 0.45 | 240 | 126 |
| Tm:GPNG [142] | Glass | GaSb SESAM | PP | 410 fs | 1997 | 10.4 | 84 | 222 |
| Tm:KYW [143] | Crystal | GaSb SESAM | PP | 386 fs | 2029 | 11.14 | 235 | 97 |
| Tm:LuAG [130] | Crystal | GaAs SESAM | No | 38 ps | 2023 | 0.42 | 1210 | 129 |
| Tm,Ho:YAG [132] | Crystal | GaSb SESAM | CM | 21ps | 2091 | 2.6 | 63 | 107 |
| Tm:CALYO [138] | Crystal | GaAs SESAM | No | 35 ps | 1959 | 3.0 | 830 | 145 |
| Tm:CALGO [139] | Crystal | GaAs SESAM | No | 27 ps | 1950 | 2.0 | 330 | 129 |
| Tm:$Lu_2O_3$ [123] | Crystal | SWCNTs | PP | 175 fs | 2070 | 27.4 | 36 | 88 |
| Tm:KLuW [124] | Crystal | SWCNTs | PP | 141 fs | 2037 | 26.5 | 26 | 88 |
| This work: | | | | | | | | |
| Tm:YAG | Ceramic | GaSb SESAM | PP | 3 ps | 2012 | 2.5 | 140 | 89 |
| Tm:LuAG | Ceramic | GaSb SESAM | PP | 3 ps | 2022 | 2.5 | 270 | 93 |
| Ho:YAG | Ceramic | GaSb SESAM | No | 2-16 ps | 2059-2121 | 2.6-0.8 | 250-28 | 83 |
| Tm:CALGO | Crystal | GaSb SESAM | PP | 646 fs | 2021 | 9.2 | 58 | 101 |
| Tm:MgW | Crystal | GaSb SESAM | No | 997 fs | 2021 | 7.6 | 30 | 105 |
| | | SWCNTs | PP | 242 fs | 2020 | 20.6 | 160 | 105 |
| | | | CM | 168 fs | 2018 | 28.2 | 124 | 76 |
| | | Graphene | CM | 86 fs | 2017 | 53 | 39 | 76 |

The other essential aspect is related to the SA applied. Due to the faster relaxation time of the GaSb-based SESAMs used in the present work, the pulse durations with the same active media (garnets as well as CALGO) could be significantly improved by 1-2 orders of magnitude, cf. Fig. 5.36. However, the shortest pulses are generated using carbon nanostructure based SAs. Compared to SWCNTs, graphene seems more promising since the modulation depth can be easily changed and controlled by transfer of a different number of layers onto the substrate as discussed in Chapter 3.

An important factor which was not discussed in detail in this chapter but was essential in selecting the active materials is the emission wavelength. Host materials that help to naturally select wavelengths above 2 μm are advantageous for femtosecond pulse generation because one can automatically avoid problems with air absorption and dispersion. This was the case with all the crystals and ceramics studied in this work, cf. Table 5.9. Operation below 2 μm normally results in narrower spectra of the mode-locked laser supporting only picosecond pulses while shifting the spectrum by wavelength selective elements (e.g. by the OC) might also restrict the spectrum. Operation with nitrogen purging was attempted with some of the lasers studied in this work but was not effective.

The best result in the present work was achieved using chirped mirrors for GDD compensation. Although they do not permit continuous control of the intracavity GDD, the lower insertion losses and the relaxed alignment procedure seem to be more important advantages.

# Chapter 6
# Conclusion and outlook

In this work, novel solid-state laser host materials doped with Tm and Ho ions were studied for ultrashort pulse generation at ~ 2 µm in the regime of passive mode-locking. Combining their advantageous spectroscopic properties with novel saturable absorbers such as GaSb SESAMs, SWCNTs and graphene, successful self-starting and steady-state mode-locked operation was achieved with various 2 µm lasers for the first time. The main achievements and findings of the present work can be summarized as follows:

- Complete spectroscopic characterization of 4 novel solid-state laser materials for the 2 µm spectral range, including 2 garnet ceramics (Tm:LuAG and Ho:YAG), and 2 single crystals (Tm:CALGO and Tm:MgW).
- Successful demonstration of the potential of transparent laser ceramics combined with near-surface QW design GaSb-based SESAMs for mode-locking around 2 µm achieving record short pulse durations for these materials (in comparison with their crystalline counterparts).
- Shortest pulse durations generated employing novel SAs around 2 µm: GaSb-based SESAM (Tm:CALGO) and graphene (Tm:MgW). Compared with SWCNT, graphene benefits from the possibility to control the modulation depth.
- As shown in Fig. 6.1, after more than 35 years of development, this work produced the first sub-100 fs (appr. 12 optical cycles) pulses in the 2 µm spectral range from a mode-locked bulk solid state laser.

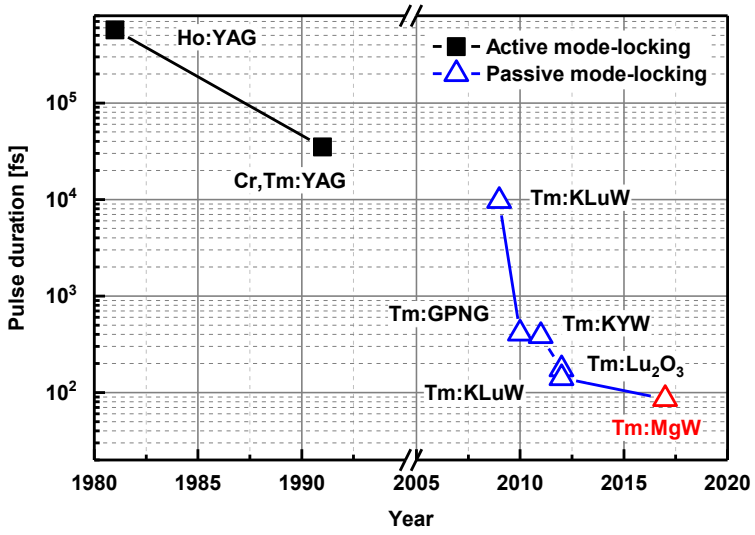


Fig.6.1 Development of mode-locked bulk solid-state lasers at ~ 2 µm (cf. Table 5.9).

Despite the first sub-100 fs pulse generation directly from a bulk solid-state laser near 2 µm, there is still a long way to go towards few cycle pulses. Possible strategies that could be successful in reaching even shorter (sub-50 fs) pulses with such types of lasers include:

- Kerr lens mode-locking because such tendency or spontaneous self-mode-locking was not observed in the described experiments. Comparing with other spectral ranges (e.g. 1 µm) this can be interpreted as too low value of the nonlinear refractive index of the laser materials near 2 µm. This can be expected farther from their band-gap but literature data for this spectral range do not exist. Adding artificial self-phase-modulation in a third cavity waist using materials with smaller but sufficient to avoid TPA band-gap (e.g. ZnS) could eventually result in self-focusing in the mode-locked regime. Such KLM has been achieved in Yb:YAG thin-disk lasers [144]. However there is no report of pure Kerr lens mode-locking of such lasers near 2 µm in the literature. Another approach to obtain Kerr lens mode-locking is to increase the intracavity power. New cavity designs and pump sources will be needed for this and Ho-lasers which offer in-band pumping with low heat generation seem more promising due to the easy scalability of Tm-fiber pump lasers.
- Improved SA. Compared with SWCNTs and graphene, GaSb-based SESAMs still have a lot of room for improvement in terms of non-saturable losses and relaxation time. By implementing them in Kerr lens mode-locked lasers they could contribute to self-starting and stabilization while the enhanced SPM will enable the generation of substantially shorter pulses which, from spectroscopic point of view, should be supported by some of the laser materials studied here.
- New laser hosts: There exist other laser hosts which combine the advantageous features identified in the present work. For instance, Tm-doped cubic sesquioxides ($Lu_2O_3$, $Sc_2O_3$ and $Y_2O_3$) naturally emit well above 2 µm and similar to YAG and LuAG, they are suitable for laser ceramics. Moreover, they exhibit superior thermo-mechanical characteristics. Mixed ceramics (e.g. $Lu_aSc_bY_{2-a-b}O_3$, $a+b < 2$) are technologically easier to fabricate than mixed crystals which will facilitate the spectral broadening due to the compositional crystal disorder.
- Co-doped materials. The emission spectra of Tm and Ho ions in fact overlap and instead of mixing hosts, one can try to mode-lock a co-doped system (i.e. a crystal or ceramic doped with Tm and Ho). This is an idea not exploited so far for femtosecond pulse generation. In such co-doped tunable CW lasers (pumped through the Tm ion) it is hardly possible to assign the emission in the overlapping range. The co-doped system is rather complex: The energy transfer plays an essential role and the doping ratio is a crucial parameter for it. However, in-band pumping might offer an additional degree of freedom in this case.
- Pulse width reduction after amplification. Existing laser technology enables pulse compression after amplification. Direct use of Tm-fibers for amplification of the pulse

train from the mode-locked laser is not possible because the emission maximum in glass is at much shorter wavelengths. However, the so-called single crystal fibers (SCF) have been developed and successfully applied in other spectral regions, e.g. with Yb-doping near 1 µm [145]. In fact these are not fibers because the laser light is not guided but simply long (few cm) crystal rods with a diameter of the order of 1 mm or less in which the pump light experiences internal reflection. Such SCFs benefit from both the advantages of fibers, such as the straightforward thermal management and high gain, and the spectroscopic and thermo-mechanical properties of single crystals. Moreover, similar to fibers they can be applied at high repetition rates, i.e. preserving the original repetition rate of the mode-locked laser. Suitable SCFs for the 2 µm spectral range seem such based on Tm-doped garnets or CALGO crystals. Despite the gain narrowing effect in the process of laser amplification it is possible to recompress the pulses to even shorter (than the initial) pulse durations. Such self-compression towards the few-cycle limit can be achieved by simply focusing the beam into a bulk material such as YAG [146]. The soliton mechanism required for this is provided near 2 µm by the anomalous dispersion typical for many materials at this wavelength. Having reached few-cycle pulse durations, one can perform carrier envelope phase (CEP) stability measurements and implement methods for CEP stabilization of the mode-locked laser.

# References


1. U. Keller, *Ultrafast solid-state lasers*, Landolt-Börnstein, Group VIII/1B1, Laser Physics and Applications. Subvolume B: Laser Systems. Part 1, G. Herziger, H. Weber, and R. Proprawe, eds., (Springer, Berlin, 2007), pp. 33-167.
2. U. N. Singh, B. M. Walsh, J. Yu, M. Petros, M. J. Kavaya, T. F. Refaat, and N. P. Barnes, "Twenty years of Tm:Ho:YLF and LuLiF laser development for global wind and carbon dioxide active remote sensing," Opt. Mater. Express **5**, 827-837 (2015).
3. K. Scholle, S. Lamrini, P. Koopmann, and P. Fuhrberg, "2 μm laser sources and their possible applications," in *Frontiers in Guided Wave Optics and Optoelectronics,* B. Pal, ed. (InTech, Rijeka, 2010), pp. 471-500.
4. J. Herrmann and B. Wilhelmi, *Lasers for ultrashort light pulses* (North-Holland, Amsterdam, 1987).
5. V. Petrov, "Frequency down-conversion of solid-state laser sources to the mid-infrared spectral range using non-oxide nonlinear crystals," Progress Quantum Electron. **42**, 1-106 (2015).
6. A. Schliesser, N. Picqué, and T. W. Hänsch, "Mid-infrared frequency combs," Nat. Photonics **6**, 440-449 (2012).
7. C. J. Saraceno, F. Emaury, C. Schriber, A. Diebold, M. Hoffmann, M. Golling, T. Südmeyer, and U. Keller, "Toward millijoule-level high-power ultrafast thin-disk oscillators," IEEE J. Sel. Top. Quantum Electron. **21**, 106-123 (2015).
8. J.-C. Diels and W. Rudolph, *Ultrashort laser pulse phenomena,* 2nd ed. (Academic press, 2006).
9. Z. Chang, *Fundamentals of attosecond optics,* (CRC Press, Boca Raton, FL, 2011).
10. D. Sanchez, M. Hemmer, M. Baudisch, S. L. Cousin, K. Zawilski, P. Schunemann, O. Chalus, C. Simon-Boisson, and J. Biegert, "7 μm, ultrafast, sub-millijoule-level mid-infrared optical parametric chirped pulse amplifier pumped at 2 μm," Optica **3**, 147-150 (2016).
11. A. Baltuška, T. Fuji, and T. Kobayashi, "Controlling the carrier-envelope phase of ultrashort light pulses with optical parametric amplifiers," Phys. Rev. Lett. **88**, 133901 (2002).
12. T. Fuji, N. Ishii, C. Y. Teisset, X. Gu, Th. Metzger, A. Baltuska, N. Forget, D. Kaplan, A. Galvanauskas, and F. Krausz, "Parametric amplification of few-cycle carrier-envelope phase-stable pulses at 2.1 μm," Opt. Lett. **31**, 1103-1105 (2006).
13. Y. Deng, A. Schwarz, H. Fattahi, M. Ueffing, X. Gu, M. Ossiander, T. Metzger, V. Pervak, H. Ishizuki, and T. Taira, "Carrier-envelope-phase-stable, 1.2 mJ, 1.5 cycle laser pulses at 2.1 μm," Opt. Lett. **37**, 4973-4975 (2012).
14. C. Homann, M. Bradler, M. Förster, P. Hommelhoff, and E. Riedle, "Carrier-envelope phase stable sub-two-cycle pulses tunable around 1.8 μm at 100 kHz," Opt. Lett. **37**, 1673-1675 (2012).

15. A. F. Campos, A. Meijerink, C. d. M. Donegá, and O. L. Malta, "A theoretical calculation of vibronic coupling strength: the trend in the lanthanide ion series and the host-lattice dependence," J. Phys. Chem. Solids **61**, 1489-1498 (2000).
16. I. T. Sorokina, "Crystalline mid-infrared lasers," in *Solid-State Mid-Infrared Laser Sources, Topics in Applied Physics*, I. T. Sorokina and K. L. Vodopyanov, eds. (Springer, Berlin, 2003), pp. 262-358.
17. M. Eichhorn, "Quasi-three-level solid-state lasers in the near and mid infrared based on trivalent rare earth ions," Appl. Phys. B **93**, 269-316 (2008).
18. K. Möllmann, M. Schrempel, B.-K. Yu, and W. Gellermann, "Subpicosecond and continuous-wave laser operation of $(F_2^+)_H$ and $(F_2^+)_{AH}$ color-center lasers in the 2-μm range," Opt. Lett. **19**, 960-962 (1994).
19. T. H. Maiman, "Stimulated optical radiation in ruby," Nature **187**, 493-494 (1960).
20. J. O. White, "Parameters for quantitative comparison of two-, three-, and four-level laser media, operating wavelengths, and temperatures," IEEE J. Quantum Electron. **45**, 1213-1220 (2009).
21. R. C. Stoneman and L. Esterowitz, "Efficient, broadly tunable, laser-pumped Tm:YAG and Tm:YSGG cw lasers," Opt. Lett. **15**, 486-488 (1990).
22. V. A. French, R. R. Petrin, R. C. Powell, and M. Kokta, "Energy-transfer processes in $Y_3Al_5O_{12}$:Tm,Ho," Phys. Rev. B **46**, 8018-8026 (1992).
23. M. Born and E. Wolf, *Principles of optics,* 7th ed. (Cambridge University Press, Cambridge, 1999).
24. P. Loiko, P. Segonds, P. L. Inácio, A. Peña, J. Debray, D. Rytz, V. Filippov, K. Yumashev, M. C. Pujol, and X. Mateos, "Refined orientation of the optical axes as a function of wavelength in three monoclinic double tungstate crystals $KRE(WO_4)_2$ (RE= Gd, Y or Lu)," Opt. Mater. Express **6**, 2984-2990 (2016).
25. A. A. Kaminskii, "Laser crystals and ceramics: recent advances," Laser Photonics Rev. **1**, 93-177 (2007).
26. A. Ikesue and Y. L. Aung, "Ceramic laser materials," Nat. Photon. **2**, 721-727 (2008).
27. B. M. Walsh, "Judd-Ofelt theory: principles and practices," in *Advances in Spectroscopy for Lasers and Sensing*, B. Di Bartolo and O. Forte, eds. (Springer Netherlands, Dordrecht, 2006), pp. 403-433.
28. D. E. McCumber, "Einstein relations connecting broadband emission and absorption spectra," Phys, Rev. **136**, A954-A957 (1964).
29. A. S. Yasyukevich, V. G. Shcherbitskii, V. É. Kisel', A. V. Mandrik, and N. V. Kuleshov, "Integral method of reciprocity in the spectroscopy of laser crystals with impurity centers," J. Appl. Spectrosc. **71**, 202-208 (2004).
30. B. Aull and H. Jenssen, "Vibronic interactions in Nd: YAG resulting in nonreciprocity of absorption and stimulated emission cross sections," IEEE J. Quantum Electron. **18**, 925-930 (1982).
31. Y.-S. Yong, S. Aravazhi, S. A. Vázquez-Córdova, J. J. Carjaval, F. Díaz, J. L. Herek, S. M. García-Blanco, and M. Pollnau, "Temperature-dependent absorption and emission of

potassium double tungstates with high ytterbium content," Opt. Express **24**, 26825-26837 (2016).

32. M. C. Pujol, M. A. Bursukova, F. Güell, X. Mateos, R. Solé, J. Gavaldà, M. Aguiló, J. Massons, F. Díaz, P. Klopp, U. Griebner, and V. Petrov, "Growth, optical characterization, and laser operation of a stoichiometric crystal $KYb(WO_4)_2$," Phys. Rev. B **65**, 165121 (2002).
33. H. Kühn, S. T. Fredrich-Thornton, C. Kränkel, R. Peters, and K. Petermann, "Model for the calculation of radiation trapping and description of the pinhole method," Opt. Lett. **32**, 1908-1910 (2007).
34. S. A. Payne, L. Chase, L. K. Smith, W. L. Kway, and W. F. Krupke, "Infrared cross-section measurements for crystals doped with $Er^{3+}$, $Tm^{3+}$, and $Ho^{3+}$," IEEE J. Quantum Electron. **28**, 2619-2630 (1992).
35. J. T. Thomas, M. Tonelli, S. Veronesi, E. Cavalli, X. Mateos, V. Petrov, U. Griebner, J. Li, Y. Pan, and J. Guo, "Optical spectroscopy of $Tm^{3+}$:YAG transparent ceramics," J. Phys. D: Appl. Phys. **46**, 375301 (2013).
36. N. P. Barnes, M. G. Jani, and R. L. Hutcheson, "Diode-pumped, room-temperature Tm:LuAG laser," Appl. Opt. **34**, 4290-4294 (1995).
37. K. Scholle, E. Heumann, and G. Huber, "Single mode Tm and Tm,Ho:LuAG lasers for LIDAR applications," Laser Phys. Lett. **1**, 285-290 (2004).
38. R. D. Shannon, "Revised effective ionic radii and systematic studies of interatomic distances in halides and chalcogenides," Acta Cryst. A **32**, 751-767 (1976).
39. S. Lamrini, P. Koopmann, M. Schäfer, K. Scholle, and P. Fuhrberg, "Efficient high-power Ho:YAG laser directly in-band pumped by a GaSb-based laser diode stack at 1.9 μm," Appl. Phys. B **106**, 315-319 (2011).
40. R. Lan, X. Mateos, Y. Wang, J. M. Serres, P. Loiko, J. Li, Y. Pan, U. Griebner, and V. Petrov, "Semiconductor saturable absorber Q-switching of a holmium micro-laser," Opt. Express **25**, 4579-4584 (2017).
41. B. M. Walsh, G. W. Grew, and N. P. Barnes, "Energy levels and intensity parameters of ions in $Y_3Al_5O_{12}$ and $Lu_3Al_5O_{12}$," J. Phys. Chem. Solids **67**, 1567-1582 (2006).
42. P. O. Petit, J. Petit, P. Goldner, and B. Viana, "Inhomogeneous broadening of optical transitions in Yb: $CaYAlO_4$," Opt. Mater. **30**, 1093-1097 (2008).
43. P. Sévillano, P. Georges, F. Druon, D. Descamps, and E. Cormier, "32-fs Kerr-lens mode-locked Yb:$CaGdAlO_4$ oscillator optically pumped by a bright fiber laser," Opt. Lett. **39**, 6001-6004 (2014).
44. J. Ma, H. Huang, K. Ning, X. Xu, G. Xie, L. Qian, K. P. Loh, and D. Tang, "Generation of 30 fs pulses from a diode-pumped graphene mode-locked Yb:$CaYAlO_4$ laser," Opt. Lett. **41**, 890-893 (2016).
45. Q. Hu, Z. Jia, C. Tang, N. Lin, J. Zhang, N. Jia, S. Wang, X. Zhao, and X. Tao, "The origin of coloration of $CaGdAlO_4$ crystals and its effect on their physical properties," CrystEngComm. **19**, 537-545 (2017).

46. J. Di, X. Xu, C. Xia, Q. Sai, D. Zhou, Z. Lv, and J. Xu, "Growth and spectra properties of Tm, Ho doped and Tm, Ho co-doped $CaGdAlO_4$ crystals," J. Lumin. **155**, 101-107 (2014).
47. P. Loiko, X. Mateos, S. Y. Choi, F. Rotermund, C. Liebald, M. Peltz, S. Vernay, D. Rytz, Y. Wang, M. Kemnitzer, A. Agnesi, E. Vilejshikova, K. Yumashev, U. Griebner, and V. Petrov, "Tm:$CaGdAlO_4$: spectroscopy, microchip laser and passive Q-switching by carbon nanostructures," Proc. SPIE **10082**, 1008228 (2017).
48. S. Gao, Z. You, J. Xu, Y. Sun, and C. Tu, "Continuous wave laser operation of Tm and Ho co-doped $CaYAlO_4$ and $CaGdAlO_4$ crystals," Mater. Lett. **141**, 59-62 (2015).
49. V. Petrov, M. Cinta Pujol, X. Mateos, Ò. Silvestre, S. Rivier, M. Aguiló, R. M. Solé, J. Liu, U. Griebner, and F. Díaz, "Growth and properties of $KLu(WO_4)_2$, and novel ytterbium and thulium lasers based on this monoclinic crystalline host," Laser Photonics Rev. **1**, 179-212 (2007).
50. V. Kravchenko, "Crystal structure of the monoclinic form of magnesium tungstate $MgWO_4$," Journal of Structural Chemistry **10**, 139-140 (1969).
51. E. Cavalli, A. Belletti, and M. Brik, "Optical spectra and energy levels of the $Cr^{3+}$ ions in $MWO_4$ (M= Mg, Zn, Cd) and $MgMoO_4$ crystals," J. Phys. Chem. Solids **69**, 29-34 (2008).
52. L. Zhang, H. Lin, G. Zhang, X. Mateos, J. M. Serres, M. Aguiló, F. Díaz, U. Griebner, V. Petrov, Y. Wang, P. Loiko, E. Vilejshikova, K. Yumashev, Z. Lin, and W. Chen, "Crystal growth, optical spectroscopy and laser action of $Tm^{3+}$-doped monoclinic magnesium tungstate," Opt. Express **25**, 3682-3693 (2017).
53. L. Zhang, Y. Huang, S. Sun, F. Yuan, Z. Lin, and G. Wang, "Thermal and spectral characterization of $Cr^{3+}$:$MgWO_4$—a promising tunable laser material," J. Lumin. **169, Part A**, 161-164 (2016).
54. L. Zhang, W. Chen, J. Lu, H. Lin, L. Li, G. Wang, G. Zhang, and Z. Lin, "Characterization of growth, optical properties, and laser performance of monoclinic Yb:$MgWO_4$ crystal," Opt. Mater. Express **6**, 1627-1634 (2016).
55. F. A. Danevich, D. M. Chernyak, A. M. Dubovik, B. V. Grinyov, S. Henry, H. Kraus, V. M. Kudovbenko, V. B. Mikhailik, L. L. Nagornaya, R. B. Podviyanuk, O. G. Polischuk, I. A. Tupitsyna, and Y. Y. Vostretsov, "$MgWO_4$–A new crystal scintillator," Nucl. Instrum. Meth. A **608**, 107-115 (2009).
56. K. Beil, S. T. Fredrich-Thornton, F. Tellkamp, R. Peters, C. Kränkel, K. Petermann, and G. Huber, "Thermal and laser properties of Yb:LuAG for kW thin disk lasers," Opt. Express **18**, 20712-20722 (2010).
57. A. J. DeMaria, D. A. Stetser, and H. Heynau, "Self mode-locking of lasers with saturable absorbers," Appl. Phys. Lett. **8**, 174-176 (1966).
58. U. Keller, K. J. Weingarten, F. X. Kartner, D. Kopf, B. Braun, I. D. Jung, R. Fluck, C. Honninger, N. Matuschek, and J. A. d. Au, "Semiconductor saturable absorber mirrors (SESAM's) for femtosecond to nanosecond pulse generation in solid-state lasers," IEEE J. Sel. Top. Quantum Electron. **2**, 435-453 (1996).

59. U. Keller, "Recent developments in compact ultrafast lasers," Nature **424**, 831-838 (2003).
60. W. B. Cho, J. H. Yim, S. Y. Choi, S. Lee, A. Schmidt, G. Steinmeyer, U. Griebner, V. Petrov, D.-I. Yeom, K. Kim, and F. Rotermund, "Boosting the nonlinear optical response of carbon nanotube saturable absorbers for broadband mode-locking of bulk lasers," Adv. Funct. Mater. **20**, 1937-1943 (2010).
61. F. Bonaccorso, Z. Sun, T. Hasan, and A. C. Ferrari, "Graphene photonics and optoelectronics," Nat. Photon. **4**, 611-622 (2010).
62. J. Ma, G. Xie, P. Lv, W. Gao, P. Yuan, L. Qian, U. Griebner, V. Petrov, H. Yu, H. Zhang, and J. Wang, "Wavelength-versatile graphene-gold film saturable absorber mirror for ultra-broadband mode-locking of bulk lasers," Sci. Rep. **4**, 5016 (2014).
63. M. Haiml, R. Grange, and U. Keller, "Optical characterization of semiconductor saturable absorbers," Appl. Phys. B **79**, 331-339 (2004).
64. G. Xing, H. Guo, X. Zhang, T. C. Sum, and C. H. A. Huan, "The Physics of ultrafast saturable absorption in graphene," Opt. Express **18**, 4564-4573 (2010).
65. R. L. Sutherland, *Handbook of nonlinear optics,* 2nd ed. (Marcel Dekker, New York, NY, 2003).
66. E. R. Thoen, E. M. Koontz, M. Joschko, P. Langlois, T. R. Schibli, F. X. Kärtner, E. P. Ippen, and L. A. Kolodziejski, "Two-photon absorption in semiconductor saturable absorber mirrors," Appl. Phys. Lett. **74**, 3927-3929 (1999).
67. U. Keller, T. H. Chiu, and J. F. Ferguson, "Self-starting and self-Q-switching dynamics of passively mode-locked Nd:YLF and Nd:YAG lasers," Opt. Lett. **18**, 217-219 (1993).
68. M. J. Lederer, B. Luther-Davies, H. H. Tan, C. Jagadish, M. Haiml, U. Siegner, and U. Keller, "Nonlinear optical absorption and temporal response of arsenic- and oxygen-implanted GaAs," Appl. Phys. Lett. **74**, 1993-1995 (1999).
69. J. Paajaste, S. Suomalainen, R. Koskinen, A. Härkönen, G. Steinmeyer, and M. Guina, "GaSb-based semiconductor saturable absorber mirrors for mode-locking 2 μm semiconductor disk lasers," phys. stat. sol. (c) **9**, 294-297 (2012).
70. U. Keller, W. H. Knox, and H. Roskos, "Coupled-cavity resonant passive mode-locked Ti:sapphire laser," Opt. Lett. **15**, 1377-1379 (1990).
71. U. Keller, D. A. B. Miller, G. D. Boyd, T. H. Chiu, J. F. Ferguson, and M. T. Asom, "Solid-state low-loss intracavity saturable absorber for Nd:YLF lasers: an antiresonant semiconductor Fabry–Perot saturable absorber," Opt. Lett. **17**, 505-507 (1992).
72. L. R. Brovelli, I. D. Jung, D. Kopf, M. Kamp, M. Moser, F. X. Kärtner, and U. Keller, "Self-starting soliton modelocked Ti-sapphire laser using a thin semiconductor saturable absorber," Electron. Lett. **31**, 287-289 (1995).
73. J. Paajaste, S. Suomalainen, A. Härkönen, U. Griebner, G. Steinmeyer, and M. Guina, "Absorption recovery dynamics in 2 μm GaSb-based SESAMs," J. Phys. D: Appl. Phys. **47**, 065102 (2014).

74. Q. Bao, H. Zhang, Y. Wang, Z. Ni, Y. Yan, Z. X. Shen, K. P. Loh, and D. Y. Tang, "Atomic-layer graphene as a saturable absorber for ultrafast pulsed lasers," Adv. Funct. Mater. **19**, 3077-3083 (2009).
75. A. K. Geim and K. S. Novoselov, "The rise of graphene," Nat. Mater. **6**, 183-191 (2007).
76. M. J. Bronikowski, P. A. Willis, D. T. Colbert, K. A. Smith, and R. E. Smalley, "Gas-phase production of carbon single-walled nanotubes from carbon monoxide via the HiPco process: A parametric study," J. Vac. Sci. Technol. A **19**, 1800-1805 (2001).
77. J. H. Yim, W. B. Cho, S. Lee, Y. H. Ahn, K. Kim, H. Lim, G. Steinmeyer, V. Petrov, U. Griebner, and F. Rotermund, "Fabrication and characterization of ultrafast carbon nanotube saturable absorbers for solid-state laser mode locking near 1 μm," Appl. Phys. Lett. **93**, 161106 (2008).
78. S. M. Bachilo, M. S. Strano, C. Kittrell, R. H. Hauge, R. E. Smalley, and R. B. Weisman, "Structure-assigned optical spectra of single-walled carbon nanotubes," Science **298**, 2361-2366 (2002).
79. A. Schmidt, "Carbon nanostructures for femtosecond mode-locked lasers in the 1.0 to 2.1 micrometer wavelength range," Dissertation (Humboldt University, Berlin, 2016).
80. W. B. Cho, A. Schmidt, J. H. Yim, S. Y. Choi, S. Lee, F. Rotermund, U. Griebner, G. Steinmeyer, V. Petrov, X. Mateos, M. C. Pujol, J. J. Carvajal, M. Aguiló, and F. Díaz, "Passive mode-locking of a Tm-doped bulk laser near 2 μm using a carbon nanotube saturable absorber," Opt. Express **17**, 11007-11012 (2009).
81. F. Rotermund, W. B. Cho, S. Y. Choi, I. H. Baek, J. H. Yim, S. Lee, A. Schmidt, G. Steinmeyer, U. Griebner, and D.-I. Yeom, "Mode-locking of solid-state lasers by single-walled carbon-nanotube based saturable absorbers," Quantum Electron. **42**, 663-670 (2012).
82. I. H. Baek, S. Y. Choi, H. W. Lee, W. B. Cho, V. Petrov, A. Agnesi, V. Pasiskevicius, D.-I. Yeom, K. Kim, and F. Rotermund, "Single-walled carbon nanotube saturable absorber assisted high-power mode-locking of a Ti:sapphire laser," Opt. Express **19**, 7833-7838 (2011).
83. R. R. Nair, P. Blake, A. N. Grigorenko, K. S. Novoselov, T. J. Booth, T. Stauber, N. M. R. Peres, and A. K. Geim, "Fine structure constant defines visual transparency of graphene," Science **320**, 1308 (2008).
84. Q. Bao, H. Zhang, Z. Ni, Y. Wang, L. Polavarapu, Z. Shen, Q.-H. Xu, D. Tang, and K. P. Loh, "Monolayer graphene as a saturable absorber in a mode-locked laser," Nano Res. **4**, 297-307 (2011).
85. F. Zhang, S. Han, Y. Liu, Z. Wang, and X. Xu, "Dependence of the saturable absorption of graphene upon excitation photon energy," Appl. Phys. Lett. **106**, 091102 (2015).
86. W. B. Cho, J. W. Kim, H. W. Lee, S. Bae, B. H. Hong, S. Y. Choi, I. H. Baek, K. Kim, D.-I. Yeom, and F. Rotermund, "High-quality, large-area monolayer graphene for efficient bulk laser mode-locking near 1.25 μm," Opt. Lett. **36**, 4089-4091 (2011).
87. H. Yang, X. Feng, Q. Wang, H. Huang, W. Chen, A. T. S. Wee, and W. Ji, "Giant two-photon absorption in bilayer graphene," Nano Lett. **11**, 2622-2627 (2011).

88. V. Aleksandrov, A. Gluth, V. Petrov, I. Buchvarov, G. Steinmeyer, J. Paajaste, S. Suomalainen, A. Härkönen, M. Guina, X. Mateos, F. Díaz, and U. Griebner, "Mode-locked Tm,Ho:$KLu(WO_4)_2$ laser at 2060 nm using InGaSb-based SESAMs," Opt. Express **23**, 4614-4619 (2015).
89. W. Rudolph and B. Wilhelmi, *Light pulse compression,* (Harwood Academic Publishers, New York, NY, 1989).
90. R. L. Fork, O. E. Martinez, and J. P. Gordon, "Negative dispersion using pairs of prisms," Opt. Lett. **9**, 150-152 (1984).
91. M. Daimon and A. Masumura, "High-accuracy measurements of the refractive index and its temperature coefficient of calcium fluoride in a wide wavelength range from 138 to 2326 nm," Appl. Opt. **41**, 5275-5281 (2002).
92. M. J. Dodge, "Refractive properties of magnesium fluoride," Appl. Opt. **23**, 1980-1985 (1984).
93. D. E. Zelmon, D. L. Small, and R. Page, "Refractive-index measurements of undoped yttrium aluminum garnet from 0.4 to 5.0 μm," Appl. Opt. **37**, 4933-4935 (1998).
94. C. A. Klein, "Room-temperature dispersion equations for cubic zinc sulfide," Appl. Opt. **25**, 1873-1875 (1986).
95. B. Tatian, "Fitting refractive-index data with the Sellmeier dispersion formula," Appl. Opt. **23**, 4477-4485 (1984).
96. I. H. Malitson, "Interspecimen comparison of the refractive index of fused silica," J. Opt. Soc. Am. **55**, 1205-1209 (1965).
97. R. Szipöcs, K. Ferencz, C. Spielmann, and F. Krausz, "Chirped multilayer coatings for broadband dispersion control in femtosecond lasers," Opt. Lett. **19**, 201-203 (1994).
98. H. A. Haus, "Theory of mode locking with a slow saturable absorber," IEEE J. Quantum Electron. **11**, 736-746 (1975).
99. H. A. Haus, "Theory of mode locking with a fast saturable absorber," J. Appl. Phys. **46**, 3049-3058 (1975).
100. H. A. Haus, "Mode-locking of lasers," IEEE J. Sel. Top. Quantum Electron. **6**, 1173-1185 (2000).
101. O. E. Martinez, R. L. Fork, and J. P. Gordon, "Theory of passively mode-locked lasers including self-phase modulation and group-velocity dispersion," Opt. Lett. **9**, 156-158 (1984).
102. V. Petrov, D. Georgiev, J. Herrmann, and U. Stamm, "Theory of cw passive mode-locking of solid state lasers with addition of nonlinear index and group velocity dispersion," Opt. Commun. **91**, 123-130 (1992).
103. J.-C. M. Diels, J. J. Fontaine, I. C. McMichael, and F. Simoni, "Control and measurement of ultrashort pulse shapes (in amplitude and phase) with femtosecond accuracy," Appl. Opt. **24**, 1270-1282 (1985).
104. C. Hönninger, R. Paschotta, F. Morier-Genoud, M. Moser, and U. Keller, "Q-switching stability limits of continuous-wave passive mode locking," J. Opt. Soc. Am. B **16**, 46-56 (1999).

105. H. A. Haus, "Parameter ranges for CW passive mode locking," IEEE J. Quantum Electron. **12**, 169-176 (1976).
106. F. X. Kärtner, L. R. Brovelli, D. Kopf, M. Kamp, I. Calasso, and U. Keller, "Control of solid state laser dynamics by semiconductor devices," Opt. Eng. **34**, 2024-2036 (1995).
107. D. Von der Linde, "Characterization of the noise in continuously operating mode-locked lasers," Appl. Phys. B **39**, 201-217 (1986).
108. F. Salin, P. Grangier, G. Roger, and A. Brun, "Observation of high-order solitons directly produced by a femtosecond ring laser," Phys. Rev. Lett. **56**, 1132-1135 (1986).
109. U. Keller, J. A. Valdmanis, M. C. Nuss, and A. M. Johnson, "53 ps pulses at 1.32 μm from a harmonic mode-locked Nd: YAG laser," IEEE J. Quantum Electron. **24**, 427-430 (1988).
110. J. Aus der Au, D. Kopf, F. Morier-Genoud, M. Moser, and U. Keller, "60-fs pulses from a diode-pumped Nd: glass laser," Opt. Lett. **22**, 307-309 (1997).
111. M. J. Lederer, B. Luther-Davies, H. H. Tan, C. Jagadish, N. N. Akhmediev, and J. M. Soto-Crespo, "Multipulse operation of a Ti:sapphire laser mode locked by an ion-implanted semiconductor saturable-absorber mirror," J. Opt. Soc. Am. B **16**, 895-904 (1999).
112. N. P. Barnes and D. J. Gettemy, "Pulsed Ho:YAG oscillator and amplifier," IEEE J. Quantum Electron. **17**, 1303-1308 (1981).
113. F. Heine, E. Heumann, G. Huber, and K. L. Schepler, "Mode locking of room-temperature cw thulium and holmium lasers," Appl. Phys. Lett. **60**, 1161-1162 (1992).
114. J. F. Pinto, G. H. Rosenblatt, and L. Esterowitz, "Continuous-wave mode-locked 2-μm Tm:YAG laser," Opt. Lett. **17**, 731-732 (1992).
115. L. E. Nelson, E. P. Ippen, and H. A. Haus, "Broadly tunable sub-500 fs pulses from an additive-pulse mode-locked thulium-doped fiber ring laser," Appl. Phys. Lett. **67**, 19-21 (1995).
116. Y. Nomura and T. Fuji, "Sub-50-fs pulse generation from thulium-doped ZBLAN fiber laser oscillator," Opt. Express **22**, 12461-12466 (2014).
117. Y. Nomura and T. Fuji, "Generation of watt-class, sub-50 fs pulses through nonlinear spectral broadening within a thulium-doped fiber amplifier," Opt. Express **25**, 13691-13696 (2017).
118. M. C. Stumpf, S. Pekarek, A. E. H. Oehler, T. Südmeyer, J. M. Dudley, and U. Keller, "Self-referencable frequency comb from a 170-fs, 1.5-μm solid-state laser oscillator," Appl. Phys. B **99**, 401-408 (2010).
119. A. A. Lagatsky, F. Fusari, S. Calvez, S. V. Kurilchik, V. E. Kisel, N. V. Kuleshov, M. D. Dawson, C. T. A. Brown, and W. Sibbett, "Femtosecond pulse operation of a Tm,Ho-codoped crystalline laser near 2 μm," Opt. Lett. **35**, 172-174 (2010).
120. A. A. Lagatsky, X. Han, M. D. Serrano, C. Cascales, C. Zaldo, S. Calvez, M. D. Dawson, J. A. Gupta, C. T. A. Brown, and W. Sibbett, "Femtosecond (191 fs) $NaY(WO_4)_2$ Tm,Ho-codoped laser at 2060 nm," Opt. Lett. **35**, 3027-3029 (2010).

121. A. A. Lagatsky, P. Koopmann, P. Fuhrberg, G. Huber, C. T. A. Brown, and W. Sibbett, "Passively mode locked femtosecond Tm:$Sc_2O_3$ laser at 2.1 μm," Opt. Lett. **37**, 437-439 (2012).
122. A. A. Lagatsky, O. L. Antipov, and W. Sibbett, "Broadly tunable femtosecond Tm:$Lu_2O_3$ ceramic laser operating around 2070 nm," Opt. Express **20**, 19349-19354 (2012).
123. A. Schmidt, P. Koopmann, G. Huber, P. Fuhrberg, S. Y. Choi, D.-I. Yeom, F. Rotermund, V. Petrov, and U. Griebner, "175 fs Tm:$Lu_2O_3$ laser at 2.07 μm mode-locked using single-walled carbon nanotubes," Opt. Express **20**, 5313-5318 (2012).
124. A. Schmidt, S. Y. Choi, D.-I. Yeom, F. Rotermund, X. Mateos, M. Segura, F. Diaz, V. Petrov, and U. Griebner, "Femtosecond pulses near 2 μm from a Tm:KLuW laser mode-locked by a single-walled carbon nanotube saturable absorber," Appl. Phys. Express **5**, 092704 (2012).
125. D. M. Kane, "Astigmatism compensation in off-axis laser resonators with two or more coupled foci," Opt. Commun. **71**, 113-118 (1989).
126. M. Wittmann, A. Penzkofer, and W. Bäumler, "Generation of frequency tunable femtosecond pulses in a cw pumped linear dispersion-balanced passive mode-locked Rhodamine 6G dye laser," Opt. Commun. **90**, 182-192 (1992).
127. W.-X. Zhang, Y.-B. Pan, J. Zhou, W.-B. Liu, J. Li, Y.-W. Zou, and Z.-Y. Wei, "Preparation and characterization of transparent Tm:YAG ceramics," Ceram. Int. **37**, 1133-1137 (2011).
128. A. Gluth, Y. Wang, V. Petrov, J. Paajaste, S. Suomalainen, A. Härkönen, M. Guina, G. Steinmeyer, X. Mateos, S. Veronesi, M. Tonelli, J. Li, Y. Pan, J. Guo, and U. Griebner, "GaSb-based SESAM mode-locked Tm:YAG ceramic laser at 2 μm," Opt. Express **23**, 1361-1369 (2015).
129. J. Ma, G. Xie, J. Zhang, P. Yuan, D. Tang, and L. Qian, "Passively mode-locked Tm:YAG ceramic laser based on graphene," IEEE J. Sel. Top. Quantum Electron. **21**, 1100806 (2015).
130. T. Feng, K. Yang, J. Zhao, S. Zhao, W. Qiao, T. Li, T. Dekorsy, J. He, L. Zheng, Q. Wang, X. Xu, L. Su, and J. Xu, "1.21 W passively mode-locked Tm:LuAG laser," Opt. Express **23**, 11819-11825 (2015).
131. K. Yang, H. Bromberger, H. Ruf, H. Schäfer, J. Neuhaus, T. Dekorsy, C. V.-B. Grimm, M. Helm, K. Biermann, and H. Künzel, "Passively mode-locked Tm,Ho:YAG laser at 2 μm based on saturable absorption of intersubband transitions in quantum wells," Opt. Express **18**, 6537-6544 (2010).
132. K. Yang, D. Heinecke, J. Paajaste, C. Kölbl, T. Dekorsy, S. Suomalainen, and M. Guina, "Mode-locking of 2 μm Tm,Ho:YAG laser with GaInAs and GaSb-based SESAMs," Opt. Express **21**, 4311-4318 (2013).
133. B. Q. Yao, Z. Cui, J. Wang, X. M. Duan, T. Y. Dai, Y. Q. Du, J. H. Yuan, and W. Liu, "An actively mode-locked Ho:YAG solid laser pumped by a Tm:YLF laser," Laser Phys. Lett. **12**, 025002 (2015).

134. X. Duan, J. Yuan, Z. Cui, B. Yao, T. Dai, J. Li, and Y. Pan, "Resonantly pumped actively mode-locked Ho:YAG ceramic laser at 2122.1 nm," Appl. Opt. **55**, 1953-1956 (2016).
135. W. X. Zhang, J. Zhou, W. B. Liu, J. Li, L. Wang, B. X. Jiang, Y. B. Pan, X. J. Cheng, and J. Q. Xu, "Fabrication, properties and laser performance of Ho:YAG transparent ceramic," J. Alloys Compd. **506**, 745-748 (2010).
136. G. Q. Xie, D. Y. Tang, H. Luo, H. J. Zhang, H. H. Yu, J. Y. Wang, X. T. Tao, M. H. Jiang, and L. J. Qian, "Dual-wavelength synchronously mode-locked Nd:CNGG laser," Opt. Lett. **33**, 1872-1874 (2008).
137. H. Yoshioka, S. Nakamura, T. Ogawa, and S. Wada, "Dual-wavelength mode-locked Yb:YAG ceramic laser in single cavity," Opt. Express **18**, 1479-1486 (2010).
138. L. C. Kong, Z. P. Qin, G. Q. Xie, X. D. Xu, J. Xu, P. Yuan, and L. J. Qian, "Dual-wavelength synchronous operation of a mode-locked 2-μm Tm:$CaYAlO_4$ laser," Opt. Lett. **40**, 356-358 (2015).
139. Z. Qin, G. Xie, L. Kong, P. Yuan, L. Qian, X. Xu, and J. Xu, "Diode-pumped passively mode-locked Tm:$CaGdAlO_4$ laser at 2 μm wavelength," IEEE Photon. J. **7**, 1500205 (2015).
140. P. Loiko, P. Becker, L. Bohatý, C. Liebald, M. Peltz, S. Vernay, D. Rytz, J. M. Serres, X. Mateos, Y. Wang, X. Xu, J. Xu, A. Major, A. Baranov, U. Griebner, and V. Petrov, "Sellmeier equations, group velocity dispersion, and thermo-optic dispersion formulas for $CaLnAlO_4$ (Ln = Y, Gd) laser host crystals," Opt. Lett. **42**, 2275-2278 (2017).
141. P. Loiko, J. M. Serres, X. Mateos, M. Aguiló, F. Díaz, L. Zhang, Z. Lin, H. Lin, G. Zhang, K. Yumashev, V. Petrov, U. Griebner, Y. Wang, S. Y. Choi, F. Rotermund, and W. Chen, "Monoclinic $Tm^{3+}$:$MgWO_4$: a promising crystal for continuous-wave and passively Q-switched lasers at ~2 μm," Opt. Lett. **42**, 1177-1180 (2017).
142. F. Fusari, A. A. Lagatsky, G. Jose, S. Calvez, A. Jha, M. D. Dawson, J. A. Gupta, W. Sibbett, and C. T. A. Brown, "Femtosecond mode-locked $Tm^{3+}$ and $Tm^{3+}$-$Ho^{3+}$ doped 2 μm glass lasers," Opt. Express **18**, 22090-22098 (2010).
143. A. A. Lagatsky, S. Calvez, J. A. Gupta, V. E. Kisel, N. V. Kuleshov, C. T. A. Brown, M. D. Dawson, and W. Sibbett, "Broadly tunable femtosecond mode-locking in a Tm:KYW laser near 2 μm," Opt. Express **19**, 9995-10000 (2011).
144. J. Brons, V. Pervak, D. Bauer, D. Sutter, O. Pronin, and F. Krausz, "Powerful 100-fs-scale Kerr-lens mode-locked thin-disk oscillator," Opt. Lett. **41**, 3567-3570 (2016).
145. F. Lesparre, J. T. Gomes, X. Délen, I. Martial, J. Didierjean, W. Pallmann, B. Resan, M. Eckerle, T. Graf, M. A. Ahmed, F. Druon, F. Balembois, and P. Georges, "High-power Yb:YAG single-crystal fiber amplifiers for femtosecond lasers in cylindrical polarization," Opt. Lett. **40**, 2517-2520 (2015).
146. M. Hemmer, M. Baudisch, A. Thai, A. Couairon, and J. Biegert, "Self-compression to sub-3-cycle duration of mid-infrared optical pulses in dielectrics," Opt. Express **21**, 28095-28102 (2013).

# List of publications

## *A. Parts of this thesis are based on the following published or submitted journal articles and conference proceedings:*

### I. Articles in Peer-Reviewed Journals

1. Y. Wang, W. Chen, M. Mero, L. Zhang, H. Lin, Z. Lin, G. Zhang, F. Rotermund, P. Loiko, X. Mateos, U. Griebner, and V. Petrov, "Sub-100 fs Tm:$MgWO_4$ laser at 2017 nm mode-locked by a graphene-based saturable absorber," Opt. Lett. **42** (2017), in press.
2. Y. Wang, W. Chen, L. Zhang, H. Lin, Z. Lin, G. Zhang, F. Rotermund, P. Loiko, X. Mateos, U. Griebner, and V. Petrov, "Passively mode-locked femtosecond Tm:$MgWO_4$ laser with SWCNTs as a saturable absorber," Opt. Express (2017), submitted.
3. P. Loiko, J. M. Serres, X. Mateos, M. Aguiló, F. Díaz, L. Zhang, Z. Lin, H. Lin, G. Zhang, K. Yumashev, V. Petrov, U. Griebner, Y. Wang, S. Y. Choi, F. Rotermund, and W. Chen, "Monoclinic $Tm^{3+}$:$MgWO_4$: a promising crystal for continuous-wave and passively Q-switched lasers at ~2 μm," Opt. Lett. **42**, 1177-1180 (2017).
4. L. Zhang, H. Lin, G. Zhang, X. Mateos, J. M. Serres, M. Aguiló, F. Díaz, U. Griebner, V. Petrov, Y. Wang, P. Loiko, E. Vilejshikova, K. Yumashev, Z. Lin, and W. Chen, "Crystal growth, optical spectroscopy and laser action of $Tm^{3+}$-doped monoclinic magnesium tungstate," Opt. Express **25**, 3682-3693 (2017).
5. Y. Wang, R. Lan, X. Mateos, J. Li, C. Li, S. Suomalainen, A. Härkönen, M. Guina, V. Petrov, and U. Griebner, "Thulium doped LuAG ceramics for passively mode locked lasers," Opt. Express **25**, 7084-7091 (2017).
6. P. Loiko, P. Becker, L. Bohaty, C. Liebald, M. Peltz, S. Vernay, D. Rytz, J. M. Serres, X. Mateos, Y. Wang, X. Xu, J. Xu, A. Major, A. Baranov, U. Griebner, and V. Petrov, "Sellmeier equations, group velocity dispersion, and thermo-optic dispersion formulas for $CaLnAlO_4$ (Ln=Y, Gd) laser host crystals," Opt. Lett. **42**, 2275-2278 (2017).
7. Y. Wang, R. Lan, X. Mateos, J. Li, C. Hu. C. Li, Y. Pan, S. Suomalainen, A. Härkönen, M. Guina, V. Petrov, and U. Griebner, "Broadly tunable mode-locked Ho:YAG ceramic laser around 2.1 μm," Opt. Express **24**, 18003-18012 (2016).
8. Y. Wang, G. Xie. X. Xu, J. Di, Z. Qin, S. Suomalainen, M. Guina, A. Härkönen, A. Agnesi, U. Griebner, X. Mateos, P. Loiko, and V. Petrov, "SESAM mode-locked Tm:CALGO laser at 2 μm," Opt. Mater. Express **6**, 131-136 (2016).
9. A. Gluth, Y. Wang, V. Petrov, J. Paajaste, S. Suomalainen, A. Härkönen, M. Guina, G. Steinmeyer, X. Mateos, S. Veronesi, M. Tonelli, J. Li, Y. Pan, J. Guo, and U. Griebner, "GaSb-based SESAM mode-locked Tm:YAG ceramic laser at 2 μm," Opt. Express **23**, 1361-1369 (2015).

## II. Articles in SPIE Proceedings

10. P. Loiko, X. Mateos, S. Y. Choi, F. Rotermund, C. Liebald, M. Peltz, S. Vernay, D. Rytz, Y. Wang, M. Kemnitzer, A. Agnesi, E. Vilejshikova, K. Yumashev, U. Griebner, and V. Petrov, "Tm:$CaGdAlO_4$: Spectroscopy, microchip laser and passive Q-switching by carbon nanostructures," Proc. SPIE **10082**, 1008228/1-6 (2017).

## III. Conference Papers

1. Y. Wang, W. Chen, M. Mero, L. Zhang, H. Lin, Z. Lin, G. Zhang, F. Rotermund, Y. J. Cho, P. Loiko, X. Mateos, U. Griebner, and V. Petrov, "Sub-100 fs Tm:$MgWO_4$ laser at 2017 nm," Advanced Solid State Lasers Conference, Nagoya, Japan, Oct. 1-5, 2017, accepted.
2. Y. Wang, W. Chen, L. Zhang, H. Lin, Z. Lin, G. Zhang, F. Rotermund, P. Loiko, J. M. Serres, X. Mateos, U. Griebner, and V. Petrov, "Passively mode-locked femtosecond Tm:$MgWO_4$ laser," Conference on Lasers and Electro-Optics CLEO/Europe, Munich, Germany, June 25-29, 2017, paper CF-P.28, Online Conference Digest.
3. P. Loiko, J. M. Serres, L. Zhang, X. Mateos, M. Aguiló, F. Díaz, Z. Lin, H. Lin, G. Zhang, K. Yumashev, V. Petrov, U. Griebner, Y. Wang, S. Y. Choi, F. Rotermund, and W. Chen, "Monoclinic $Tm^{3+}$:$MgWO_4$ – A novel efficient laser emitting above 2 μm," Conference on Lasers and Electro-Optics CLEO/Europe, Munich, Germany, June 25-29, 2017, paper CE-1.5, Online Conference Digest.
4. L. Z. Zhang, Z. B. Lin, H. F. Lin, G. Zhang, X. Mateos, P. Loiko, J. M. Serres, M. Aguiló, F. Díaz, Y. C. Wang, U. Griebner, V. Petrov, E. Vilejshikova, K. Yumashev, and W. D. Chen, "Growth, spectroscopy and laser operation of Tm-doped monoclinic magnesium tungstate (Tm:$MgWO_4$)," Conference on Lasers and Electro-Optics CLEO'17, San Jose (CA), USA, May 14-19, 2017, paper STh4I.6, CLEO Online Technical Digest.
5. Y. Wang, R. Lan, X. Mateos, J. Li, S. Suomalainen, A. Härkönen, M. Guina, U. Griebner, and V. Petrov, "Passively mode-locked Tm:LuAG ceramic laser," Conference on Lasers and Electro-Optics CLEO'17, San Jose (CA), USA, May 14-19, 2017, paper SF2K.3, CLEO Online Technical Digest.
6. X. Mateos, L. Zhang, Z. Lin, H. Lin, G. Zhang, P. Loiko, J. M. Serres, M. Aguiló, F. Díaz, Y. Wang, U. Griebner, V. Petrov, E. Vilejshikova, K. Yumashev, and W. Chen, "Growth, Spectroscopy and Laser Operation of Tm-doped Monoclinic Magnesium Tungstate (Tm:MgWO4)," in Conference on Lasers and Electro-Optics, STh4I.6 (2017).
7. P. Becker, L. Bohaty, C. Liebald, M. Peltz, S. Vernay, D. Rytz, P. Loiko, J. M. Serres, X. Mateos, K. Yumashev, Y. Wang, V. Petrov, and U. Griebner, "Sellmeier equations for $CaGdAlO_4$ and $CaYAlO_4$," Europhoton 2016, 7th EPS-QEOD Europhoton Conference on Solid-State, Fibre and Waveguide Coherent Light Sources, Vienna, Austria, Aug. 21-26, 2016, paper PO-3.13, Conference Digest, p. 48.
8. Y. Wang, R. Lan, X. Mateos, J. Li, Y. Pan, S. Suomalainen, A. Härkönen, M. Guina, U. Griebner, and V. Petrov, "In-band-pumped mode-locked Ho:YAG ceramic laser at 2.1 μm"

Conference on Lasers and Electro-Optics CLEO'16, San Jose (CA), USA, June 5-10, 2016, paper STu4M.1, CLEO Online Technical Digest.

9. Y. Wang, G. Xie. X. Xu, J. Di, Z. Qin, S. Suomalainen, M. Guina, A. Härkönen, A. Agnesi, U. Griebner, X. Mateos, P. Loiko, and V. Petrov, "SESAM mode-locked Tm:CALGO laser at 2 μm," Advanced Solid State Lasers Conference, Berlin, Germany, Oct. 4-9, 2015, paper AW1A.2.

## *B. The following papers appeared during the PhD work of the candidate but remained outside the scope of the thesis.*

### I. Articles in Peer-Reviewed Journals

1. T. Xu, Y. Wang, D. Lu, Z. Pan, H. Yu, H. Zhang, and J. Wang, "The modulation mechanism of growth atmosphere on composition and phase transition behavior in barium calcium titanate crystal," Cryst. Res. Technol. **52,** 1700009/1-7 (2017).

2. Z. Zhang, P. Loiko, H. Wu, X. Mateos, J. M. Serres, H. F. Lin, W. D. Chen, G. Zhang, L. Z. Zhang, F. Díaz, M. Aguiló, V. Petrov, U. Griebner, Y. C. Wang, E. Vilejshikova, K. Yumashev, and Z. B. Lin, "Disordered Tm:$Ca_9La(VO_4)_7$: a novel crystal with potential for broadband tunable lasing," Opt. Mater. Express **7**, 484-493 (2017).

3. R. Lan, X. Mateos, Y. Wang, J. M. Serres, P. Loiko, J. Li, Y. Pan, U. Griebner, and V. Petrov, "Semiconductor saturable absorber Q-switching of a holmium microchip laser," Opt. Express **25**, 4579-4584 (2017).

4. R. Lan, P. Loiko, X. Mateos, Y. Wang, J. Li, Y. Pan, S. Y. Choi, M. H. Kim, F. Rotermund, A. Yasukevich, K. Yumashev, U. Griebner, and V. Petrov, "Passive Q-switching of microchip lasers based on Ho:YAG ceramics," Appl. Opt. **55**, 4877-4887 (2016).

5. J. Di, X. Sun, X. Xu, C. Xia, Q. Sai, H. Yu, Y. Wang, L. Zhu, Y. Gao and X. Guo, "Growth and spectral characters of Nd:$CaGdAlO_4$ crystal," Eur. Phys. J. Appl. Phys. **74**, 10501/1-6 (2016).

6. M. Rüsing, S. Sanna, S. Neufeld, G. Berth, W. G. Schmidt, A. Zrenner, H. Yu, Y. Wang, and H. Zhang, "Vibrational properties of $LiNb_{1-x}Ta_xO_3$ mixed crystals," Phys. Rev. B **93**, 184305/1-11 (2016).

7. F. J. Furch, A. Giree, F. Morales, A. Anderson, Y. Wang, C. P. Schulz, and M. J. J. Vrakking, "Close to transform-limited, few-cycle 12 μJ pulses at 400 kHz for applications in ultrafast spectroscopy," Opt. Express **24**, 19293-19310 (2016).

8. P. Loiko, X. Mateos, Y. Wang, Z. Pan, K. Yumashev, H. Zhang, U. Griebner, and V. Petrov, "Thermo-optic dispersion formulas for YCOB and GdCOB laser host crystals," Opt. Mater. Express **5** 1089-1097 (2015).

## II. Conference Papers

1. P. Loiko, X. Mateos, J. M. Serres, R. Lan, S. Y. Choi, F. Rotermund, Y. Wang, J. Li, Y. Pan, M. Aguiló, F. Díaz, U. Griebner, and V. Petrov, "Single-walled carbon nanotubes oust graphene and semiconductor saturable absorbers in Q-switched solid-state lasers at 2 μm," Conference on Lasers and Electro-Optics CLEO/Europe, Munich, Germany, June 25-29, 2017, paper CA-5.2, Online Conference Digest.

2. L. Z. Zhang, Z. B. Lin, X. Mateos, P. Loiko, J. M. Serres, Y. C. Wang, U. Griebner, V. Petrov, M. Aguiló, F. Díaz, E. Vilejshikova, K. Yumashev, H. F. Lin, G. Zhang, and W. D. Chen, "Growth, spectroscopy and laser operation of a novel disordered tetragonal tungstate crystal – Tm:$Na_2La_4(WO_4)_7$," The 6th Advanced Lasers and Photon Sources (ALPS'17), Yokohama, Japan, Apr. 18 - Apr. 21, 2017, paper ALPS11-4. Proceedings (USB stick), 2 pages.

3. P. Loiko, X. Mateos, S. Y. Choi, F. Rotermund, C. Liebald, M. Peltz, S. Vernay, D. Rytz, Y. Wang, M. Kemnitzer, A. Agnesi, K. Yumashev, U. Griebner, and V. Petrov, "Tm:CALGO laser passively Q-switched by graphene and single-walled carbon nanotubes," Photonics West 17: Lasers and applications in science and engineering, SPIE Conference 10082: "Solid State Lasers XXVI: Technology and Devices", San Francisco (CA), USA, Jan. 28 - Feb. 2, 2017, paper [10082-79], Technical Summaries.

4. R. Lan, P. Loiko, X. Mateos, Y. Wang, J. Li, Y. Pan, S. Y. Choi, M. H. Kim, F. Rotermund, K. Yumashev, U. Griebner, and V. Petrov, "Passively Q-switched Ho:YAG ceramic lasers," 12th Laser Ceramics Symposium, International Symposium on Transparent Ceramics for Photonic Applications, Saint-Louis, France, Nov. 28 - Dec. 2, 2016, paper. We-5-O-03.

5. R. Lan, X. Mateos, P. Loiko, Y. Wang, S. Y. Choi, F. Rotermund, M. Aguiló, F. Díaz, K. Yumashev, U. Griebner, and V. Petrov, "Sub-100 ns Tm:KLuW and Ho:KLuW lasers passively Q-switched with SWCNTs," Conference on Lasers and Electro-Optics CLEO'16, San Jose (CA), USA, June 5-10, 2016, paper JTu5A.36, CLEO Online Technical Digest.

6. R. Lan, P. Loiko, X. Mateos, Y. Wang, J. Li, Y. Pan, S. Y. Choi, M. H. Kim, F. Rotermund, A. Yasukevich, K. Yumashev, U. Griebner, and V. Petrov, "Passive Q-switching of Ho:YAG ceramic lasers at 2.1 μm," Conference on Lasers and Electro-Optics CLEO'16, San Jose (CA), USA, June 5-10, 2016, paper STu4M.6, CLEO Online Technical Digest.

7. R. Lan, X. Mateos, Y. Wang, P. Loiko, J. M. Serres, J. Li, Y. Pan, K. Yumashev, V. Petrov, and U. Griebner, "Semiconductor saturable absorber Q-switching of a holmium microchip laser," Advanced Solid State Lasers Conference, Boston (MA), USA, Oct. 30 - Nov. 03, 2016, paper JTu2A.22.

8. P. Loiko, X. Mateos, Y. Wang, Z. Pan, K. Yumashev, H. Zhang, H. Yu, U. Griebner, and V. Petrov, "Thermo-optic dispersion formulas for YCOB and GdCOB laser host crystals," Advanced Solid State Lasers Conference, Berlin, Germany, Oct. 4-9, 2015, paper AM2A.7.

9. F. J. Furch, A. Anderson, S. Birkner, Y. Wang, A. Giree, C. P. Schulz, and M. J. J. Vrakking, "Improved characteristics of high repetition rate non-collinear optical parametric amplifiers for electron-ion coincidence spectroscopy," Conference on Lasers and Electro-Optics CLEO'15, San Jose (CA), USA, May 10 - May 15, 2015, paper SF1M.5, CLEO Online Technical Digest

# Acknowledgements

During the last 4 years, I have received a lot of help and support from my advisor, colleagues and friends. Without your help, I would have been unable to finish my thesis. Here I would like to express my gratitude to all of you.

First, I would like to express my sincere gratitude to my advisor Prof. Marc Vrakking for giving me the opportunity to conduct my research here at MBI. Thank you for your patience, motivation and insightful comments. You always provide me with valuable ideas and good connections, encouraging me to be a better scholar in the future.

Second, I am truly grateful to my mentor at MBI, Dr. Valentin Petrov. Your advices on my research and strict academic training have been, and will continue to be priceless for me. Many thanks to Dr. Uwe Griebner in division C of MBI, who has helped me and contributed to my research by providing samples and guidance on experimental setups, as well as providing a lot of useful advice and discussions.

My work is also greatly supported by Dr. Xavier Mateos and Dr. Pavel Loiko. Thank you not only for the inspiration and guidance but also for the great working environment you create. Your optimism and enthusiasm in research cheer me along the way. Many thanks to Dr. Weidong Chen as well for providing me with your crystals. I learn a lot from your suggestions both on research and for my career.

I would also like to express my gratitude to Dr. Mark Merö who has given great guidance and advice on the FROG measurements as well as help with the ongoing Cr:YAG project. Thanks also to Dr. Federico Furch and Dr. Alexandria Anderson who helped me with the building of f-2f interferometer during the initiate period of my research here. Thanks to Dr. Gabrielle Thomas for proofreading my drafts and helping me with ongoing experiments.

I would like to give special thanks to Chinese Scholarship Council, for their support of my Ph.D. work and study in Germany. I hope to thank my Masters advisor Prof. Huaijin Zhang and Prof. Haohai Yu for encouraging me to apply for the scholarship. Their academic suggestions help me to achieve my goals.

My time at Berlin was full of joy thanks to all my colleagues and friends: Jingming, Yingliang, Nikita, Andrey, Florian, Achut, Ruijun and Tianli. Especially for the help I received during the small bicycle accident here. Doped with titanium nails in my arm, I would say I am the most suitable guy for ultrashort pulse generation.

Finally, I would like to thank my parents who are always supporting me, sorry for my absence in family life during the last few years. Special thanks to Qiuzi for your support, company and understanding. Meeting you is the most lovely accident in the long journey from China to Berlin.

As the Chinese saying goes: There is an end to the words, but not to their message

# Selbstständigkeitserklärung

Hiermit versichere ich, dass ich die vorliegende Dissertation selbstständig und nur unter Verwendung der angegebenen Literatur und Hilfsmittel verfasst habe.
Die Arbeit ist weder in einem früheren Promotionsverfahren angenommen noch als ungenügend beurteilt worden.

_____

Berlin, den 13. Juli 2017